

ARTICLE TYPE

Efficient formulation of a two-noded geometrically exact curved beam element

Martin Horák¹ | Emma La Malfa Ribolla^{*2} | Milan Jirásek¹

¹Faculty of Civil Engineering, Czech Technical University in Prague, Prague, Czech Republic

²Department of Engineering, University of Palermo, Palermo, Italy

Correspondence

*Emma La Malfa Ribolla, Viale delle Scienze, Ed. 8. 90128 Palermo (PA). Email: emma.lamalfaribolla@unipa.it

Abstract

The paper extends the formulation of a 2D geometrically exact beam element proposed in our previous paper¹ to curved elastic beams. This formulation is based on equilibrium equations in their integrated form, combined with the kinematic relations and sectional equations that link the internal forces to sectional deformation variables. The resulting first-order differential equations are approximated by the finite difference scheme and the boundary value problem is converted to an initial value problem using the shooting method. The paper develops the theoretical framework based on the Navier-Bernoulli hypothesis, with a possible extension to shear-flexible beams. Numerical procedures for the evaluation of equivalent nodal forces and of the element tangent stiffness are presented in detail. Unlike standard finite element formulations, the present approach can increase accuracy by refining the integration scheme on the element level while the number of global degrees of freedom is kept constant. The efficiency and accuracy of the developed scheme are documented by seven examples that cover circular and parabolic arches, a spiral-shaped beam, and a spring-like beam with a zig-zag centerline. The proposed formulation does not exhibit any locking. No excessive stiffness is observed for coarse computational grids and the distribution of internal forces is not polluted by any oscillations. It is also shown that a cross effect in the relations between internal forces and deformation variables arises, i.e., the bending moment affects axial stretching and the normal force affects the curvature. This coupling is theoretically explained in the appendix.

KEYWORDS:

geometrically exact nonlinear beam, curved beam, Kirchhoff beam, large rotations, planar frame, shooting method

1 | INTRODUCTION

Curved beam models are widely used in various engineering applications involving for example arches, pipes and bridge slab structures in civil engineering or lattice metamaterials, tires, and rings in mechanical engineering. Often, these structures are discretized into multiple straight elements that represent the curved geometry only approximately. The majority of contributions to the development of curved beam elements are based on the finite element (FE) method within the small-displacement theory and address shear and membrane locking caused by the coupling between bending and stretching^{2,3,4,5,6,7}. On the other hand,

design and manufacturing of flexible as well as soft metamaterials have opened an area for the application of beams made of polymers or soft materials, for which large displacements and rotation may arise.

The key contributions to large-deformation analysis of thin beams are the theory of Reissner^{8,9}, based on the extension of Timoshenko's assumption to finite deformations, and the FE formulation developed by Simo and his coworkers^{10,11,12,13}. The geometrically exact beam theory is still attracting researchers, with recent developments in the isogeometric approach (e.g.,^{14,15}) or in computational procedures related to the parameterisation of rotations using the rotation vector (^{16,17}). In a recent work¹ we have presented a numerical formulation for two-dimensional straight beams under large sectional rotations based on the shooting method: The boundary value problem is converted into an initial value problem handled by a finite difference scheme, and the estimated values used in artificially added initial conditions are iteratively adjusted until the boundary conditions on the opposite beam end are satisfied. On the global (structural) level, the governing equations are assembled in the same way as for a standard FE beam element with six degrees of freedom. It has been demonstrated that the advantage of this approach is a dramatic reduction of the number of global degrees of freedom, since the accuracy of the numerical approximation can be conveniently increased by refining the integration scheme on the element level instead of introducing additional global unknowns.

The present paper extends the geometrically exact formulation presented by Jirásek et al.¹ to curved beams undergoing large displacements and rotations. The theoretical framework is developed in Section 2 and the corresponding numerical procedures are described in Section 3. The efficiency and accuracy of the proposed method is illustrated in Section 4 by five examples, which treat circular and parabolic arches and a logarithmic spiral.

2 | BEAM WITH INITIAL CURVATURE

2.1 | Kinematic description

The approach developed by Jirásek et al.¹ will now be extended to initially curved beams. Consider that the centerline of the undeformed beam is a planar curve of length L . An auxiliary curvilinear coordinate s is defined as the arc length measured along the undeformed centerline, with $s \in [0, L]$. For a given shape of the centerline, it is possible to specify function $\varphi_0(s)$ which describes the initial rotation of section s with respect to the left end section (this means that $\varphi_0(0) = 0$). Counterclockwise rotations are considered as positive. Displacement components u and w will be expressed with respect to a local Cartesian coordinate system xz that is attached to the left end section and follows its motion; see Fig. 1a.

The transformation of the beam from the undeformed state to the current one is decomposed into

- (A) a rigid-body translation and rotation that follows the motion of the left end section, and
- (B) a true deformation during which the left end section remains fixed.

Phase A can be handled by simple geometrical transformations and does not affect the end forces expressed with respect to the moving local coordinate system. It is therefore sufficient to focus on phase B and consider the left end of the beam as fixed. The black straight beam in Fig. 1a corresponds to a fictitious state used as a reference, while the initial stress-free configuration of the beam is plotted in red and the current deformed configuration in blue.

Fictitious displacements that describe the mapping of an arbitrary point (x, z) from its reference position in the fictitious straight state to its actual position in the initial stress-free configuration are denoted as u_0 and w_0 and considered as functions of x and z . Based on the standard assumption that all cross sections remain planar, these functions can be expressed as

$$u_0(x, z) = u_{s0}(x) + z \sin \varphi_0(x) \quad (1)$$

$$w_0(x, z) = w_{s0}(x) - z(1 - \cos \varphi_0(x)) \quad (2)$$

where u_{s0} and w_{s0} are functions of x that correspond to displacements of points on the centerline. Let us recall that φ_0 is the already introduced function defining the angle between a generic section and the left end section in the stress-free state. This angle at the same time corresponds to the rotation from the fictitious straight state to the initial stress-free state. It is also worth noting that the coordinate s measured along the arc of the curved centerline in the stress-free state has the same value as the coordinate x measured along the Cartesian axis in the fictitious straight state, and in the subsequent derivations we will write all functions as dependent on x instead of s . In the same spirit, Cartesian coordinate z in the fictitious straight state corresponds to the coordinate that would be measured in the initial stress-free state in the direction normal to the curved centerline.

Functions u_{s0} , w_{s0} and φ_0 are supposed to be specified in advance but they are not independent. The length of the centerline must remain unaffected by the transformation from the fictitious straight reference configuration to the initial stress-free

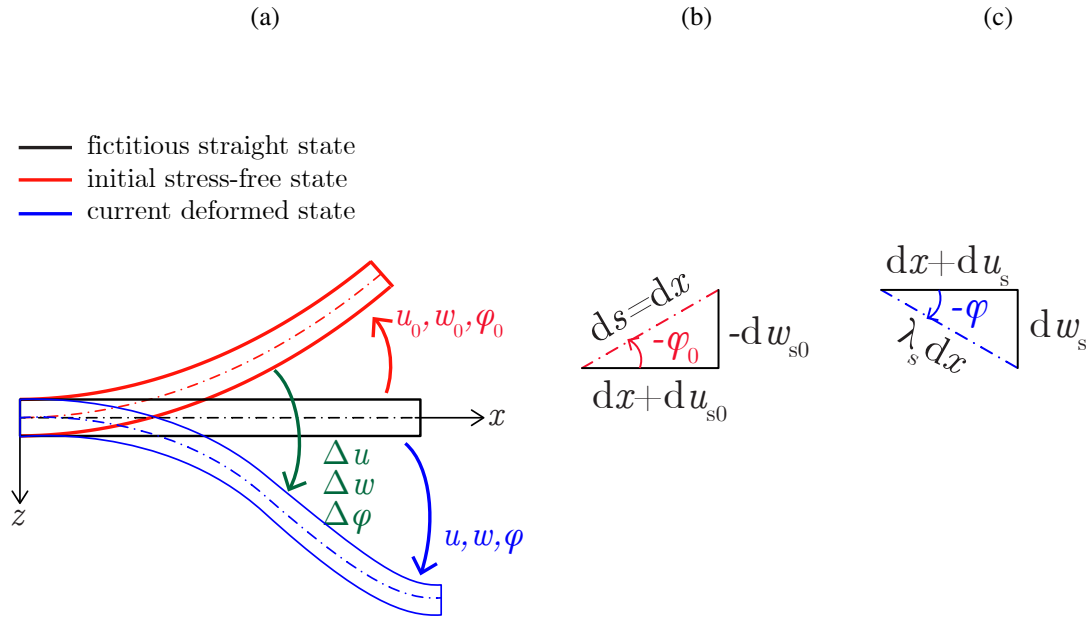


FIGURE 1 (a) Coordinate system xz aligned with the left beam end, fictitious straight configuration (black), initial stress-free configuration (red), and current deformed configuration (blue); (b) infinitesimal triangle with hypotenuse on the centerline in the initial stress-free configuration; (c) infinitesimal triangle with hypotenuse on the centerline in the current deformed configuration

configuration, which is described by conditions

$$u'_{s0} = \cos \varphi_0 - 1 \quad (3)$$

$$w'_{s0} = -\sin \varphi_0 \quad (4)$$

in which the prime denotes the derivative with respect to x . Relations (3)–(4) follow from the geometry of the infinitesimal triangle depicted in Fig. 1b. By definition, cross sections in the initial state are perpendicular to the initial centerline, and so the angle by which the tangent to the centerline deviates from the x axis is the same as the angle φ_0 by which the section deviates from the z axis.

In principle it is possible to specify only function φ_0 and construct u_{s0} and w_{s0} by integrating equations (3)–(4) with initial conditions $u_{s0}(0) = 0$ and $w_{s0}(0) = 0$. Alternatively, one can characterize the initial shape by specifying functions u_{s0} and w_{s0} , making sure that they satisfy the constraint $(1 + u'_{s0})^2 + w'^2_{s0} = 1$, and then evaluate function $\varphi_0 = -\arcsin w'_{s0}$. However, one should bear in mind that the description based on a given function φ_0 combined with relations (3)–(4) is fully general and permits arbitrary values of the “rotation” φ_0 , while the inverse relation $\varphi_0 = -\arcsin w'_{s0}$ is valid only as long as $\varphi_0 \in [-\pi/2, \pi/2]$. This is always true in the vicinity of the left end section but not necessarily along the whole beam. For instance, if we consider a circular arch of radius R , the initial shape is described by

$$\varphi_0(x) = \frac{x}{R} \quad (5)$$

$$u_{s0}(x) = R \sin \frac{x}{R} - x \quad (6)$$

$$w_{s0}(x) = R \left(\cos \frac{x}{R} - 1 \right) \quad (7)$$

from which

$$u'_{s0}(x) = \cos \frac{x}{R} - 1 \quad (8)$$

$$w'_{s0}(x) = -\sin \frac{x}{R} \quad (9)$$

Functions u_{s0} and w_{s0} defined in (6)–(7) satisfy the constraint $(1 + u'_{s0})^2 + w'^2_{s0} = 1$, but the corresponding function φ_0 can be evaluated as $-\arcsin w'_{s0}$ only for $x \leq \pi R/2$. If the centerline length L exceeds $\pi R/2$, one needs to modify the formula for the inversion of (4) accordingly and set $\varphi_0 = \pi + \arcsin w'_{s0}$ for $x \in [\pi R/2, 3\pi R/2]$ etc.

The “total” centerline displacements, u_s and w_s , and the “total” rotation, φ , are understood as changes between the fictitious straight state and the final deformed configuration. They differ from the initial values by increments

$$\Delta u_s = u_s - u_{s0} \quad (10)$$

$$\Delta w_s = w_s - w_{s0} \quad (11)$$

$$\Delta \varphi = \varphi - \varphi_0 \quad (12)$$

that represent the actual displacements and rotation. Similar relations can be written for the displacements of an arbitrary point, u and w , for which the subscript “s” is dropped. In analogy to (1)–(2), the displacements of an arbitrary point can be expressed in terms of the centerline displacements and sectional rotation as

$$u(x, z) = u_s(x) + z \sin \varphi(x) \quad (13)$$

$$w(x, z) = w_s(x) - z(1 - \cos \varphi(x)) \quad (14)$$

2.2 | Deformation variables

Let us proceed to the evaluation of strains. The sections are assumed to remain perpendicular to the centerline, and so the shear strains are neglected and it is sufficient to characterize the stretching in the direction parallel to the centerline. Consider a fiber segment parallel to the centerline and located at section x and at height z , which is in the reference straight configuration represented by an infinitesimal interval of length dx . In the deformed configuration, this segment is mapped on the hypotenuse of an orthogonal triangle with catheti $dx + du$ and dw and its length is

$$\overline{dx} = \sqrt{(dx + du)^2 + dw^2} = dx \sqrt{(1 + u')^2 + w'^2} \quad (15)$$

Making use of (1)–(2), we express the ratio between the current and reference fiber lengths as

$$\begin{aligned} \frac{\overline{dx}}{dx} &= \sqrt{(1 + u')^2 + w'^2} = \sqrt{(1 + u'_s + z\varphi' \cos \varphi)^2 + (w'_s - z\varphi' \sin \varphi)^2} = \\ &= \lambda_s + z\varphi' \end{aligned} \quad (16)$$

in which

$$\lambda_s = \sqrt{(1 + u'_s)^2 + w'^2_s} \quad (17)$$

is the centerline stretch.

When evaluating the actual physical stretch of a generic fiber, we need to take into account that the length of the considered fiber segment in the stress-free configuration is not dx but

$$dx_0 = (\lambda_{s0} + z\varphi'_0) dx = (1 + z\varphi'_0) dx \quad (18)$$

Here we have taken into account that

$$\lambda_{s0} = \sqrt{(1 + u'_{s0})^2 + w'^2_{s0}} = 1 \quad (19)$$

due to the constraint on the functions that define the initial shape (which follows from the assumption that coordinate x corresponds to the arc length measured along the centerline). Based on the above, the stretch of a generic fiber is given by

$$\lambda = \frac{\overline{dx}}{dx_0} = \frac{\lambda_s + z\varphi'}{1 + z\varphi'_0} = \frac{\lambda_s + z\kappa}{1 + z\kappa_0} \quad (20)$$

where $\kappa_0 = \varphi'_0$ is the initial curvature and $\kappa = \varphi'$ is the curvature in the deformed state. The fact that for $z = 0$ we obtain $\lambda = \lambda_s$ confirms that λ_s defined in (17) is the stretch evaluated at the centerline.

If we imagine the beam first as straight and then deform it to what we later consider as the initial configuration, the stretch would be given by $1 + z\kappa_0$. Measured with respect to the fictitious straight shape, the final stretch would be $\lambda_s + z\kappa$. However, since the fiber is actually stress-free in the initial (but curved) configuration, the effective stretch that it feels is the ratio $(\lambda_s + z\kappa)/(1 + z\kappa_0)$.

2.3 | Internal forces

The next step is to set up the expression for the strain energy of the deformed beam and identify the internal forces as the variables work-conjugate with the sectional deformation variables λ_s and κ . Since the stress state at each material point is considered as

uniaxial, it is sufficient to specify the strain energy density, \mathcal{E}_{int} , as function of the stretch, λ , and then integrate it over the volume. The density is understood here as strain energy per unit initial volume, i.e., volume in the stress-free but initially curved state of the beam. When integrating over the volume of the initially curved beam, we have to take into account that an infinitesimal segment of length dx measured along the centerline contains fibers whose length $(1 + z\kappa_0) dx$ varies as function of their distance from the centerline. The strain energy is therefore written as

$$E_{int} = \int_0^L \int_A (1 + z\kappa_0) \mathcal{E}_{int}(\lambda) dA dx \quad (21)$$

and its variation is

$$\delta E_{int} = \int_0^L \int_A (1 + z\kappa_0) \frac{\partial \mathcal{E}_{int}}{\partial \lambda} \delta \lambda dA dx \quad (22)$$

where A is the cross section and

$$\delta \lambda = \frac{\delta \lambda_s + z \delta \kappa}{1 + z\kappa_0} \quad (23)$$

is the variation of stretch. The derivative $\partial \mathcal{E}_{int} / \partial \lambda = \sigma$ is the stress work-conjugate with the Biot strain, because differentiation with respect to $\epsilon = \lambda - 1$ gives the same result as differentiation with respect to λ . This stress can be interpreted as the normal component of the back-rotated first Piola-Kirchhoff stress (where the back rotation eliminates the effects of the cross-sectional rotation).

The expression for the strain energy variation can be further converted into

$$\delta E_{int} = \int_0^L \int_A (1 + z\kappa_0) \sigma \frac{\delta \lambda_s + z \delta \kappa}{1 + z\kappa_0} dA dx = \int_0^L \int_A \sigma (\delta \lambda_s + z \delta \kappa) dA dx = \int_0^L (N \delta \lambda_s + M \delta \kappa) dx \quad (24)$$

in which

$$N = \int_A \sigma dA \quad (25)$$

$$M = \int_A z \sigma dA \quad (26)$$

are identified as the normal force and bending moment, playing the role of stress resultants that are work-conjugate with the centerline stretch and curvature.

If the expression for strain energy density is taken as quadratic, given by

$$\mathcal{E}_{int}(\lambda) = \frac{1}{2} E (\lambda - 1)^2 \quad (27)$$

where E is the Young modulus, the resulting stress-strain relation

$$\sigma = \frac{d\mathcal{E}_{int}(\lambda)}{d\lambda} = E(\lambda - 1) = E\epsilon \quad (28)$$

is linear in terms of the Biot strain $\epsilon = \lambda - 1$ and the (back-rotated) first Piola-Kirchhoff stress σ . However, since the distribution of stretches across the height of the section of an initially curved beam is not linear but is given by the rational function (20), the distribution of stresses across the section height is nonlinear even for this type of a linear stress-strain law, and it is given by

$$\sigma = E \left(\frac{\lambda_s + z\kappa}{1 + z\kappa_0} - 1 \right) = E \frac{\lambda_s - 1 + z(\kappa - \kappa_0)}{1 + z\kappa_0} = E \frac{\epsilon_s + z\Delta\kappa}{1 + z\kappa_0} \quad (29)$$

where

$$\epsilon_s = \lambda_s - 1 \quad (30)$$

is the strain at the centerline and

$$\Delta\kappa = \kappa - \kappa_0 \quad (31)$$

is the difference between the curvatures in the deformed state and in the stress-free state.

Substituting the stress expressed from (29) into the integral formulae for internal forces, eqs. (25)–(26), we obtain

$$N = \int_A \sigma \, dA = E \int_A \frac{\varepsilon_s + z\Delta\kappa}{1 + z\kappa_0} \, dA = E \int_A \frac{dA}{1 + z\kappa_0} \varepsilon_s + E \int_A \frac{z \, dA}{1 + z\kappa_0} \Delta\kappa \quad (32)$$

$$M = \int_A z\sigma \, dA = E \int_A \frac{z\varepsilon_s + z^2\Delta\kappa}{1 + z\kappa_0} \, dA = E \int_A \frac{z \, dA}{1 + z\kappa_0} \varepsilon_s + E \int_A \frac{z^2 \, dA}{1 + z\kappa_0} \Delta\kappa \quad (33)$$

The resulting sectional equations, i.e., relations between internal forces and sectional deformation variables, can be written as

$$N = EA_{\kappa_0} \varepsilon_s + ES_{\kappa_0} \Delta\kappa \quad (34)$$

$$M = ES_{\kappa_0} \varepsilon_s + EI_{\kappa_0} \Delta\kappa \quad (35)$$

where

$$A_{\kappa_0} = \int_A \frac{dA}{1 + z\kappa_0} \quad (36)$$

$$S_{\kappa_0} = \int_A \frac{z \, dA}{1 + z\kappa_0} \quad (37)$$

$$I_{\kappa_0} = \int_A \frac{z^2 \, dA}{1 + z\kappa_0} \quad (38)$$

are modified sectional characteristics, dependent on the initial curvature κ_0 . They remain constant during the simulation and thus can be computed in advance, so their evaluation does not represent any problem even for general sections. Moreover, by manipulating the integrals it is easy to show that $S_{\kappa_0} = -\kappa_0 I_{\kappa_0}$ and $A_{\kappa_0} = A - \kappa_0 S_{\kappa_0} = A + \kappa_0^2 I_{\kappa_0}$ where A is the standard sectional area. Therefore, it is sufficient to evaluate the modified moment of inertia, I_{κ_0} , and the modified area and modified static moment are then obtained in a straightforward way.

For a rectangular section, the modified moment of inertia can be expressed analytically:

$$I_{\kappa_0} = b_s \int_{-h_s/2}^{h_s/2} \frac{z^2 \, dA}{1 + z\kappa_0} = \frac{b_s}{\kappa_0^3} \left(\ln \frac{2 + h_s \kappa_0}{2 - h_s \kappa_0} - h_s \kappa_0 \right) = b_s h_s^3 \left(\frac{1}{12} + \frac{h_s^2 \kappa_0^2}{80} + \frac{h_s^4 \kappa_0^4}{448} + \dots \right) \quad (39)$$

The dimensionless product $h_s \kappa_0$ is equal to the ratio h_s/R_0 where $R_0 = 1/\kappa_0$ is the initial radius of curvature. If this ratio is 1:10, the relative difference between the modified moment of inertia I_{κ_0} and the standard moment of inertia $I = b_s h_s^3/12$ is just 0.1503 %. The approximation

$$I_{\kappa_0} \approx b_s h_s^3 \left(\frac{1}{12} + \frac{h_s^2 \kappa_0^2}{80} \right) = \frac{b_s h_s^3}{12} \left(1 + 0.15 \frac{h_s^2}{R_0^2} \right) \quad (40)$$

is then sufficiently accurate.

Sectional equations (34)–(35) have been derived using a rigorous procedure that combines (i) the definition of internal forces as stress resultants (25)–(26), (ii) the kinematic assumption of planar cross sections remaining planar, which leads to (20), and (iii) the linear uniaxial stress-strain law (28). If no further approximations are made, the consistently derived equations reflect a certain coupling between axial stretching and bending, in the sense that the normal force depends not only on the axial strain but also on the change of curvature, and the bending moment depends not only on the change of curvature but also on the axial strain. Of course, this is true for a beam with nonzero initial curvature. For a straight beam, sectional characteristics A_{κ_0} and I_{κ_0} are respectively equal to the standard area A and moment of inertia I , and S_{κ_0} vanishes because it corresponds to the static sectional moment $S = 0$. In this case, sectional equations (34)–(35) reduce to their simple form

$$N = EA \varepsilon_s \quad (41)$$

$$M = EI \Delta\kappa \quad (42)$$

in which the axial stretching and bending are decoupled. For curved beams, sectional equations in the decoupled form (41)–(42) need to be considered as a simplified version of the consistently derived equations (34)–(35), which is based on an approximation and introduces a certain error.

It is worth noting that the coupling between axial stretching and bending for curved beams is a phenomenon described in the literature but often ignored. The consistent sectional equations were, in a different notation, derived for instance by Bauer et al.¹⁸; see their equations (72)–(73). Similar issues arise also in shell theory. Detailed discussion of the appropriate form of sectional equations for curved beams is provided in Appendix A.

2.4 | Equilibrium equations

The equilibrium equations in their differential form could be derived from the stationarity conditions of the total potential energy functional using the standard variational approach. This procedure is described in detail in our previous paper¹ and it will not be repeated here because the resulting equations

$$-(N \cos \varphi)' - \left(\frac{M'}{\lambda_s} \sin \varphi \right)' = 0 \quad (43)$$

$$(N \sin \varphi)' - \left(\frac{M'}{\lambda_s} \cos \varphi \right)' = 0 \quad (44)$$

are exactly the same as equations (26)–(27) in¹. It is important to note that φ needs to be properly understood as the rotation of the section with respect to the fictitious straight configuration and not as the actual rotation with respect to the initial curved state, which would be $\Delta\varphi = \varphi - \varphi_0$. Furthermore, equations (43)–(44) can be integrated in closed form using the same approach as in¹, which finally leads to

$$N(x) = -X_{ab} \cos \varphi(x) + Z_{ab} \sin \varphi(x) \quad (45)$$

$$M(x) = -M_{ab} + X_{ab} w_s(x) - Z_{ab}(x + u_s(x)) \quad (46)$$

where X_{ab} , Z_{ab} and M_{ab} are integration constants that physically correspond to the end forces and end moment acting on the left end of the beam. Again, φ , u_s and w_s are the rotation and displacements with respect to the fictitious straight configuration, and the components of end forces are expressed with respect to the local xz coordinate system attached to the left end. Of course, equations (45)–(46) could be set up directly as equilibrium conditions deduced from a free-body diagram, but it is reassuring that they can be derived variationally and that the internal forces (primarily defined as work conjugates of the deformation variables) have indeed their usual meaning.

2.5 | Treatment of the governing equations

The approach used here when setting up the relations between the generalized end forces (i.e., end forces and moments) and the generalized end displacements (i.e., end displacements and rotations) follows the main idea described in¹. Instead of approximating the centerline displacement functions by a linear combination of pre-selected functions (e.g., polynomials) and enforcing equilibrium in the weak sense, we consider the integrated equilibrium equations (45)–(46) and combine them with the sectional constitutive equations (34)–(35) and with a set of three first-order differential equations

$$\varphi' = \kappa \quad (47)$$

$$u_s' = \lambda_s \cos \varphi - 1 \quad (48)$$

$$w_s' = -\lambda_s \sin \varphi \quad (49)$$

which link the centerline displacement functions u_s and w_s and the sectional rotation function φ to the deformation variables—centerline stretch λ_s and curvature κ . Equation (47) directly follows from the definition of the curvature, specified in the text after equation (20), while equations (48)–(49) follow from the geometry of an orthogonal triangle with hypotenuse given by a deformed centerline segment of length $\lambda_s dx$ inclined by φ with respect to the horizontal axis; see Fig. 1c.

One component of the outlined approach is the evaluation of the deformation variables from the internal forces, which is based on the inverted form of consistent sectional equations (34)–(35),

$$\varepsilon_s = \frac{I_{\kappa_0} N - S_{\kappa_0} M}{E(A_{\kappa_0} I_{\kappa_0} - S_{\kappa_0}^2)} \quad (50)$$

$$\Delta\kappa = \frac{-S_{\kappa_0} N + A_{\kappa_0} M}{E(A_{\kappa_0} I_{\kappa_0} - S_{\kappa_0}^2)} \quad (51)$$

Exploiting previously mentioned relations $S_{\kappa_0} = -\kappa_0 I_{\kappa_0}$ and $A_{\kappa_0} = A + \kappa_0^2 I_{\kappa_0}$, this can be rewritten as¹

$$\varepsilon_s = \frac{N + \kappa_0 M}{EA} \quad (52)$$

$$\Delta\kappa = \frac{\kappa_0 N}{EA} + \frac{M}{EI_{\kappa_0}} + \frac{\kappa_0^2 M}{EA} = \frac{M}{EI_{\kappa_0}} + \kappa_0 \varepsilon_s \quad (53)$$

If the consistent sectional equations (34)–(35) are replaced by their simplified form (41)–(42), the inverted relations read

$$\varepsilon_s = \frac{N}{EA} \quad (54)$$

$$\Delta\kappa = \frac{M}{EI} \quad (55)$$

One could now express the internal forces on the right-hand sides of (52)–(53) using the integrated equilibrium equations (45)–(46), and then transform the deformation variables ε_s and $\Delta\kappa$ into $\lambda_s = 1 + \varepsilon_s$ and $\kappa = \kappa_0 + \Delta\kappa$ and substitute the resulting expressions into the right-hand sides of (47)–(49). This would lead to a set of three ordinary differential equations for functions u_s , w_s and φ , with all the other unknown functions eliminated. However, for the purpose of numerical treatment, it is preferred to keep the equations separate and process them one by one, because the procedure will be more transparent and individual operations will retain a clear physical meaning.

Before we proceed with the details of numerical implementation, let us note that the proposed approach shares some common features with the technique developed by Saje²⁰ in a more general context of the Reissner beam model⁸, i.e., with shear distortion taken into account. Saje²⁰ started from a variational formulation based on the Hu-Washizu principle. The potential energy was written as the sum of (i) the strain energy dependent on functions that characterize deformation of individual beam segments (axial strain, curvature and shear distortion) and (ii) the load energy dependent on the displacement and rotation functions and on the generalized displacements at both end sections. Compatibility constraints that link the deformation and displacement functions were enforced by an additional term that contains two Lagrange multiplier functions, and the curvature was expressed directly as the derivative of rotation. The resulting functional was then reduced by imposing relations that correspond to some of the stationarity conditions (Euler-Lagrange equations). In particular, the axial strain and shear distortion were expressed in terms of the rotation and Lagrange multipliers, and the Lagrange multiplier functions were expressed in terms of their values at the left end and prescribed loads. The reduced functional was dependent on only one function—the rotation, and on eight discrete values—six generalized end displacements and two left-end values of Lagrange multiplier, which physically correspond to the left-end forces. The functional was then discretized by approximating the rotation function by a polynomial of degree $M - 1$ with M unknown coefficients. The discretized model has $M + 6$ degrees of freedom, because the unknown end rotations directly depend on the coefficients of the polynomial rotation approximation, and thus only four end displacements and two end forces need to be considered as additional degrees of freedom.

In the present context (of an Euler-Bernoulli beam model), the approach of Saje²⁰ would correspond to the second-order differential equation for the rotation function that can be constructed in the following way: Equation (47) is differentiated with respect to x , κ' is replaced by $\varphi_0'' + \Delta\kappa'$, $\Delta\kappa'$ is expressed as M'/EI using the differentiated form of (55), M' is then evaluated according to (46) with the derivatives u_s' and w_s' expressed by (48)–(49), and finally λ_s is written as $1 + \varepsilon_s$ where ε_s is set to N/EA according to (54) and N is expressed using (45). After a simple rearrangement, the resulting equation reads

$$EI\varphi'' + \left(1 + \frac{Z_{ab} \sin \varphi - X_{ab} \cos \varphi}{EA}\right) (X_{ab} \sin \varphi + Z_{ab} \cos \varphi) = EI\varphi_0'' \quad (56)$$

Instead of solving this equation in its weak form by constructing a polynomial approximation of function φ , in our approach we treat the original equations (45)–(49) and (52)–(53) separately, replace the first derivatives in (47)–(49) by finite differences, and handle the problem by marching from the left end to the right end without the need for solving a coupled set of equations. Of course, the left-end forces and moment still have to be determined iteratively, but the resulting set always consists of only three nonlinear algebraic equations, no matter how fine discretization we use along the beam. In contrast to that, the approach of Saje²⁰ leads to a coupled set of $M + 6$ nonlinear algebraic equations if the rotation function is approximated by a polynomial of

¹According to equation (52), the centerline strain is not proportional to the standard normal force N but to a certain combination of the normal force and bending moment, $N + \kappa_0 M$. This may evoke the notion of “effective membrane stress resultant” introduced by Simo and Fox¹⁹ in the context of shell analysis. However, it turns out that our corrective term $\kappa_0 M$ has a different origin. The relation between the present theory and the framework used by Simo and Fox¹⁹ is discussed in detail in Appendix A.

order $M - 1$. We also use the fully consistent inverted sectional equations (52)–(53) instead of their simplified form (54)–(55), which would follow from the formulation adopted by Saje.²⁰

Another potential advantage of our approach is that it can handle (with high precision) cases when the curvature varies along the beam in a non-smooth way, which would be quite hard to approximate by a polynomial. An example of such a problem will be presented in section 4.7.

3 | NUMERICAL PROCEDURES

3.1 | Choice of primary unknown functions

Based on the theoretical description developed in the preceding section, a natural choice of the primary unknown functions would be the centerline displacements u_s and w_s and the sectional rotation φ . However, we should bear in mind that these kinematic variables describe changes of the current beam state with respect to the fictitious straight state. A potential disadvantage of the approach based on such “total” displacements is that even the initial stress-free shape would be computed numerically with some error, even though functions u_{s0} , w_{s0} and φ_0 that characterize the stress-free state are assumed to be known. One also needs to take into account that since the computed “total” displacements and rotation at the right end of the beam, $u_s(L)$, $w_s(L)$ and $\varphi(L)$, are referred to the fictitious straight shape, they do not correspond to the actual displacements and rotation of the joint to which the right end is attached. The joint displacements and rotation are in fact $\Delta u_s(L)$, $\Delta w_s(L)$ and $\Delta \varphi(L)$. For instance, if the beam ends do not move at all, the target values that should be obtained by the shooting method (to be described in Section 3.2) would not be zero but $u_{s0}(L)$, $w_{s0}(L)$ and $\varphi_0(L)$. These corrections would need to be included in the expressions for the residual used by the shooting method.

The above considerations motivate an alternative choice of displacements and rotation with respect to the stress-free configuration, Δu_s , Δw_s and $\Delta \varphi$, as the primary unknown functions. In terms of these “true” displacements and rotation, equations (47)–(49) can be rewritten as

$$\Delta \varphi' = \Delta \kappa \quad (57)$$

$$\Delta u_s' = (1 + \varepsilon_s) \cos(\varphi_0 + \Delta \varphi) - \cos \varphi_0 \quad (58)$$

$$\Delta w_s' = -(1 + \varepsilon_s) \sin(\varphi_0 + \Delta \varphi) + \sin \varphi_0 \quad (59)$$

These equations have been obtained by combining (47)–(49) with (10)–(12), (3)–(4) and (30)–(31). Function φ_0 is known (it specifies the initial geometry) and the deformation variables ε_s and $\Delta \kappa$ are directly evaluated from N and M using (52)–(53). Of course, when the internal forces are computed based on equations (45)–(46), the displacements and rotation must be substituted in their total form, i.e., Δu_s , Δw_s and $\Delta \varphi$ must be increased by the known values of u_{s0} , w_{s0} and φ_0 .

3.2 | Shooting method

From the mathematical point of view, the problem that we need to solve looks like an initial value problem, because equations (57)–(59) are first-order differential equations for $\Delta \varphi$, Δu_s and Δw_s and the initial values $\Delta \varphi(0) = 0$, $\Delta u_s(0) = 0$ and $\Delta w_s(0) = 0$ are known (due to the definition of the local coordinate system that remains firmly attached to the left end section). However, in order to proceed with the integration, one also needs to know the left-end forces X_{ab} and Z_{ab} and the left-end moment M_{ab} , which are used when expressing the internal forces according to (45)–(46).

In the context of structural analysis, the beam under consideration is attached to joints that link it to other beams, and the joint displacements and rotations play the role of basic global unknowns. Therefore, a typical task at the beam element level is to evaluate the end forces and moments (at both ends) generated by prescribed displacements and rotations of the joints. Numerical treatment of this task can be based on a special version of the shooting method, i.e., of the method that converts a boundary value problem into an initial value problem with an iterative modification of those initial values that are not known. These values are first guessed and then repeatedly corrected until the boundary conditions on the opposite end of the interval are satisfied with sufficient accuracy. In the present setting, the left-end forces X_{ab} and Z_{ab} and the left-end moment M_{ab} need to be adjusted until the numerically computed displacements and rotation of the right end (with respect to the coordinate system attached to the left end) become equal to the target values determined from the prescribed joint displacements and rotations. This iterative process at the beam element level is embedded in the global iteration of joint displacements and rotations leading to satisfaction of joint equilibrium conditions.

To formalize the computational procedure outlined above, let us introduce the column matrix of the left end generalized forces,

$$\mathbf{f}_{ab} = \begin{pmatrix} X_{ab} \\ Z_{ab} \\ M_{ab} \end{pmatrix} \quad (60)$$

and the column matrix of the right end generalized displacements,

$$\mathbf{u}_b = \begin{pmatrix} u_b \\ w_b \\ \varphi_b \end{pmatrix} \quad (61)$$

Numerical integration along the beam, starting from zero values of generalized displacements at the left end and using generalized forces \mathbf{f}_{ab} , leads to the values of generalized displacements at the right end. This is formally described by the mapping

$$\mathbf{g}(\mathbf{f}_{ab}) = \begin{pmatrix} \Delta u_s(L; X_{ab}, Z_{ab}, M_{ab}) \\ \Delta w_s(L; X_{ab}, Z_{ab}, M_{ab}) \\ \Delta \varphi(L; X_{ab}, Z_{ab}, M_{ab}) \end{pmatrix} \quad (62)$$

where for instance $\Delta u_s(L; X_{ab}, Z_{ab}, M_{ab})$ means the value of function Δu_s at $x = L$ determined with the left end forces set to X_{ab} and Z_{ab} and the left end moment to M_{ab} .

For given values of \mathbf{u}_b , condition

$$\mathbf{g}(\mathbf{f}_{ab}) = \mathbf{u}_b \quad (63)$$

represents a set of three nonlinear equations for unknowns \mathbf{f}_{ab} . The solution is found by the Newton-Raphson method, using the recursive formula

$$\mathbf{f}_{ab}^{(k+1)} = \mathbf{f}_{ab}^{(k)} + \mathbf{G}^{-1} \left(\mathbf{f}_{ab}^{(k)} \right) \left(\mathbf{u}_b - \mathbf{g} \left(\mathbf{f}_{ab}^{(k)} \right) \right), \quad k = 0, 1, 2, \dots \quad (64)$$

where

$$\mathbf{G} = \frac{\partial \mathbf{g}}{\partial \mathbf{f}_{ab}} \quad (65)$$

is the Jacobi matrix of mapping \mathbf{g} .

Note that the target values of $\Delta u_s(L)$, $\Delta w_s(L)$ and $\Delta \varphi(L)$ are the true displacements and rotation of the joint attached to the right end of the beam. Of course, the displacement components must be taken with respect to the local beam coordinate system aligned with the left end. The advantage of the approach based on displacements and rotation with respect to the initial shape is that, for this choice, $\mathbf{g}(\mathbf{0}) = \mathbf{0}$ holds exactly, even when the mapping \mathbf{g} is evaluated numerically, and so for zero prescribed displacements of the joints, leading to $\mathbf{u}_b = \mathbf{0}$, equation (63) yields zero end forces, $\mathbf{f}_{ab} = \mathbf{0}$. This would not be the case if the numerical integration used the “total displacements” as primary unknowns, because the initial shape would not be captured exactly by the numerical approximation.

3.3 | Algorithms

A numerical algorithm for evaluation of function \mathbf{g} will be developed in Section 3.3.1 and the corresponding algorithm for evaluation of the Jacobi matrix \mathbf{G} will be described in Section 3.3.2. Approximation of the governing equations is based on finite difference expressions. The interval $[0, L]$ is divided into N segments of equal length $h = L/N$, which connect the grid points $x_i = ih$, $i = 0, 1, 2, \dots, N$. The approximate values of various quantities at point x_i will be denoted by subscript i . To increase the accuracy, in some cases it is beneficial to deal with approximate values at the midpoint of segment number i , which will be denoted by subscripts $i - 1/2$. Of course, the coordinates of the midpoints are given by $x_{i-1/2} = (i - 1/2)h$, $i = 1, 2, \dots, N$.

3.3.1 | Evaluation of right-end displacements and rotation

For a beam with arbitrary geometry, the initial shape is supposed to be described by given functions u_{s0} , w_{s0} and φ_0 , from which it is possible to derive the initial curvature function, $\kappa_0 = \varphi'_0$. In the special case of a circular arch, we have $\kappa_0 = 1/R_0 = \text{const.}$, where R_0 is the initial radius of curvature of the centerline. More precisely, $\kappa_0 = 1/R_0$ if the shape of the arch is convex (center of curvature above the arch), while $\kappa_0 = -1/R_0$ should be used if the shape is concave.

Based on the shape and dimensions of the cross section, one can determine the modified moment of inertia, $I_{\kappa 0}$, as function of the initial curvature. For a rectangular section, the exact expression (39) or its approximation (40) can be used. For other

sectional shapes, an appropriate analytical formula can be derived or, as the last resort, numerical evaluation of the integral in (38) can be performed. The algorithm also works with the standard sectional area, A .

Evaluation of right-end displacements and rotation for given left-end forces and moment and for left-end displacements and rotation set to zero can be described as follows:

1. Set initial values

$$\Delta u_0 = 0 \quad (66)$$

$$\Delta w_0 = 0 \quad (67)$$

$$\Delta \varphi_0 = 0 \quad (68)$$

$$M_0 = -M_{ab} \quad (69)$$

$$\kappa_{0,0} = \kappa_0(0) \quad (70)$$

$$\varepsilon_0 = (-X_{ab} + \kappa_{0,0}M_0)/EA \quad (71)$$

$$\Delta \kappa_0 = \kappa_{0,0}\varepsilon_0 + M_0/EI_{\kappa_0}(\kappa_{0,0}) \quad (72)$$

2. For $i = 1, 2, \dots, N$ evaluate

$$\Delta \varphi_{i-1/2} = \Delta \varphi_{i-1} + \Delta \kappa_{i-1} \Delta x/2 \quad (73)$$

$$\varphi_{i-1/2} = \varphi_0(x_{i-1/2}) + \Delta \varphi_{i-1/2} \quad (74)$$

$$N_{i-1/2} = -X_{ab} \cos \varphi_{i-1/2} + Z_{ab} \sin \varphi_{i-1/2} \quad (75)$$

$$\kappa_{0,i-1/2} = \kappa_0(x_{i-1/2}) \quad (76)$$

$$\varepsilon_{i-1/2} = (N_{i-1/2} + \kappa_{0,i-1/2}M_{i-1})/EA \quad (77)$$

$$\Delta u_i = \Delta u_{i-1} + [(1 + \varepsilon_{i-1/2}) \cos \varphi_{i-1/2} - \cos \varphi_0(x_{i-1/2})] \Delta x \quad (78)$$

$$\Delta w_i = \Delta w_{i-1} + [\sin \varphi_0(x_{i-1/2}) - (1 + \varepsilon_{i-1/2}) \sin \varphi_{i-1/2}] \Delta x \quad (79)$$

$$M_i = -M_{ab} + X_{ab}(w_0(x_i) + \Delta w_i) - Z_{ab}(x_i + u_0(x_i) + \Delta u_i) \quad (80)$$

$$\kappa_{0,i} = \kappa_0(x_i) \quad (81)$$

$$\varepsilon_i = (N_{i-1/2} + \kappa_{0,i}M_i)/EA \quad (82)$$

$$\Delta \kappa_i = \kappa_{0,i}\varepsilon_i + M_i/EI_{\kappa_0}(\kappa_{0,i}) \quad (83)$$

$$\Delta \varphi_i = \Delta \varphi_{i-1/2} + \Delta \kappa_i \Delta x/2 \quad (84)$$

3. The resulting values of right-end displacements and rotation are $u_b = \Delta u_N$, $w_b = \Delta w_N$ and $\varphi_b = \Delta \varphi_N$.

This algorithm has a similar structure to the procedure developed in¹ for a straight beam. It is fully explicit and at the same time second-order accurate because time derivatives are replaced either by central differences, or by a sequence of two half-steps that use a forward difference combined with a backward difference. For instance, equation (57) is integrated in two half-steps described by (73) and (84), the first one being based on a forward difference and the second on a backward difference. For an initially straight beam, the axial strain depends only on the normal force, which can be determined from the sectional rotation without knowing the displacements, and the curvature depends only on the bending moment, which can be determined from the displacements without knowing the rotation. In that case, integration of equation (57) in two half-steps described by (73) and (84) corresponds to the trapezoidal rule, and integration of equations (58)–(59) described by (78)–(79) corresponds to the midpoint rule. The initial curvature introduces a slight coupling but the effects of the normal force on the change of curvature and of the bending moment on the axial strain remain small. This is why the accuracy is not substantially compromised if

- the evaluation of the axial strain at midpoint described by (77) is based on the normal force at midpoint and the bending moment at the beginning of the segment, and
- the evaluation of the curvature change at the end of the segment described by (83) is based on the bending moment at the end of the segment combined with the normal force at midpoint; see (82).

Using this scheme, it is sufficient to evaluate the normal force only at the midpoint and the bending moment only at the end of the segment. One can avoid the evaluation of the bending moment and displacements at the midpoint and of the normal force at

the end of the segment, which would involve additional calculations without a substantial increase in accuracy. Note that $\varepsilon_{i-1/2}$ and ε_i computed in (77) and (82) are auxiliary variables, which are directly used in (78)–(79) and (83) but do not need to be stored. On the other hand, $\Delta\kappa_i$ evaluated in (83) is used not only in (84) but also in the next segment in (73) under the name of $\Delta\kappa_{i-1}$ (with the value of i incremented). In fact, one could proceed from $\Delta\varphi_{i-1/2}$ to $\Delta\varphi_{i+1/2}$ in one single step of length Δx and skip the evaluation of $\Delta\varphi_i$. A half-step is needed only in the first segment and the last one, to obtain $\Delta\varphi_N$ as one of the basic output variables.

3.3.2 | Jacobi matrix

The foregoing algorithm defines the mapping \mathbf{g} of the generalized left-end forces \mathbf{f}_{ab} on the generalized right-end displacements $\mathbf{g}(\mathbf{f}_{ab})$, which is needed for the evaluation of the left-hand side of (63). For iterative solution of equations (63) by the Newton-Raphson method, one also needs the Jacobi matrix of mapping \mathbf{g} , i.e., the matrix

$$\mathbf{G} = \frac{\partial \mathbf{g}}{\partial \mathbf{f}_{ab}} \quad (85)$$

which contains derivatives of the right-end displacements and rotation with respect to the left-end forces and moment.

The entries of the Jacobi matrix are evaluated numerically using the linearized version of the computational scheme. Suppose that the input values of left-end forces X_{ab} , Z_{ab} and M_{ab} are perturbed by infinitesimal increments dX_{ab} , dZ_{ab} and dM_{ab} . The corresponding infinitesimal changes of displacements and rotations along the beam can be computed from the linearized form of equations (73)–(84), which reads

$$d\varphi_{i-1/2} = d\varphi_{i-1} + d\kappa_{i-1}\Delta x/2 \quad (86)$$

$$dN_{i-1/2} = -dX_{ab}\cos\varphi_{i-1/2} + dZ_{ab}\sin\varphi_{i-1/2} + X_{ab}\sin\varphi_{i-1/2}d\varphi_{i-1/2} + Z_{ab}\cos\varphi_{i-1/2}d\varphi_{i-1/2} \quad (87)$$

$$d\varepsilon_{i-1/2} = (dN_{i-1/2} + \kappa_{0,i-1/2}dM_{i-1})/EA \quad (88)$$

$$du_i = du_{i-1} + [d\varepsilon_{i-1/2}\cos\varphi_{i-1/2} - (1 + \varepsilon_{i-1/2})\sin\varphi_{i-1/2}d\varphi_{i-1/2}] \Delta x \quad (89)$$

$$dw_i = dw_{i-1} - [d\varepsilon_{i-1/2}\sin\varphi_{i-1/2} + (1 + \varepsilon_{i-1/2})\cos\varphi_{i-1/2}d\varphi_{i-1/2}] \Delta x \quad (90)$$

$$dM_i = -dM_{ab} + dX_{ab}(w_0(x_i) + \Delta w_i) - dZ_{ab}(x_i + u_0(x_i) + \Delta u_i) + X_{ab}dw_i - Z_{ab}du_i \quad (91)$$

$$d\varepsilon_i = (dN_{i-1/2} + \kappa_{0,i}dM_i)/EA \quad (92)$$

$$d\kappa_i = \kappa_{0,i}d\varepsilon_i + dM_i/EI_{\kappa 0}(\kappa_{0,i}) \quad (93)$$

$$d\varphi_i = d\varphi_{i-1/2} + d\kappa_i\Delta x/2 \quad (94)$$

The values of du_0 , dw_0 and $d\varphi_0$ are set to zero, because the zero values of Δu_0 , Δw_0 and $\Delta\varphi_0$ are fixed; see (66)–(68). The value of dM_0 is set to $-dM_{ab}$, and $d\kappa_0$ is obtained as $\kappa_{0,0}d\varepsilon_0 - dM_{ab}/EI_{\kappa 0}(\kappa_{0,0})$ where $d\varepsilon_0 = -(dX_{ab} + \kappa_{0,0}dM_{ab})/EA$.

If we set $dX_{ab} = 1$ and $dZ_{ab} = dM_{ab} = 0$, the resulting values of du_N , dw_N and $d\varphi_N$ will correspond to the first column of the Jacobi matrix \mathbf{G} . They are evaluated using the adapted scheme with $d\kappa_0 = -\kappa_{0,0}/EA$ and

$$d\varphi_{i-1/2} = d\varphi_{i-1} + d\kappa_{i-1}\Delta x/2 \quad (95)$$

$$dN_{i-1/2} = -\cos\varphi_{i-1/2} + X_{ab}\sin\varphi_{i-1/2}d\varphi_{i-1/2} + Z_{ab}\cos\varphi_{i-1/2}d\varphi_{i-1/2} \quad (96)$$

$$d\varepsilon_{i-1/2} = (dN_{i-1/2} + \kappa_{0,i-1/2}dM_{i-1})/EA \quad (97)$$

$$du_i = du_{i-1} + [d\varepsilon_{i-1/2}\cos\varphi_{i-1/2} - (1 + \varepsilon_{i-1/2})\sin\varphi_{i-1/2}d\varphi_{i-1/2}] \Delta x \quad (98)$$

$$dw_i = dw_{i-1} - [d\varepsilon_{i-1/2}\sin\varphi_{i-1/2} + (1 + \varepsilon_{i-1/2})\cos\varphi_{i-1/2}d\varphi_{i-1/2}] \Delta x \quad (99)$$

$$dM_i = w_0(x_i) + \Delta w_i + X_{ab}dw_i - Z_{ab}du_i \quad (100)$$

$$d\varepsilon_i = (dN_{i-1/2} + \kappa_{0,i}dM_i)/EA \quad (101)$$

$$d\kappa_i = \kappa_{0,i}d\varepsilon_i + dM_i/EI_{\kappa 0}(\kappa_{0,i}) \quad (102)$$

$$d\varphi_i = d\varphi_{i-1/2} + d\kappa_i\Delta x/2 \quad (103)$$

The other two columns are obtained in an analogous fashion. In practice, the evaluation of (95)–(103) in a loop over $i = 1, 2, \dots, N$ is performed simultaneously with the evaluation of (73)–(84), so that various auxiliary values such as $\cos\varphi_{i-1/2}$, $\sin\varphi_{i-1/2}$ or $\varepsilon_{i-1/2}$ can be reused.

3.4 | Transformation to global coordinates

Suppose that the algorithms described in Section 3.3 have been implemented and equations (63) can be solved numerically based on the iterative scheme (64). The prescribed values of right-end displacements \mathbf{u}_b on the right-hand side of (63) as well as the resulting left-end forces \mathbf{f}_{ab} are expressed in a local coordinate system xz , with the origin located at the left end of the beam in the deformed configuration and with the x axis in the direction of the tangent to the deformed centerline at the left end. Now we need to link the local components of forces and displacements to the components expressed with respect to the global coordinate system used for the whole structural model, which will be denoted by a superscript G .

The initial geometry is described by global coordinates of the joints connected by the beam, i.e., x_a^G and z_a^G at the left end and x_b^G and z_b^G at the right end, and also by the beam length measured along the centerline, L , and by functions u_{s0} , w_{s0} , φ_0 and κ_0 that specify the curved shape of the beam. These functions are not independent, and in principle it would be sufficient to specify the curvature, κ_0 , because the rotation, φ_0 , could be computed by integrating κ_0 and imposing initial condition $\varphi_0(0) = 0$, and the functions describing the centerline, u_{s0} and w_{s0} , could be computed by integrating equations (3)–(4) and imposing initial conditions $u_{s0}(0) = 0$ and $w_{s0}(0) = 0$. Instead of performing these operations numerically or developing complicated rules for symbolic integration, the implementation in OOFEM^{21,22} leaves it up to the user to prepare all needed functions and specify them on input, making sure that they are consistent.

For the purpose of transformation between local and global coordinate systems, we need to characterize the angle α_{ab} by which the local axes are rotated (clockwise) with respect to the global axes. Suppose that α_{0ab} is the value of this angle in the initial stress-free state, which can be determined from the given geometrical data. During the deformation process, the local coordinate system rotates with the left end joint, and so

$$\alpha_{ab} = \alpha_{0,ab} - \varphi_a^G \quad (104)$$

where φ_a^G is the rotation of the left joint (positive counterclockwise). Another quantity that will play a role in the transformations is the angle by which the beam chord deviates from the local x -axis. The value of this angle in the initial stress-free state, denoted as β_{0ab} , can easily be deduced from the description of the initial beam shape.

As already explained in Section 2.1, the total transformation of the beam can be conceptually decomposed into two parts: (A) rigid-body motion and (B) pure deformation. We can imagine that during stage A the beam moves as a rigid body such that it gets translated by u_a^G and w_a^G and then rotated about the left end by φ_a^G counterclockwise. This part of the overall motion does not affect the deformation state of the beam and has no effect on the end forces and moments, provided that their components are expressed with respect to a coordinate system that rotates with the beam.

During stage B, the left end remains fixed while the right end is moved to its actual position in the deformed configuration and the right end section is rotated by $\varphi_b^G - \varphi_a^G$. The displacements of the right end experienced during this second stage and expressed with respect to the local coordinate system attached to the left end are

$$u_b = (u_b^G - u_a^G) \cos \alpha_{ab} + (w_b^G - w_a^G) \sin \alpha_{ab} + L_{ab}(\cos(\beta_{0ab} + \varphi_a^G) - \cos \beta_{0ab}) \quad (105)$$

$$w_b = -(u_b^G - u_a^G) \sin \alpha_{ab} + (w_b^G - w_a^G) \cos \alpha_{ab} + L_{ab}(\sin(\beta_{0ab} + \varphi_a^G) - \sin \beta_{0ab}) \quad (106)$$

where L_{ab} is the length of the initial chord, see (117), and the rotation is

$$\varphi_b = \varphi_b^G - \varphi_a^G \quad (107)$$

Therefore, if the global displacements and rotations are prescribed, they can be transformed into the local displacements and rotation of the right end with respect to the left end, which are assembled into the column matrix \mathbf{u}_b . The corresponding column matrix of left-end forces \mathbf{f}_{ab} , obtained by solving equations (62) and formally denoted as $\mathbf{g}^{-1}(\mathbf{u}_b)$, has components X_{ab} , Z_{ab} and M_{ab} . Here, M_{ab} is directly the end moment acting at the left end, while the end forces must be transformed into the global components

$$X_{ab}^G = X_{ab} \cos \alpha_{ab} - Z_{ab} \sin \alpha_{ab} \quad (108)$$

$$Z_{ab}^G = X_{ab} \sin \alpha_{ab} + Z_{ab} \cos \alpha_{ab} \quad (109)$$

Finally, equilibrium equations written for the whole beam lead to expressions for the right-end forces

$$X_{ba}^G = -X_{ab}^G \quad (110)$$

$$Z_{ba}^G = -Z_{ab}^G \quad (111)$$

and the right-end moment

$$M_{ba} = -M_{ab} + X_{ab}(w_{s0}(L) + w_b) - Z_{ab}(L + u_{s0}(L) + u_b) \quad (112)$$

The angle characterizing the initial deviation of the local axes from the global ones can be expressed as

$$\alpha_{0ab} = \gamma_{0ab} - \beta_{0ab} \quad (113)$$

where

$$\gamma_{0ab} = \arctan \frac{z_b^G - z_a^G}{x_b^G - x_a^G} \quad (114)$$

is the angle between the beam chord (straight line connecting the end joints) and the global axis x^G , and β_{0ab} is the angle between the beam chord and the tangent to the centerline at the left end; see Fig. 2. Recall that (x_a^G, z_a^G) and (x_b^G, z_b^G) are the global coordinates of the end joints a and b in the initial state.

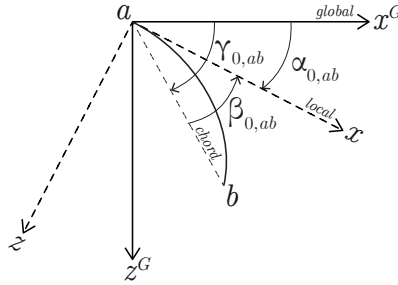


FIGURE 2 Local and global coordinate axes in the initial state and definition of angles $\alpha_{0,ab}$, $\beta_{0,ab}$ and $\gamma_{0,ab}$

Strictly speaking, formula (114) gives the correct result only if $x_b^G > x_a^G$ and, to make it general, the rule for evaluation of γ_{ab} would need to be split into several cases. However, for evaluation of the transformation formulae we will not really need the angle γ_{0ab} as such but rather its sine and cosine, which are conveniently expressed as

$$\cos \gamma_{0ab} = \frac{x_b^G - x_a^G}{L_{ab}} \quad (115)$$

$$\sin \gamma_{0ab} = \frac{z_b^G - z_a^G}{L_{ab}} \quad (116)$$

where

$$L_{ab} = \sqrt{(x_b^G - x_a^G)^2 + (z_b^G - z_a^G)^2} \quad (117)$$

is the initial chord length (distance between the end joints). These equations give the correct values of $\cos \gamma_{0ab}$ and $\sin \gamma_{0ab}$ including the signs for arbitrary inclinations of the chord.

In a similar fashion, the sine and cosine of angle β_{0ab} between the beam chord and the local axis (in the initial state) can be expressed as

$$\cos \beta_{0ab} = \frac{L + u_{s0}(L)}{L_{ab}} \quad (118)$$

$$\sin \beta_{0ab} = \frac{w_{s0}(L)}{L_{ab}} \quad (119)$$

Consistency requires that

$$(L + u_{s0}(L))^2 + w_{s0}^2(L) = L_{ab}^2 \quad (120)$$

Recall that L is the length of the beam measured along the curved centerline while the chord length L_{ab} represents the distance between the end joints, both in the initial stress-free state.

3.5 | Matrix formalism and stiffness matrix

It is convenient to rewrite relations (105)–(109) in the matrix notation:

$$\mathbf{u}_b = \mathbf{T}(\varphi_a^G)(\mathbf{u}_b^G - \mathbf{u}_a^G) + \mathbf{l}(\varphi_a^G) \quad (121)$$

$$\mathbf{f}_{ab}^G = \mathbf{T}^T(\varphi_a^G) \mathbf{f}_{ab} \quad (122)$$

where

$$\mathbf{T}(\varphi_a^G) = \begin{pmatrix} \cos(\alpha_{0,ab} - \varphi_a^G) & \sin(\alpha_{0,ab} - \varphi_a^G) & 0 \\ -\sin(\alpha_{0,ab} - \varphi_a^G) & \cos(\alpha_{0,ab} - \varphi_a^G) & 0 \\ 0 & 0 & 1 \end{pmatrix} \quad (123)$$

$$\mathbf{l}(\varphi_a^G) = L_{ab} \begin{pmatrix} \cos(\beta_{0ab} + \varphi_a^G) - \cos \beta_{0ab} \\ \sin(\beta_{0ab} + \varphi_a^G) - \sin \beta_{0ab} \\ 0 \end{pmatrix} \quad (124)$$

Recall that \mathbf{f}_{ab} and \mathbf{u}_b are the column matrices of local components defined in (60)–(61). The column matrices of global components are defined as

$$\mathbf{u}_a^G = \begin{pmatrix} u_a^G \\ w_a^G \\ \varphi_a^G \end{pmatrix}, \quad \mathbf{u}_b^G = \begin{pmatrix} u_b^G \\ w_b^G \\ \varphi_b^G \end{pmatrix}, \quad \mathbf{f}_{ab}^G = \begin{pmatrix} X_{ab}^G \\ Z_{ab}^G \\ M_{ab}^G \end{pmatrix} \quad (125)$$

For computing purposes, the coefficients in matrices \mathbf{T} and \mathbf{l} can be expanded into

$$\cos(\beta_{0ab} + \varphi_a^G) = \cos \beta_{0ab} \cdot \cos \varphi_a^G - \sin \beta_{0ab} \cdot \sin \varphi_a^G \quad (126)$$

$$\sin(\beta_{0ab} + \varphi_a^G) = \sin \beta_{0ab} \cdot \cos \varphi_a^G + \cos \beta_{0ab} \cdot \sin \varphi_a^G \quad (127)$$

$$\cos(\alpha_{0,ab} - \varphi_a^G) = \cos \alpha_{0,ab} \cdot \cos \varphi_a^G + \sin \alpha_{0,ab} \cdot \sin \varphi_a^G \quad (128)$$

$$\sin(\alpha_{0,ab} - \varphi_a^G) = \sin \alpha_{0,ab} \cdot \cos \varphi_a^G - \cos \alpha_{0,ab} \cdot \sin \varphi_a^G \quad (129)$$

where $\cos \beta_{0ab}$ and $\sin \beta_{0ab}$ are pre-computed constants given by (118)–(119) and

$$\cos \alpha_{0,ab} = \cos \gamma_{0ab} \cdot \cos \beta_{0ab} + \sin \gamma_{0ab} \cdot \sin \beta_{0ab} \quad (130)$$

$$\sin \alpha_{0,ab} = \sin \gamma_{0ab} \cdot \cos \beta_{0ab} - \cos \gamma_{0ab} \cdot \sin \beta_{0ab} \quad (131)$$

are pre-computed constants obtained from the constants given by (115)–(119).

Combining (121)–(122) with the inverse form of (63),

$$\mathbf{f}_{ab} = \mathbf{g}^{-1}(\mathbf{u}_b) \quad (132)$$

we get

$$\mathbf{f}_{ab}^G = \mathbf{T}^T(\varphi_a^G) \mathbf{g}^{-1}(\mathbf{T}(\varphi_a^G)(\mathbf{u}_b^G - \mathbf{u}_a^G) + \mathbf{l}(\varphi_a^G)) \quad (133)$$

This formula summarizes the process of evaluation of the left-end forces and moment from the end displacements and rotations. For better clarity, let us rewrite it in the simplified form

$$\mathbf{f}_{ab}^G = \mathbf{T}^T \mathbf{g}^{-1}(\mathbf{T}(\mathbf{u}_b^G - \mathbf{u}_a^G) + \mathbf{l}) \quad (134)$$

bearing in mind that matrices \mathbf{T} and \mathbf{l} depend on the left-end rotation, φ_a^G , which is at the same time the last component of column matrix \mathbf{u}_a^G .

The dependence of \mathbf{T} and \mathbf{l} on φ_a^G needs to be taken into account when developing the relation between infinitesimal increments of end displacements and end forces, which will provide an appropriate formula for the tangent element stiffness matrix.

The linearized form of equations (121)–(122) reads

$$d\mathbf{u}_b = \mathbf{T}(d\mathbf{u}_b^G - d\mathbf{u}_a^G) + (\mathbf{T}'(\mathbf{u}_b^G - \mathbf{u}_a^G) + \mathbf{l}') d\varphi_a^G \quad (135)$$

$$d\mathbf{f}_{ab}^G = \mathbf{T}^T d\mathbf{f}_{ab} + \mathbf{T}'^T \mathbf{f}_{ab} d\varphi_a^G \quad (136)$$

where

$$\mathbf{T}' = \frac{\partial \mathbf{T}(\varphi_a^G)}{\partial \varphi_a^G} = \begin{pmatrix} \sin(\alpha_{0,ab} - \varphi_a^G) & -\cos(\alpha_{0,ab} - \varphi_a^G) & 0 \\ \cos(\alpha_{0,ab} - \varphi_a^G) & \sin(\alpha_{0,ab} - \varphi_a^G) & 0 \\ 0 & 0 & 0 \end{pmatrix} \quad (137)$$

$$\mathbf{l}' = \frac{\partial \mathbf{l}(\varphi_a^G)}{\partial \varphi_a^G} = L_{ab} \begin{pmatrix} -\sin(\beta_{0ab} + \varphi_a^G) \\ \cos(\beta_{0ab} + \varphi_a^G) \\ 0 \end{pmatrix} \quad (138)$$

Combining this with the linearized version of (132),

$$d\mathbf{f}_{ab} = \mathbf{G}^{-1}(\mathbf{u}_b) d\mathbf{u}_b \quad (139)$$

we get

$$\begin{aligned} d\mathbf{f}_{ab}(\varphi_a^G) &= \mathbf{T}^T \mathbf{G}^{-1} [\mathbf{T}(d\mathbf{u}_b^G - d\mathbf{u}_a^G) + [\mathbf{T}'(\mathbf{u}_b^G - \mathbf{u}_a^G) + \mathbf{l}'] d\varphi_a] + \mathbf{T}'^T \mathbf{f}_{ab} d\varphi_a = \\ &= \mathbf{T}^T \mathbf{G}^{-1} \mathbf{T}(d\mathbf{u}_b^G - d\mathbf{u}_a^G) + [\mathbf{T}^T \mathbf{G}^{-1} [\mathbf{T}'(\mathbf{u}_b^G - \mathbf{u}_a^G) + \mathbf{l}'] + \mathbf{T}'^T \mathbf{f}_{ab}] d\varphi_a \end{aligned} \quad (140)$$

where \mathbf{G}^{-1} is the inverse of Jacobi matrix \mathbf{G} evaluated at $\mathbf{f}_{ab} = \mathbf{g}^{-1}(\mathbf{u}_b)$ where $\mathbf{u}_b = \mathbf{T}(\mathbf{u}_b^G - \mathbf{u}_a^G) + \mathbf{l}$.

Based on (140), we can set up the first three rows of the 6×6 element tangent stiffness matrix (in global coordinates). In view of (110)–(111), the fourth row is minus the first row, and the fifth row is minus the second row, because $dX_{ba}^G = -dX_{ab}^G$ and $dZ_{ba}^G = -dZ_{ab}^G$. To determine the sixth row, one needs to linearize the expression for M_{ba} . Instead of using (112), it is convenient to set up an equivalent formula written in terms of the global components. From the moment equilibrium condition written with respect to the centroid of the right end section in the deformed state, we get

$$M_{ba} = -M_{ab} + X_{ab}^G(z_b^G - z_a^G + w_b^G - w_a^G) - Z_{ab}^G(x_b^G - x_a^G + u_b^G - u_a^G) \quad (141)$$

and the infinitesimal increment of the right-end moment can be expressed as

$$\begin{aligned} dM_{ba} &= -dM_{ab} + (z_b^G - z_a^G + w_b^G - w_a^G)dX_{ab}^G - (x_b^G - x_a^G + u_b^G - u_a^G)dZ_{ab}^G + \\ &+ X_{ab}^G(dw_b^G - dw_a^G) - Z_{ab}^G(du_b^G - du_a^G) \end{aligned} \quad (142)$$

Consequently, the sixth row of the stiffness matrix can be constructed as a linear combination of the first three rows with coefficients $(z_b^G - z_a^G + w_b^G - w_a^G)$, $-(x_b^G - x_a^G + u_b^G - u_a^G)$ and -1 , resp., added to the row $(Z_{ab}^G, -X_{ab}^G, 0, -Z_{ab}^G, X_{ab}^G, 0)$. However, this does not even have to be done, since the stiffness matrix must be symmetric and we already have its sixth column, except for the last (i.e., diagonal) entry. So it is sufficient to mirror the entries from the sixth column into the sixth row and put

$$k_{66} = (z_b^G - z_a^G + w_b^G - w_a^G) k_{16} - (x_b^G - x_a^G + u_b^G - u_a^G) k_{26} - k_{36} \quad (143)$$

on the diagonal.

4 | NUMERICAL EXAMPLES

A nonlinear curved beam element based on the proposed approach has been implemented into OOFEM^{21,22}, an object-oriented finite element code. Even though the present formulation is not based on an interpolation of displacements and rotations using fixed shape functions multiplied by unknown nodal values, the element can still be incorporated into a structural model in the same way as conventional beam elements. For given input values of nodal (joint) displacements and rotations, the corresponding end forces and moments are evaluated and assembled into nodal equilibrium equations. Also, the corresponding 6×6 element tangent stiffness matrix is constructed and assembled (by standard procedures) into the structural tangent stiffness matrix used in global equilibrium iterations. The accuracy and efficiency of the suggested approach will now be demonstrated using seven examples.

The first four examples treat arches of a circular shape, for which functions φ_0 , u_{s0} and w_{s0} that characterize the initial geometry in terms of the arc-length coordinate are given by (5)–(7). The fifth example deals with a parabolic arch, and it shows that analogous closed-form expressions are in this case not available; therefore, it is explained how the description of the initial geometry can be handled numerically. The sixth example analyzes a logarithmic spiral, for which functions (157)–(159) describing the initial geometry are derived in Appendix B. Finally, the last example shows that the present formulation can

handle not only beams with a smooth centerline, but also cases in which the centerline exhibits kinks, e.g., a beam consisting of multiple straight segments. Even in this case, the whole beam can be treated as one element, and no intermediate nodes hosting additional global degrees of freedom need to be introduced.

4.1 | Symmetric circular arch, initial stiffness

It is well-known that curved finite elements suffer by excessive stiffness unless the axial displacement interpolation is of a sufficiently high order. When low-order axial displacement approximations are used, membrane locking makes it difficult for the elements to bend without stretching, and parasitic oscillating stresses may appear. This locking effect can be eliminated by using selectively reduced integration of the stiffness terms^{3,4}.

The present formulation exploits the equilibrium equations in their strong form and does not work with a priori chosen shape functions for the kinematic approximation, unlike standard displacement-based finite elements. In each integration segment, the values of curvature and axial strain are completely independent. The membrane locking effect is therefore not expected to occur, and accuracy can be increased simply by increasing the number of integration segments. This can be verified by analyzing the circular arch in Fig. 3a. The same problem was studied by Stolarski and Belytschko, who constructed a geometrically nonlinear model in the spirit of the shallow-shell approximation of Marguerre²³, first for a curved Euler-Bernoulli beam³ and then for a curved beam with shear distortion⁴.

To facilitate the comparison, let us take the geometrical and constitutive parameters from the original papers. They were specified in British units (inches and psi), which will be omitted here. The cross section is a rectangle of width $b_s = 1.2$ and depth $h_s = 0.125$, the radius of the undeformed centerline is $R_0 = 2.935$, and the elastic modulus is set to $E = 1.05 \times 10^7$ (which is the value for aluminum in psi). Symmetry is exploited, and so the numbers of elements reported below always correspond to one half of the structure. On the other hand, the applied force P is considered as the full load on the whole structure.

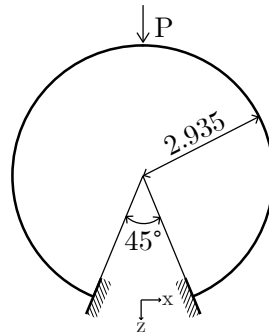


FIGURE 3 Symmetric circular arch: geometry

The complete load-deflection curve is nonlinear but locking phenomena can be detected already in the geometrically linear range, where the structural response is conveniently characterized by the load-deflection ratio, P/w , playing the role of the initial structural stiffness (i.e., the initial slope of the nonlinear load-deflection diagram). Here, w denotes the vertical deflection under the loading force, P . Stolarski and Belytschko³ reported the analytical value of the P/w ratio for the Euler-Bernoulli model to be equal to 471.09, but this value was actually based on the load acting on one half of the structure and later⁴ it was corrected to 942.2. However, our analytical calculation based on the force method indicates that, for a model that neglects the shear distortion and takes into account the axial and flexural deformation, the initial stiffness is 943.73. In this calculation, and also in the numerical simulations, the interaction between bending and axial deformation is neglected, so that the underlying theory remains the same as in the original papers by Stolarski and Belytschko^{3,4} and the results can be directly compared. This means that the consistent sectional equations (34)–(35) are replaced by their simplified form (41)–(42), which is reflected by appropriate modifications in lines (71)–(72), (77) and (82)–(83) of the algorithm (in fact, it is sufficient to set $\kappa_{0,i} = 0$, $i = 0, 1, 2 \dots N$). If the effect of shear distortion is added, the stiffness decreases to 941.11, provided that the Poisson ratio

$\nu = 0.3$ and the effective shear area is equal to the actual area, as assumed by Stolarski and Belytschko.⁴ With the shear area reduction factor set to the standard value for a rectangle, i.e., $5/6$, the resulting stiffness would be 940.59.

The results presented by Stolarski and Belytschko³ showed that a simulation on a mesh composed of eight curved finite elements with a linear approximation of the displacement component in the direction of the chord and a cubic approximation of the displacement perpendicular to the chord leads to an excessive structural stiffness if the integration scheme uses 4 or 3 Gauss integration points. The resulting P/w ratios were 1396.6 and 1405.1, respectively, which corresponds to relative errors of 48 % and 49 %. Reduced integration with 2 integration points per element resulted into $P/w = 900.26$, which is by 4.6 % lower than the exact value.

Stolarski and Belytschko⁴ analyzed the same problem using a slightly adjusted model with shear distortion taken into account and with the effective shear area considered as equal to the actual area. In this case, the theoretical stiffness is 941.11. The displacement-based element used a cubic interpolation for transverse displacements, quadratic for sectional rotations and linear for axial displacements. Eight elements with full integration would again lead to an excessive stiffness (1389.8, 48 % above the exact value) while a 2-point integration (which corresponds to reduced integration of the membrane terms and full integration of the shear terms) gives a substantial improvement (946.6, 0.6 % above). Various hybrid and mixed formulations were tested as well but none of them gave a closer approximation of the analytical result.

In our analyses, we used discretizations by one or two curved elements. It is remarkable that, for the one-element mesh, no global degrees of freedom were needed and the problem was solved simply by prescribing the end displacements and rotations and evaluating the corresponding end forces and moments. For the two-element mesh, only three global unknowns had to be introduced. Accuracy was increased by refining the integration segments and the full nonlinear model was used, but the initial load-deflection ratio was evaluated from the stiffness matrix computed in the undeformed configuration.

1 element			2 elements		
NIS	P/w	error [%]	NIS	P/w	error [%]
Exact	943.73				
4	632.01	33.031	2	633.33	32.891
8	839.37	11.058	4	839.82	11.010
16	915.23	3.020	8	915.36	3.007
32	936.44	0.773	16	936.47	0.769
64	941.90	0.194	32	941.91	0.193
128	943.27	0.049	64	943.28	0.048
256	943.62	0.012	128	943.62	0.012
$\rightarrow \infty$	943.73	0.000	$\rightarrow \infty$	943.73	0.000

TABLE 1 Symmetric circular arch: initial load-deflection ratios and the corresponding errors caused by numerical integration.

The results in Tab. 4.1 show that as the number of integration segments (NIS) is increased, the load-deflection ratio converges to the exact value, 943.73. Convergence is monotonic (from below) and fully regular. Asymptotically, quadratic convergence is observed, in the sense that the error is inversely proportional to the square of the NIS (i.e., when the NIS is doubled, the error is reduced by a factor close to 4). Solutions obtained on the one-element and two-element meshes are very similar, provided that the total number of integration segments is kept the same. The relative error obtained with one element divided into 16 integration segments (or for two elements, each divided into 8 segments) is about 3 % and it is lower than the error reported by Stolarski and Belytschko³ for 8 finite elements with reduced two-point integration, which required 18 global unknowns.

4.2 | Simply supported circular arch, internal forces

The second example corresponds to the cylindrical shell strip analyzed by Bieber et al.²⁴ in their section 4.3.1. Since the Poisson ratio was considered as zero, the problem is equivalent to the circular arch schematically shown in Fig. 4. The radius

of the undeformed centerline is $R_0 = 100$ while the sectional depth is just $h_s = 0.25$, which corresponds to a very slender arch. Bieber et al.²⁴ analyzed the structural response in an extremely large range of support displacements u up to 300, using 10 isogeometric NURBS elements of polynomial orders p varying between 2 and 15. They showed that the load-displacement curve becomes reasonably accurate already for $p = 4$ while the distribution of normal force exhibits wild oscillations even for $p = 10$, provided that the simplified formulation is used. With an improved formulation, Bieber et al.²⁴ were able to get substantially better results using low-order polynomials.

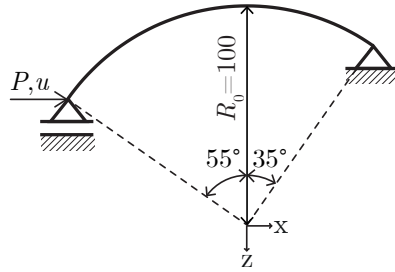


FIGURE 4 Simply supported circular arch: geometry and loading

We can analyze the same problem using again just one element. If the simulation is run under displacement control (prescribed displacement u at the left support), only two global unknowns are needed. To be consistent with example 4.3.1 in Bieber et al.²⁴, the elastic modulus is set to $E = 21000$, the sectional width to $b_s = 10$, and simplified sectional equations (41)–(42) are adopted. The load-displacement diagram plotted in Fig. 5a is in good agreement² with the results of Bieber et al.²⁴, and reasonable accuracy is attained already for 8 integration segments. Moreover, the distribution of normal forces shown in Fig. 5b is not polluted by any oscillations and exhibits fast convergence. To illustrate the convergence rate, the value of the normal force at the right support in the state at which the left support is displaced by $u = 100$ (i.e., near the first peak of the load-displacement diagram) is taken as a representative example. Values of this normal force computed for different numbers of integration segments (NIS) are reported in Tab. 2. Convergence is seen to be quadratic, i.e., of the same order as convergence in terms of displacements.

NIS	normal force	error [%]
4	0.03793	24.66
8	0.04723	6.20
16	0.04956	1.56
32	0.05015	0.39
$\rightarrow \infty$	0.05035	0.00

TABLE 2 Simply supported circular arch: normal force at the right support in the state when the displacement of the left support is $u = 100$, obtained numerically with different values of the number of integration segments (NIS), and the corresponding relative errors.

²It is worth noting that we report here the total force P acting on the beam of width $b_s = 10$ and the (total) normal force N , while Bieber et al.²⁴ reported the load multiplier λ and the specific normal force $n_{11} = N/b_s$. This is why our normal forces are 10 times larger than those in Figs. 27–29 in Bieber et al.²⁴ According to their Fig. 25, the load intensity was set to 0.1λ on a strip of width 10, and so the load multiplier λ should correspond to our load resultant, P . However, the values of λ in Fig. 26 in Bieber et al.²⁴ are 10 times smaller than the values of P in our Fig. 5a, which means that Bieber et al.²⁴ probably plotted the load intensity 0.1λ instead of the load multiplier.

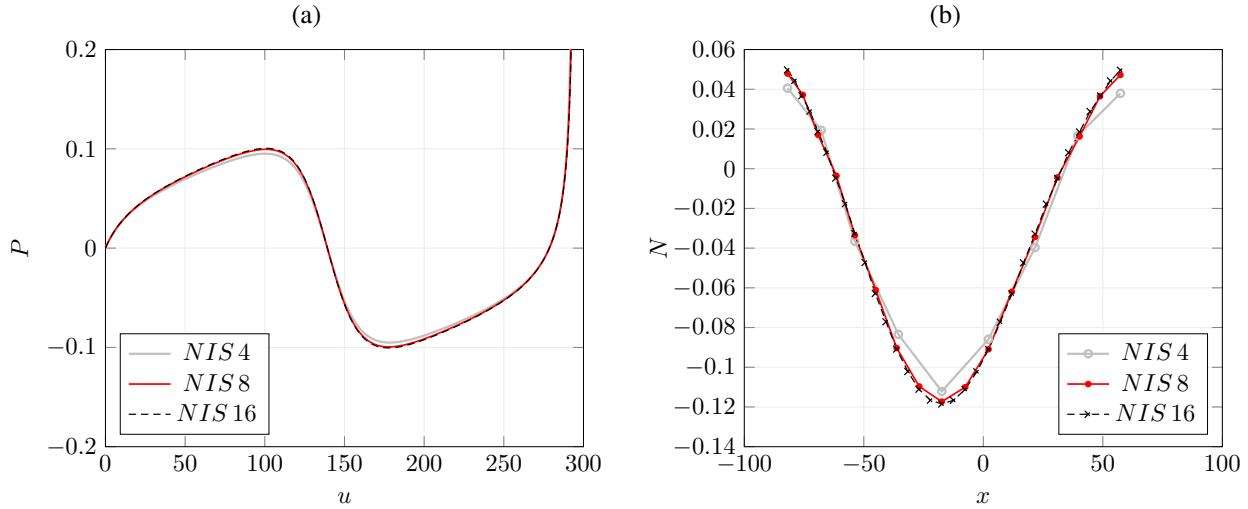


FIGURE 5 Simply supported circular arch: (a) load-displacement diagram, (b) distribution of normal force in the state characterized by $u = 100$, plotted as function of the global coordinate x marked in Fig. 4.

4.3 | Unfolding of a circular cantilever beam

In the previous examples, the sectional equations that link the internal forces to deformation variables were used in their simplified form (41)–(42), so that the results could be directly compared to those reported in the literature. For linear elastic beams, it is usually assumed that the bending moment is not affected by the axial strain and the normal force is not affected by the curvature. However, this can be rigorously proven only if the beam is initially straight. For beams with an initial curvature, we have derived consistent relations (34)–(35), which contain modified sectional characteristics and cross-coupling terms. Let us now explain the physical origin of these modifications and illustrate the resulting effects on the structural behavior. For this purpose, we will consider a curved cantilever which has the initial form of a full circle, cut at a certain section. One side of the cut is clamped and the other is loaded by an increasing bending moment, which gradually unfolds the beam to a straight configuration and subsequently folds it again to a circular shape with the opposite curvature.

Even though this fictitious test might seem to be the direct analog of the simple example of a straight cantilever folded to a circle by an end moment^{1,11}, the case of the initially curved beam is actually more involved. For pure bending (i.e., zero normal force) and a rectangular cross section of width b_s and depth h_s , the consistent inverted sectional equations (52)–(53) reduce to

$$\varepsilon_s = \frac{\kappa_0 M}{EA} = \kappa_0 \frac{M}{Eb_s h_s} \quad (144)$$

$$\Delta\kappa = \left(\frac{1}{EI_{\kappa_0}} + \frac{\kappa_0^2}{EA} \right) M = \frac{12 + h_s^2 \kappa_0^2 + 0.15 h_s^4 \kappa_0^4}{1 + 0.15 h_s^2 \kappa_0^2} \frac{M}{Eb_s h_s^3} \quad (145)$$

in which $\kappa_0 = 1/R_0$ is the initial curvature. Here we have taken into account that, for the rectangular section, the modified moment of inertia I_{κ_0} can be approximated by formula (40) and the standard sectional area is $A = b_s h_s$.

For an initially straight cantilever of length $L = 2\pi R_0$, the moment needed to fold the cantilever into a full circle would be $M_0 = EI\kappa_0 = EI/R_0$, and the radius of that circle would be R_0 . On the other hand, if the cantilever in its initial stress-free shape has the form of a circle of radius R_0 , application of moment $-M_0$ (the negative sign means that the moment acts clockwise) leads to the change of curvature

$$\Delta\kappa = -\frac{12 + h_s^2 \kappa_0^2 + 0.15 h_s^4 \kappa_0^4}{1 + 0.15 h_s^2 \kappa_0^2} \frac{EI\kappa_0}{Eb_s h_s^3} = -\frac{12 + h_s^2 \kappa_0^2 + 0.15 h_s^4 \kappa_0^4}{12 + 1.8 h_s^2 \kappa_0^2} \kappa_0 \quad (146)$$

and the resulting curvature

$$\kappa = \kappa_0 + \Delta\kappa = \frac{0.8 h_s^2 \kappa_0^2 - 0.15 h_s^4 \kappa_0^4}{12 + 1.8 h_s^2 \kappa_0^2} \kappa_0 \quad (147)$$

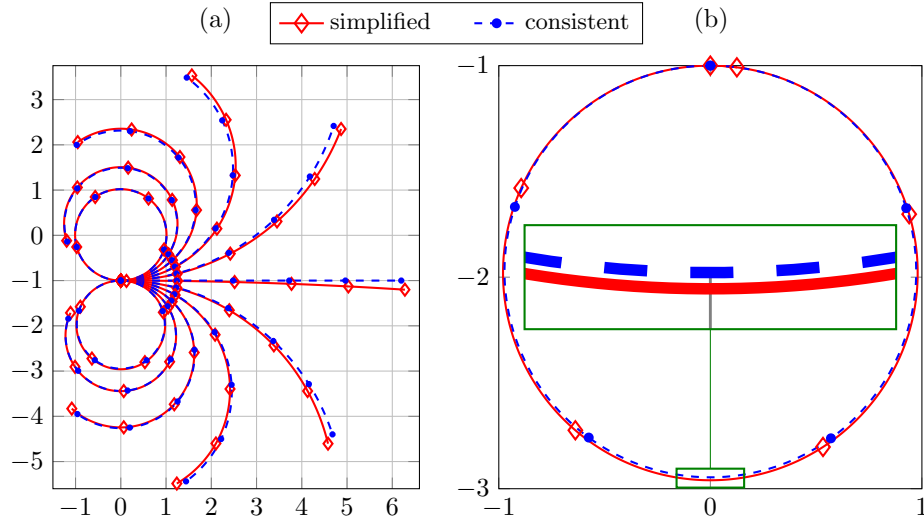


FIGURE 6 Comparison of the consistent and simplified theories for pure bending of a circular cantilever beam: (a) deformed configurations for an increasing end moment ranging from 0 to $-2M_1$, (b) closer look at the final stage.

is not zero. For instance, for $h_s = 0.4$ and $R_0 = 1$ we obtain $h_s\kappa_0 = h_s/R_0 = 0.4$ and $\kappa = 0.0101$. To get precisely zero curvature, the applied moment needs to be set to $-M_1$ where

$$M_1 = \frac{12 + 1.8 h_s^2 \kappa_0^2}{12 + h_s^2 \kappa_0^2 + 0.15 h_s^4 \kappa_0^4} EI \kappa_0 = \frac{12 + 1.8 h_s^2 \kappa_0^2}{12 + h_s^2 \kappa_0^2 + 0.15 h_s^4 \kappa_0^4} M_0 \quad (148)$$

Under this load, the initially curved cantilever becomes perfectly straight but its length does not remain equal to the initial centerline length $L = 2\pi R_0$ because the axial strain

$$\varepsilon_{s1} = \frac{\kappa_0}{Eb_s h_s} \cdot (-M_1) = -\frac{h_s^2 \kappa_0^2 + 0.15 h_s^4 \kappa_0^4}{12 + h_s^2 \kappa_0^2 + 0.15 h_s^4 \kappa_0^4} \quad (149)$$

is not zero. For our example with $h_s\kappa_0 = 0.4$, we obtain $\varepsilon_{s1} = -0.0135$.

The physical reason why the circular arch unfolded by a uniform moment into a straight beam tends to shrink is that if it did not, the compressive strain in the fibers that were initially on the outer surface and had initial length $2\pi(R_0 + h_s/2)$ would be $-h_s/(2R_0 + h_s)$ while the tensile strain in the fibers that were initially on the inner surface and had initial length $2\pi(R_0 - h_s/2)$ would be $h_s/(2R_0 - h_s)$, i.e., it would be higher in magnitude than the compressive strain. If the material law is linear elastic (in terms of the Biot strain and its work-conjugate stress), the same would hold for the stresses and the resulting normal force would be tensile. To get zero normal force, the centerline length must be reduced.

The case of a fully unfolded circle that still remains linear elastic in terms of the engineering strain and nominal stress may look purely academic, but the same argument applies even to much lower strain levels and thus the centerline would shrink at least during an initial stage of the unfolding process (see Appendix A for deeper analysis). This phenomenon is neglected by the widely used simplified theory, which is in many cases justified because the effect is indeed weak provided that $h_s\kappa_0 \ll 1$. The difference between M_1 and M_0 for $h_s\kappa_0 = 0.4, 0.2, 0.1$ and 0.05 is about 1 %, 0.3 %, 0.07 % and 0.02 %, respectively. However, note that the case of $h_s\kappa_0 = 0.4$ is not outside the range of what is normally considered as slender beams, because the total length of the circular centerline is $L = 2\pi R_0 = 2\pi/\kappa_0$ and thus the span-to-depth ratio of the unfolded cantilever is $L/h_s = 2\pi/(h_s\kappa_0) \approx 15.7$. In fact, the unfolding of a circular cantilever was studied in²⁵ using the simplified theory, with dimensions set to $L = 10$ and $h_s = 1$, which corresponds to $h_s\kappa_0 = 2\pi h_s/L \approx 0.628$. In this case, the described modification would play a significant role and the difference between M_1 and M_0 would be about 2.4 %.

Another (closely related) consequence of the coupling between membrane and bending effects is that if the applied moment is $-2M_1$, the curvature changes from κ_0 to $-\kappa_0$ and one may think that the centerline is located on a circle of radius R_0 (i.e., of the same radius as in the initial state), but in reality the radius is different. The reason is that, according to the definition adopted here, the curvature is equal to the derivative of rotation with respect to the arc length coordinate measured along the

initial centerline, but the arc length along the deformed centerline is different, since the axial strain is not zero. The actual radius of curvature under loading by constant moment $-2M_1$ leading to curvature $-\kappa_0$ and axial strain $2\varepsilon_{s1}$ is evaluated as

$$R = \left| \frac{(1 + 2\varepsilon_{s1}) dx}{d\varphi} \right| = \frac{1 + 2\varepsilon_{s1}}{\kappa_0} = (1 + 2\varepsilon_{s1}) R_0 \approx 0.973 R_0 \quad (150)$$

This means that if the consistent theory is used and moment $-2M_1$ is applied, the resulting shape is a perfectly closed circle of a smaller radius than the initial one, with the radius reduced by approximately 2.7 % (here we consider again our specific example with $h_s \kappa_0 = 0.4$).

The deformed shapes of the initially circular beam that correspond to the applied moment ranging from 0 to $-2M_1$ with step $-0.2 M_1$ are shown in Fig. 6. The solid red curves have been obtained using the simplified relations $N = EA \varepsilon_s$ and $M = EI \Delta \kappa$ while the dashed purple curves have been obtained with the consistent relations (34)–(35). In the middle of the deformation process, at applied moment $M = -M_1$, the current shape computed using the consistent theory is straight and the centerline length is slightly reduced as compared to the initial one. On the other hand, according to the simplified theory the centerline length would remain constant, and the current shape would be straight at applied moment $M = -M_0$ while at $M = -M_1$ it would be slightly curved. The markers plotted in Fig. 6 indicate the position of points that are initially regularly spaced on the centerline at $s = iL/5$ where $i = 0, 1, \dots, 5$.

The simulations also confirm the theoretical solution that corresponds to the ultimate stage of loading, with applied moment $-2M_1$; see the “lower” circle in Fig. 6a, which is also shown in more detail in Fig. 6b. For the consistent theory, the deformed shape plotted by the dashed blue line corresponds to a full circle of radius close to 0.973, as predicted in (150). On the other hand, the simplified theory would give a perfectly closed circle of the same radius as the initial one only if moment $-2M_0$ was applied. Under moment $-2M_1$ it gives a deformed centerline located on a circle of radius approximately $0.98 R_0$, plotted in Fig. 6 by the solid red line. As seen in Fig. 6b, this circle is “more than closed”, i.e., the free end of the cantilever initially located at the origin does not end up at the origin but is slightly shifted along the circle clockwise.

To provide not only a visual but also a quantitative assessment, the distances between the positions of the end point computed using the consistent and simplified theories at different levels of loading are evaluated in Table 3. The distance (i.e., the Cartesian norm of the difference between displacement vectors) is normalized here by the initial radius R_0 , so the values around 0.2 represent a considerable error.

$-M/M_1$	normalized error
0.2	0.0228
0.4	0.0660
0.6	0.1224
0.8	0.1780
1.0	0.2168
1.2	0.2279
1.4	0.2095
1.6	0.1726
1.8	0.1388
2.0	0.1256

TABLE 3 Pure bending of a circular cantilever beam subjected to an increasing end moment: Evaluation of the error in the displacement of the end point caused by replacement of the consistent theory by the simplified one (normalized by the circle radius R_0).

The deformed shapes in Fig. 6 and the error values in Table 3 are based on a highly accurate numerical solution with 1 element divided into 2048 integration segments. The dependence of the numerical error on the number of integration segments is illustrated in Table 4. The evaluated quantity w is the vertical displacement of the point initially located at $s = L/2$ caused by the applied moment $-M_1$ or $-2M_1$. At $M = -M_1$, the exact value of this displacement is $w = -2 R_0$, where $R_0 = 1$ in our

example. At $M = -2M_1$, a highly accurate computation yields $w = -3.94612 R_0$. The table confirms that asymptotically the error decreases in inverse proportion to the square of the number of integration segments.

Model	$M = -M_1$		$M = -2M_1$	
	w/R_0	error [%]	w/R_0	error [%]
Exact	-2	–	-3.946122	–
4 segments	-2.221453	11.07265	-4.383040	43.69177
8 segments	-2.052343	2.61715	-4.049401	10.32787
16 segments	-2.012914	0.64570	-3.971593	2.54707
32 segments	-2.003215	0.16075	-3.952468	0.63457
64 segments	-2.000802	0.04010	-3.947707	0.15847
128 segments	-2.000201	0.01005	-3.946518	0.03957
256 segments	-2.000050	0.00249	-3.946221	0.00987
512 segments	-2.000012	0.00060	-3.946147	0.00247
1024 segments	-2.000003	0.00015	-3.946128	0.00057
2048 segments	-2.000001	0.00005	-3.946124	0.00017

TABLE 4 Pure bending of a circular cantilever beam subjected to end moment $-M_1$ or $-2M_1$: Evaluation of errors in vertical displacement caused by numerical integration along the beam element.

All results presented so far have been obtained for a discretization of the entire circular cantilever by 1 curved element. Consider now the effect of mesh refinement. For curved elements, the initial geometry is reproduced exactly and no extra benefit would be gained by using several elements, provided that the total number of integration segments would remain the same. This has already been illustrated for the previous example in Table 4.1. On the other hand, if the initial circular shape is approximated by straight elements, the initial curvature of each element will be zero and the expressions for internal forces will have the simplified form (the information about initial curvature is transformed into jumps in the centerline slope between neighboring elements). Upon mesh refinement, the initial centerline geometry approximated by a polygon will converge to a circle, but the numerical solutions obtained for the deformed shape will converge to a limit that corresponds to the simplified theory, which neglects the effect of initial curvature on the relations between internal forces and deformation variables. This paradox is related to the fact that if the curved beam is approximated by straight elements that connect nodes located at the curved centerline, the total length of the polygonal approximation properly converges to the length of the curved centerline, and the length of fibers located at a given nonzero distance from the centerline converges to the same limit, which is however different from the actual length of those fibers on the curved beam. This fact is schematically illustrated in Fig. 7, which shows the circular arch (Fig. 7a) and its approximation by eight straight elements of the standard type (Fig. 7b). A gradual change of the inclination angle of individual sections is replaced by jumps at element interfaces. The arrangement of rectangular domains representing individual elements leads to gaps and overlaps, the area of which does not vanish in the limit as the element size tends to zero.

To get the proper limit even with straight elements, one would need to abandon the idea that individual sections are initially perpendicular to the centerline and consider non-parallel end sections as shown in Fig. 7c. In this way, the information on the variable fiber length could be incorporated into the model, but instead of this artificial adjustment it is better to use fully consistent curved elements.

4.4 | Asymmetric circular arch, complete load-displacement curve

The third example is representative of an arch instability after large deflections. The structural setup is similar to the arch analyzed in Section 4.1 but the supports are not symmetric and the dimensions are different. This particular structure was investigated by several authors^{2,11,26} and the solution based on Euler's nonlinear theory of the inextensible curved elastica was evaluated by DaDeppo and Schmidt²⁷, who reported a value of the maximum load equal to $8.97 EI/R^2$. The theory they used was exact in

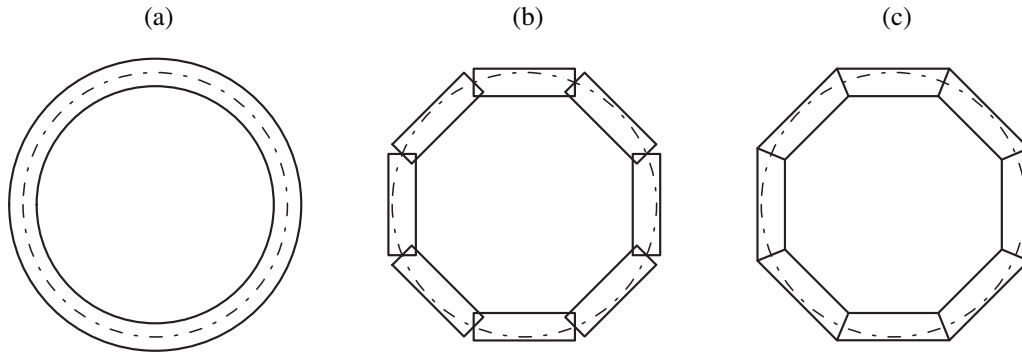


FIGURE 7 Geometry of a circular arch: (a) Exact, (b) approximated by straight beam elements with the same length of all longitudinal fibers, (c) approximated by straight beam elements with variable length of longitudinal fibers.

the sense that no restrictions were imposed on the magnitudes of deflections²⁸. The nonlinear boundary-value problem of the inextensible elastica was solved numerically to a high degree of accuracy, which was confirmed by comparisons with certain exact solutions of other problems previously derived by the same authors²⁹.

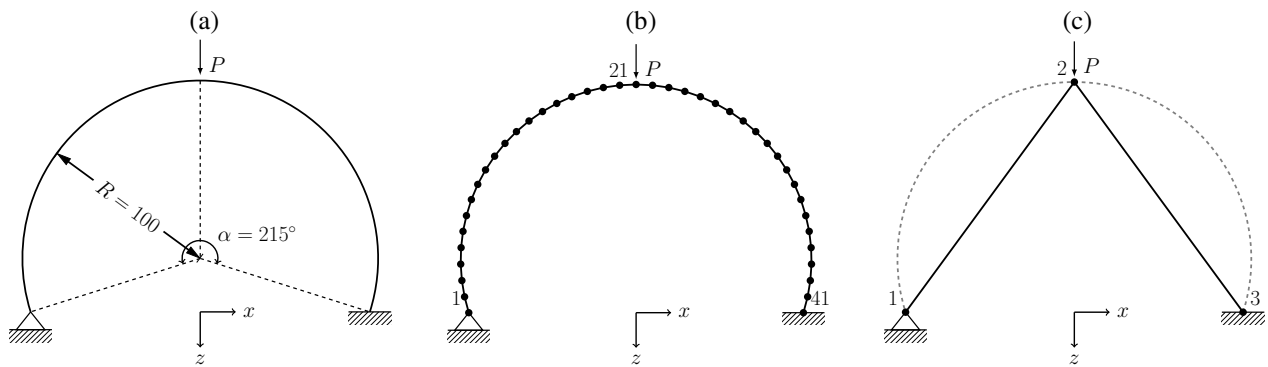


FIGURE 8 Asymmetric circular arch: (a) Geometry, (b) forty-element mesh used by Simo and Vu-Quoc¹¹, (c) two-element mesh used by the present curved beam formulation.

The arch is circular with one boundary hinged and the other clamped, and it is loaded by a vertical concentrated load applied at the top, as shown in Fig. 8a. In calculations presented in the literature, the structure was usually considered as very slender, so that the solution obtained for the axially incompressible case with neglected shear distortion could be used as a reference. However, the specific values of parameters are in some cases hard to find.

Wood and Zienkiewicz²⁶ obtained a buckling load of $9.24 EI/R^2$ using a mesh consisting of sixteen 2D six-noded parilinear elements (linear approximation in the direction of thickness and quadratic in the longitudinal direction), and one 2D three-noded linear element near the hinged support. Overall, their mesh had 67 nodes with 127 global unknowns, and they analyzed an arch of depth $h_s = 1$, which corresponds to $h_s \kappa_0 = 0.01$.

Simo and Vu-Quoc¹¹ performed their analysis with a mesh consisting of forty straight beam elements (Fig. 8b) and found a maximum load of $9.0528 EI/R^2$. A similar result was obtained with straight elements by Ibrahimbegović²⁵, who also reported a great improvement with twenty 3-node curved elements. The resulting maximum load of $8.973 EI/R^2$ was very close to the reference value published by DaDeppo and Schmidt.

In our analysis, we have used the minimum number of elements required to discretize the structure, which results in a two-element mesh shown in Fig. 8c, with only four global unknowns—two displacements and the rotation at the loaded node plus the rotation at the left support. The analysis has been performed under indirect displacement control, with the load iteratively

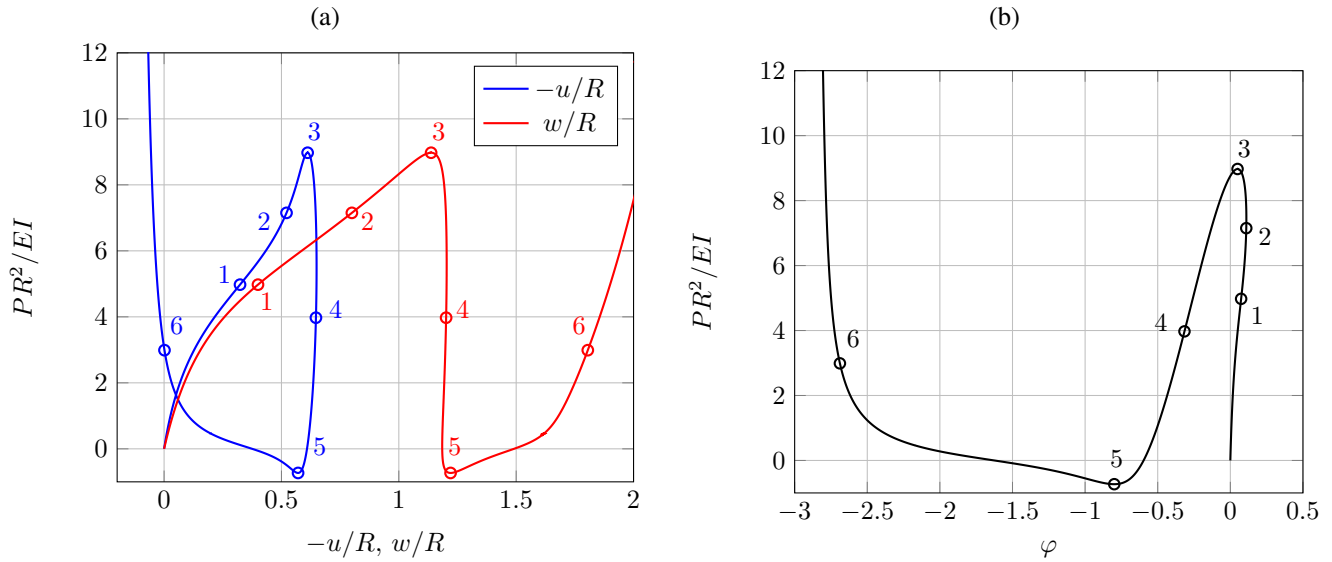


FIGURE 9 Asymmetric circular arch: (a) Load-displacement curves and (b) load-rotation curve for the top of the arch (node 2 in Fig. 8c)

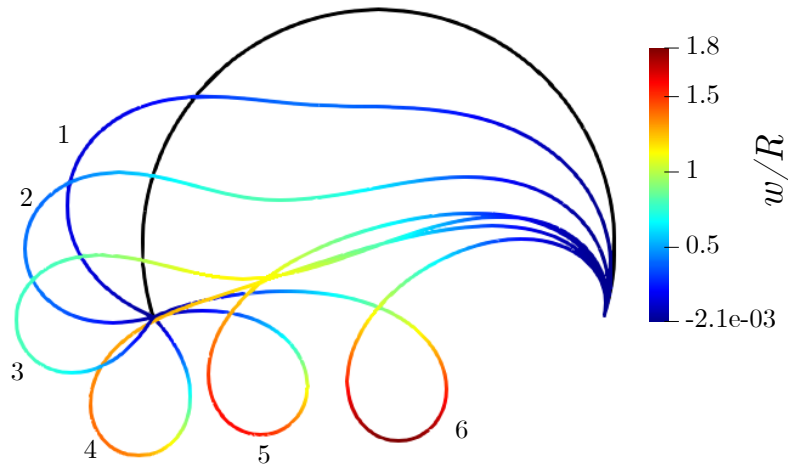


FIGURE 10 Asymmetric circular arch: Deformed shapes and normalized vertical displacement along the arch for the six states labeled by numbers 1–6 in Fig. 9.

adjusted such that the rotation at the left support increases by prescribed increments. Direct displacement control based on prescribed increments of the vertical displacement under the applied force is not advisable because the corresponding load-displacement diagram, plotted by the red line in Fig. 9a, exhibits a section with a very steep drop and even a slight snapback (see the path 3-4-5 in the figure).

The simulation has been done with the same sectional stiffnesses as in²⁵, namely $EA = 10^8$ and $EI = 10^6$, which correspond to a section of depth $h_s = \sqrt{0.12} \approx 0.3464$ and thus to $h_s \kappa_0 \approx 0.003464$. The numerical solution naturally depends on the number of segments used for integration of the governing equations on the element level. As seen in Table 4.4, the accuracy of the present simulation is higher than in²⁶ if 10 integration segments are used and higher than in¹¹ if 20 integration segments are used.

Further refinement of the integration grid leads again to quadratic convergence. The error is calculated by considering a highly accurate limit value of 8.972922, obtained by refinement until the resulting maximum load stabilizes up to seven valid digits.

This limit is in good agreement with the truncated value of 8.97 reported by DaDeppo and Schmidt²⁷, and it perfectly agrees with the value of 8.973 reported by Ibrahimbegović²⁵. One should note that²⁵ used shear-flexible elements and the actual limit value would be in that case slightly lower.

In the simulations reported in Table 4.4, the simplified relations between internal forces and deformation variables have been used. Since, for the given input data, $h_s \kappa_0 \ll 1$, the results obtained with the consistent relations would be only slightly different. The maximum load calculated with very high accuracy would change from 8.972922 to 8.972950 if the consistent relations are used.

The load-displacement curves plotted in Fig. 9 indicate that the arch exhibits a snap-through behavior after reaching the peak load at the state marked by label 3. The last physically reasonable numerical solution is obtained at the state marked by label 4. The simulation can be continued without problems but the deformed structure passes across the left support (see Fig. 10). This aspect was investigated by Simo et al.³⁰, who showed that a contact constraint condition on the left support needs to be introduced to obtain a more realistic solution. Here, we have not considered contact activation and the subsequent stiffening effect in the structure because these phenomena are out of scope of the present study.

Model	N° global unknowns	$P_{cr} R^2 / EI$	error [%]
DaDeppo and Schmidt ²⁷		8.97	
Wood and Zienkiewicz ²⁶	127	9.24	
Simo and Vu-Quoc ¹¹	117	9.0528	
Ibrahimbegović ²⁵		8.973	
present approach, 10 segments	4	8.735135	2.650
20 segments	4	8.912875	0.669
40 segments	4	8.957865	0.168
80 segments	4	8.969161	0.0420
160 segments	4	8.971979	0.0105
320 segments	4	8.972686	0.00263
640 segments	4	8.972863	0.00066
$\rightarrow \infty$	4	8.972922	0

TABLE 5 Asymmetric circular arch: Evaluation of errors in maximum load caused by numerical integration along the beam element and comparison with results from the literature.

4.5 | Parabolic arch

In the previous three examples, the initial shape was supposed to be circular and its analytical description was based on formulae (5)–(7). Let us now consider a parabolic arch. In the simplest case, when the left end of the parabolic beam element is located at the apex of the parabola, functions u_{s0} and w_{s0} that characterize the initial undeformed shape must satisfy the equation

$$w_{s0} = \frac{a}{2} (x + u_{s0})^2 \quad (151)$$

where a is a given geometric parameter. These functions are also constrained by the condition

$$(1 + u'_{s0})^2 + w'^2_{s0} = 1 \quad (152)$$

which follows from the fact that differential segments in the fictitious straight configuration have the same length as in the initial undeformed configuration. Taking the derivative of (151) and substituting into (152), we obtain after rearrangement

$$\sqrt{1 + a^2 (x + u_{s0})^2} (1 + u'_{s0}) = 1 \quad (153)$$

and integration after separation of variables leads to

$$a(x + u_{s0})\sqrt{1 + a^2(x + u_{s0})^2} + \operatorname{arcsinh}(a(x + u_{s0})) = 2ax \quad (154)$$

This equation implicitly defines function $u_{s0}(x)$ but the closed-form expression for this function is not available. Still, equation (154) could be solved numerically for each prescribed value of x_i and the corresponding $u_{s0}(x_i)$ could be evaluated. In this way, the analytical description of the initial shape would be replaced by a precomputed table of values of x_i and $u_{s0}(x_i)$ for all points of the integration grid. It is then easy to evaluate the corresponding $w_{s0}(x_i)$ from (151) and the “initial rotations $\varphi_0(x_i)$ from

$$\varphi_0(x) = -\arctan a(x + u_{s0}) \quad (155)$$

The procedure described above can be used to ensure uniform spacing of the grid points, which was assumed in the algorithms described in Section 3.3. As an alternative, one can prescribe uniform spacing in projection of the curved beam element onto the local x axis, which coincides with the tangent to the centerline constructed at the left end. In this case, the prescribed values are $x_i + u_{s0}(x_i) = ih_p$, $i = 0, 1, 2, \dots, N$, where $h_p = L_p/N$ is the projected integration segment length derived from the projected element length, L_p . The corresponding values of x_i are then directly obtained from (154) by evaluating the expression on the left-hand side and dividing by $2a$. Afterwards, $u_{s0}(x_i) = ih_p - x_i$ can be determined and the corresponding values $w_{s0}(x_i)$ and $\varphi_0(x_i)$ are calculated as usual from (151) and (155). All this can be done “on the fly” and there is no need to solve nonlinear equations and store a precomputed table of values. In the algorithms, the constant segment length h needs to be replaced by a variable length h_i , computed for each integration segment separately as the Euclidean distance between points with coordinates $((i-1)h_p, w_{s0}(x_{i-1}))$ and $(ih_p, w_{s0}(x_i))$. In theory, this may slightly disturb the quadratic convergence rate when the number of segments increases, since the integration of curvature is no longer based on a central difference scheme. However, no problems have been observed in the specific calculations to be reported next.

For these calculations, we adopt an example of a parabolic arch from¹⁴ and investigate two selected geometries. One, characterized by $H = 0.25$ m, corresponds to a shallow arch, and the other, with $H = 0.5$ m, to a deeper one. The cross section is a square with $b_s = h_s = 0.2$ m and the elastic modulus is $E = 10^4$ MPa.

It is well known that the load-displacement curves of shallow arches typically exhibit snap-through followed by an unstable branch and eventually by restoration of stable equilibrium, while the behavior of deep arches is more complex, with the so-called looping of the load-displacement curve³¹. The aim of this example is to demonstrate that the proposed formulation is able to capture such phenomena. The arch is simply supported and loaded by a concentrated force acting at midspan. Symmetry is exploited and only one half of the arch is simulated, which means that a possible bifurcation into a nonsymmetric shape is ignored.

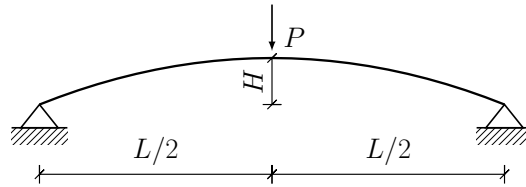


FIGURE 11 Parabolic arch: Geometry and loading, with $L = 10$ m, $H = 0.25$ m for the shallow arch and $H = 0.5$ m for the deeper arch.

The response of the shallow arch is described by the diagrams in Fig. 12a,c. The load-displacement curve (Fig. 12a) shows excellent agreement with the results reported in¹⁴, where isogeometric analysis was used. To illustrate the deformation process, the deformed shapes corresponding to four selected states that are marked by special symbols in the load-displacement curve are presented in Fig. 12c: the initial state (black), the state at peak load and onset of snap-through instability (red), the state at the end of the unstable branch (blue), and a stable state attained at displacement $w = 0.5$ m (green).

In a similar fashion, the response of the deeper arch is described by the diagrams in Fig. 12b,d. In contrast to the shallow arch, the vertical displacement under the load does not increase monotonically and the snapback phenomenon is observed in addition to the snap-through. The simulation cannot be performed under direct displacement control and an arc-length technique is needed. Still, the complicated load-displacement diagram can be captured and the results nicely agree with those from¹⁴.

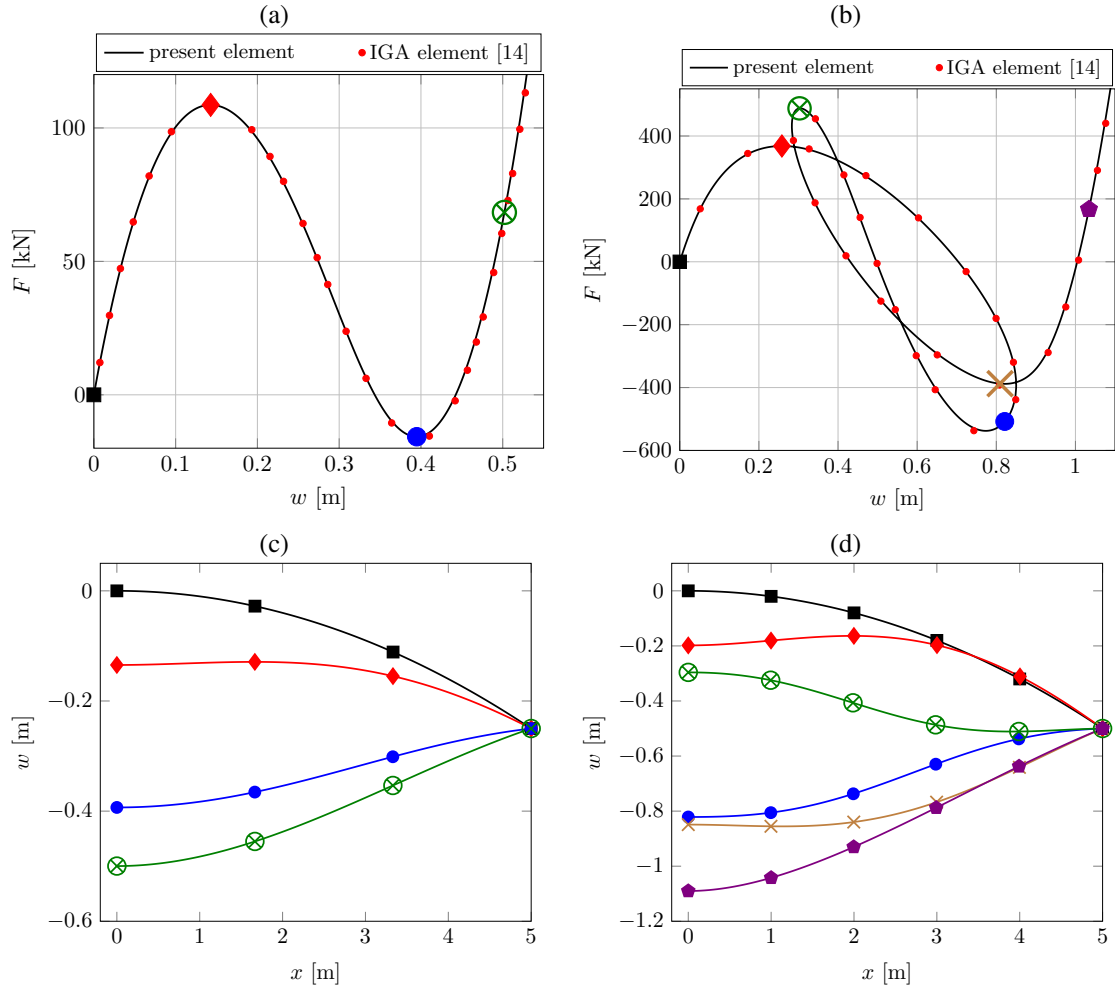


FIGURE 12 Parabolic arch: Load-displacement diagrams (a) for the shallow arch and (b) for the deeper arch, and deformed shapes (c) for the shallow arch and (d) for the deeper arch.

4.6 | Logarithmic spiral

The last example presents an extreme case of a highly curved beam, which has the initial shape of a planar spiral. It would not be so easy to properly approximate such a “structure” by straight elements or by shallow curved elements. Using the present approach, the whole spiral can be represented by one single element and its shape can be taken into account precisely, independently of the total number of loops.

The spiral considered in this example is a logarithmic one, and in polar coordinates (r, θ) it is described by

$$r = a e^{b\theta} \quad (156)$$

where a and b are positive parameters. Fig. 13 depicts the shape of the spiral obtained for $b = 0.15$ and $\theta \in [0, 4\pi]$. Parameter a sets the length scale and determines the distance of the clamped end of the spiral (at $\theta = 0$) from the pole.

For the logarithmic spiral, it is possible to derive closed-form expressions for functions that describe the initial shape with respect to local Cartesian coordinates with the origin at the left end of the spiral and with the local x axis in the tangential direction. The details of the derivation are provided in Appendix B. The resulting expressions read

$$\varphi_0(x) = \frac{\ln(1 + cx)}{b} \quad (157)$$

$$u_{s0}(x) = a \left((1 + cx) \sin(\varphi_0(x) + \varphi^*) - \sin \varphi^* \right) - x \quad (158)$$

$$w_{s0}(x) = a \left((1 + cx) \cos(\varphi_0(x) + \varphi^*) - \cos \varphi^* \right) \quad (159)$$

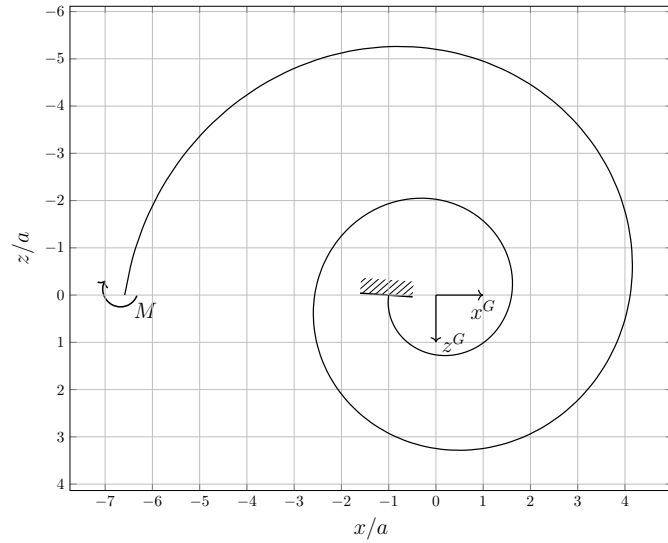


FIGURE 13 Logarithmic spiral: Geometric shape, support and loading, and the choice of global coordinate axes

where

$$c = \frac{b}{a\sqrt{1+b^2}} \quad (160)$$

and

$$\varphi^* = \arctan b \quad (161)$$

are auxiliary parameters, introduced only to simplify notation. Formulae (157)–(159) can be understood as a generalized form of the formulae that characterize a circular geometry. Indeed, by setting $a = R$ and $b \rightarrow 0$, we can reduce (157)–(159) to (5)–(7). Since $b \rightarrow 0$ leads to $c \rightarrow 0$, the expression on the right-hand side of (157) tends to a fraction $0/0$ but the limit, x/R , can be properly evaluated using L'Hospital's rule. Formulae (158)–(159) are then reduced simply by setting $a = R$, $c = 0$, $\varphi^* = 0$ and $\varphi_0(x)$ by x/R .

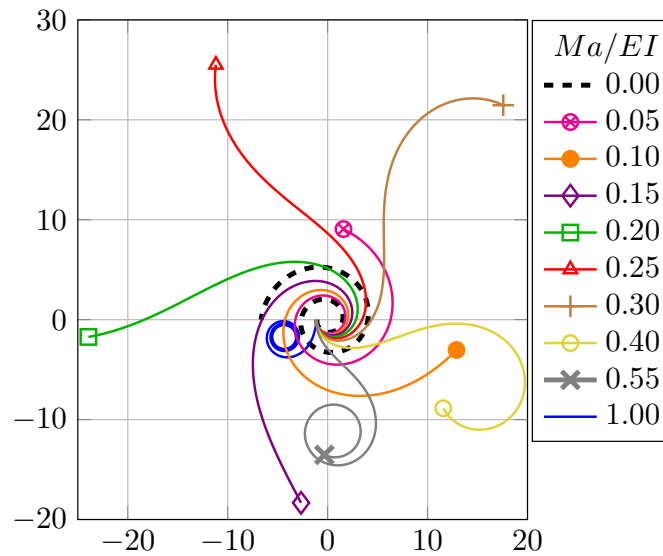


FIGURE 14 Initial undeformed shape of the spiral (black) and selected deformed shapes for applied moment increasing up to $M = EI/a$, plotted in the space of dimensionless coordinates normalized by a .

Similarly to Example 4.3, one side of the curved beam is clamped and the other is loaded by an increasing end moment unfolding the spiral, see Fig. 13. Parameter b that controls the shape of the spiral is in this example set to 0.15 and the polar angle θ varies from 0 to 4π , which means that the spiral has initially two full loops. The only other parameter that matters is the ratio $h_s/a = 1/30$, which leads to a dimensionless parameter $EAa^2/EI = 1080$.

Selected deformed shapes (and the initial undeformed shape in black) for a sequence of applied moments ranging from 0 to EI/a are shown in Fig. 14, and the final state, reached at $M = EI/a$, is reproduced in detail in Fig. 15. The spatial coordinates used in Figs. 13–15 have their origin at the pole of the spiral and are normalized by constant a . In the dimensionless coordinates, the clamped section is located at $(-1, 0)$.

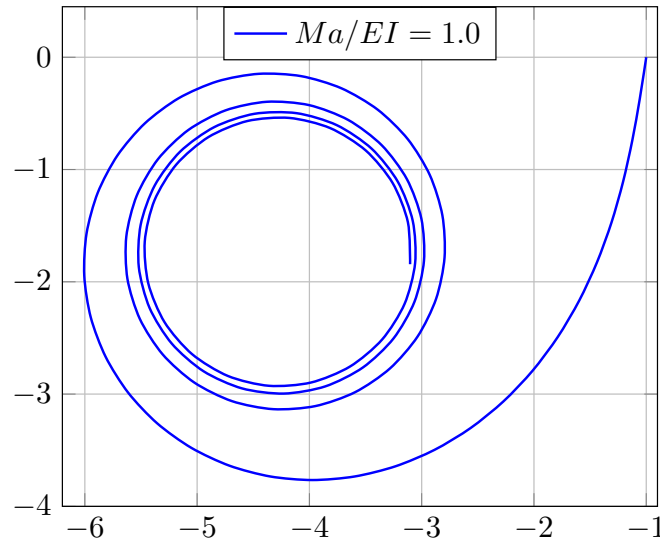


FIGURE 15 Deformed shape of the final configuration.

4.7 | A zig-zag beam (two-dimensional spring)

One advantage of the proposed formulation is that it can easily handle not only beams with a smooth curved centerline, but also beams with kinks, i.e., with discontinuities in the centerline slope. An illustrative example is the zig-zag beam depicted in the top part of Fig. 16a, which can be considered as a two-dimensional form of a spring. This beam consists of ten straight segments, with a right angle between neighboring segments. During the initial phase of loading by an increasing horizontal force P at the left support, the spring is compressed and its “macroscopic axis” remains straight. However, since the zig-zag centerline does not coincide with that fictitious axis, individual segments experience bending and, from the macroscopic point of view, the spring is relatively flexible in tension or compression. The overall deformed shape is plotted in the bottom part of Fig. 16a in black. The vertical displacement of the traced point marked by a special symbol remains very small and the horizontal displacement increases almost proportionally to the applied force; see the first steep part of the load-displacement diagrams in Fig. 16b. When a critical force is reached, the spring starts buckling and the vertical displacement increases dramatically (solid curve in Fig. 16b). The deformed shape evolves as indicated by images in green and blue in Fig. 16a until the ends of the spring meet (red image).

This highly nonlinear process has been simulated using one single element. The results are presented in Fig. 16b in terms of the dimensionless force PL^2/EI and dimensionless displacements u/L and w/L . The axial sectional stiffness was selected such that $EAL^2/EI = 1000$, which corresponds to a not too stocky beam, with individual physical segments deforming mainly by bending. The fact that the centerline consists of straight segments with kinks does not lead to any changes in the algorithm presented in Section 3.3.1. It is sufficient to make sure that each kink point is at the same time one of the points of the computational grid. In other words, each physical segment is divided into an integer number of computational segments. The simulation

results are presented here for 200 computational segments per regular full-length physical segments (100 computational segments in the first and last physical segment), i.e., with $NIS=1800$, but it has been checked that the load-displacement curves would remain visually almost the same even with $NIS=90$. It has also been verified that the same results are obtained if the zig-zag beam is divided into 10 straight elements.

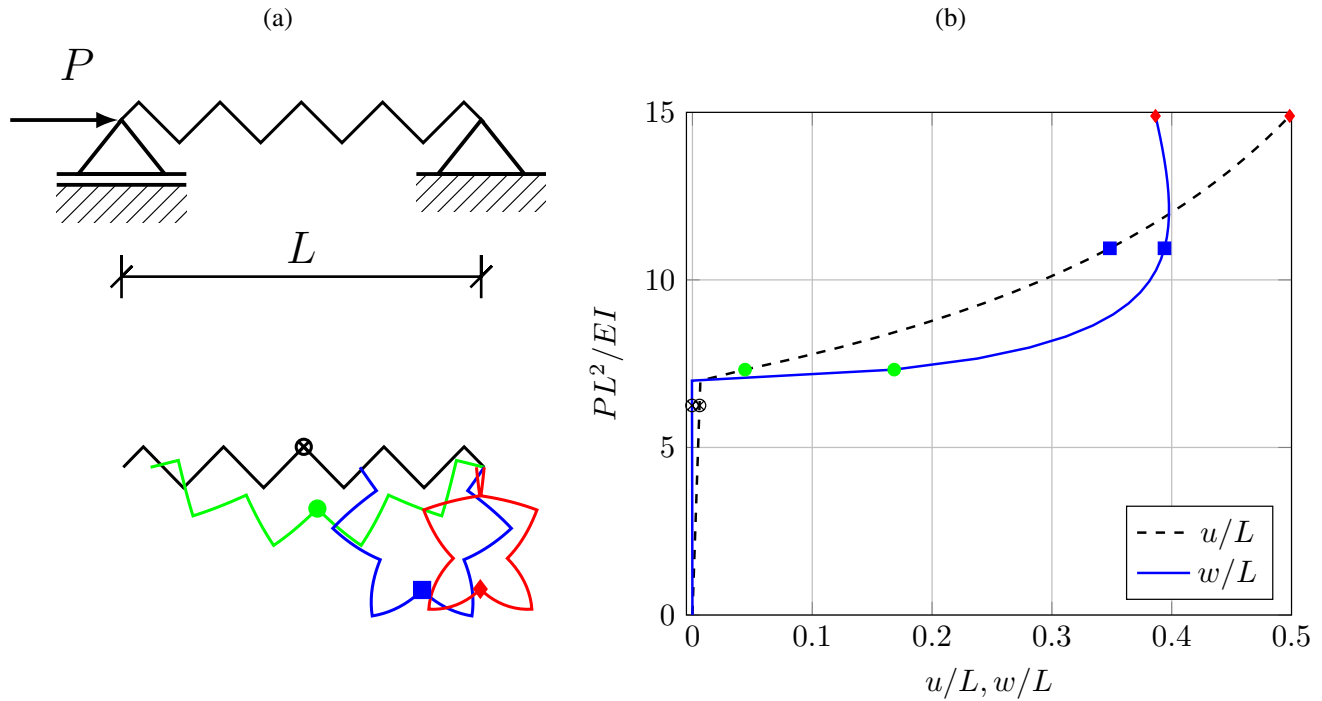


FIGURE 16 Zig-zag beam: (a) initial geometry and loading (top) and deformed shapes (bottom), (b) load-displacement diagrams for the horizontal and vertical displacements of the selected point at beam center

The critical force can be estimated based on analogy with a standard straight beam that has an equivalent stiffness. For the linearized model, one can easily evaluate the displacement caused by a unit force applied along the macroscopic axis and also the end rotations caused by two unit moments applied at the opposite ends with opposite orientations. This is then set equal to the displacement L/\overline{EA} and rotation L/\overline{EI} that would be produced on a standard beam with axial sectional stiffness \overline{EA} and flexural sectional stiffness \overline{EI} . For the present input data, the resulting equivalent stiffnesses are $\overline{EA} = 486\sqrt{2}EI/L^2$ and $\overline{EI} = EI/\sqrt{2}$. A simple estimate of the critical load is obtained using the standard Euler formula for a simply supported beam,

$$P_E = \frac{\overline{EI}\pi^2}{L^2} = \frac{EI\pi^2}{\sqrt{2}L^2} \approx 6.9789 \frac{EI}{L^2} \quad (162)$$

This would be exact for an axially incompressible beam. An improved estimate that takes into account the axial compressibility is constructed using formula (112) from our previous paper¹ (the more accurate version of the formula is used):

$$P_{cr} = \frac{\overline{EA}}{2} \left(1 - \sqrt{1 - \frac{4\overline{EI}\pi^2}{\overline{EA}L^2}} \right) = \frac{243\sqrt{2}EI}{L^2} \left(1 - \sqrt{1 - \frac{\pi^2}{243}} \right) \approx 7.0512 \frac{EI}{L^2} \quad (163)$$

The critical force evaluated by a highly accurate numerical simulation turns out to be $7.0514EI/L^2$.

The reason why the algorithm from Section 3.3.1 does not need to be modified is that the discontinuity in the initial slope, i.e., in function φ_0 , does not affect the evaluation of $\varphi_0(x_{i-1/2})$ in the algorithmic steps described by equations (74) and (78)–(79), provided that the midpoints of integration segments do not coincide with the kink points on the centerline. The initial curvature κ_0 is considered as zero and φ_0 is constant in each physical segment. For the present geometry, $\varphi_0 = 0$ in odd physical segments and $\varphi_0 = -\pi/2$ in even physical segments. Functions u_0 and w_0 are also easy to describe. The accuracy depends on the number

of computational segments per physical segments. The whole spring with a zig-zag centerline can be handled by one element and the number of global degrees of freedom remains low (equal to 2 if the loading process is controlled by applied horizontal displacement at the left support) and independent of the number of physical segments in the spring. Since the function that describes the distribution of bending moments is not smooth (for small changes of the initial geometry, it is piecewise linear), it would be very hard to approximate the resulting rotation function by a polynomial. Therefore, the approach of Saje²⁰, described in Section 2.5, would in this case require discretization into elements that correspond to individual physical segments, leading to many global degrees of freedom. Of course, the example is somewhat artificial, but it is not totally meaningless and illustrates the high flexibility of our approach.

5 | CONCLUDING REMARKS

As illustrated by the examples, the formulation developed in this paper can describe curved elastic beams under large displacements and rotations with high accuracy. In summary, the main idea is that the equilibrium equations are used in their integrated form (45)–(46), and they are combined with the geometrically exact kinematic relations (47)–(49) and sectional equations (52)–(53). The resulting set of three first-order ordinary differential equations is then numerically approximated by an explicit finite difference scheme and the boundary value problem is converted to an initial value problem using the shooting method. On the global (structural) level, the governing equations are assembled in the same way as for a standard two-noded beam element with six degrees of freedom. In this sense, it plays the same role as traditional finite elements in the context of structural analysis. The advantage is that accuracy of the numerical approximation can be conveniently increased by refining the integration scheme on the element level while the number of global degrees of freedom is kept constant.

The specific formulation presented in this paper is based on a number of simplifying assumptions, some of which could be generalized. From the kinematic point of view, the formulation has been developed for curved planar beams assuming the validity of the Navier-Bernoulli hypothesis. An extension to shear-flexible beams would be relatively straightforward. One would need to include the shear force among the internal forces and link it to the sectional shear distortion. This would not substantially affect the structure of the governing equations. A much more challenging task would be an extension to three dimensions, which would require a major change of the descriptor that characterizes the sectional rotation.

The initial shape of the curved beam that can be considered by the present formulation is virtually arbitrary. It is described by functions that relate the position of each centerline point and the inclination of the corresponding section to the arc-length coordinate. For some shapes, most notably for the circular shape, such functions are available in closed form. If this is not the case, a table of values of these functions can be precomputed numerically. Alternatively, for flat elements, one can use the projection onto a straight line as a replacement of the arc-length coordinate, with the slight drawback that the integration segments along the centerline then do not have a constant length.

Since accuracy can be efficiently improved by increasing the number of integration segments into which the element is divided, the size of the element does not need to be reduced and the number of global degrees of freedom can be kept low and independent of the refinement level. There is of course a limitation stemming from the presently used assumption that the loading is applied exclusively at joints that connect the elements while individual element are not loaded at their intermediate sections. However, this assumption has been introduced only for simplicity and it could easily be removed. In the integrated form of the equilibrium equations, the effect of loads applied directly on the element can be incorporated. This is conceptually easy and the extended implementation only requires a more refined specification and processing of the input data.

A very attractive feature of the present formulation is that it does not suffer from membrane locking. This is documented in examples in Sections 4.1–4.2. Convergence to the exact solution is found to be very regular, the results are meaningful even for relatively coarse discretizations, and no parasitic oscillations of internal forces are detected.

From the constitutive point of view, the presented simple version of the method is based on the assumption of linear elasticity. The expressions for internal forces (normal force and bending moment) as functions of the sectional deformation variables (axial stretch or strain and curvature) are then linear and easily invertible. Still, for a curved beam, it is interesting to note that the sectional equations are coupled, in contrast to the case of a straight beam. This phenomenon and its consequences are illustrated by an example in Section 4.3 and analyzed in detail in Appendix A. The difference as compared to the simplified uncoupled equations is negligible for very slender beams but it may play an important role if, for instance, a thick-walled cylinder is analyzed using a circular beam model.

The constitutive description can be generalized to nonlinear elasticity (as outlined in Appendix A.2) and even to inelastic behavior, e.g., to plasticity. Of course, the computational demands are then increased, because the inverted form of the relation between internal forces and deformation variables can hardly be described analytically and numerical evaluation, involving an iterative solution of a set of two nonlinear algebraic equations, needs to be adopted. It is fair to admit that the method would fail if this relation becomes non-invertible, e.g., due to softening in the moment-curvature diagram. Such cases would lead to localization phenomena and would need to be handled by adaptively introducing generalized inelastic hinges.

Certain theoretical aspects that are not necessary for proper understanding of the present approach but could be of general interest are discussed in detail in Appendix A. In particular, the appendix presents a rigorous analysis of the structure of sectional equations for curved beams. The present approach, with sectional equations consistently derived from a uniaxial hyperelastic stress-strain law, is compared to the reduced form of the equations used for description of shells by Simo and Fox¹⁹, which were derived from a potential postulated directly in terms of the deformation variables on the sectional level. It is shown that such a potential cannot have an arbitrary form and that, if it is derived consistently, the definition of the effective membrane stress resultant used by Simo and Fox¹⁹ needs to be modified.

ACKNOWLEDGMENTS

The authors are grateful for the support of the Czech Science Foundation (project No. 19-26143X). The authors would also like to thank A. Borković for providing data for the load-displacement curves of parabolic arches calculated by the IGA formulation¹⁴.

Conflict of interest

The authors declare no potential conflict of interests.

References

1. Jirásek M, La Malfa Ribolla E, Horák M. Efficient finite difference formulation of a geometrically nonlinear beam element. *International Journal for Numerical Methods in Engineering* 2021; 122(23): 7013-7053. doi: <https://doi.org/10.1002/nme.6820>
2. Noor A, Peters J. Mixed models and reduced/selective integration displacement models for nonlinear analysis of curved beams. *International Journal for Numerical Methods in Engineering* 1981; 17(4): 615-631. doi: 10.1002/nme.1620170409
3. Stolarski H, Belytschko T. Membrane locking and reduced integration for curved elements. *Journal of Applied Mechanics, Transactions ASME* 1982; 49(1): 172-176. doi: 10.1115/1.3161961
4. Stolarski H, Belytschko T. Shear and membrane locking in curved C^0 elements. *Computer Methods in Applied Mechanics and Engineering* 1983; 41(3): 279-296. doi: 10.1016/0045-7825(83)90010-5
5. Babu C, Prathap G. A linear thick curved beam element. *International Journal for Numerical Methods in Engineering* 1986; 23(7): 1313-1328. doi: 10.1002/nme.1620230709
6. Zhang C, Di S. New accurate two-noded shear-flexible curved beam elements. *Computational Mechanics* 2003; 30(2): 81-87. doi: 10.1007/s00466-002-0367-2
7. Ferradi MK, Cespedes X. A curved beam model with the asymptotic expansion method. *Engineering Structures* 2021; 241. doi: 10.1016/j.engstruct.2021.112494
8. Reissner E. On one-dimensional finite-strain beam theory: the plane problem. *Zeitschrift für angewandte Mathematik und Physik ZAMP* 1972; 23(5): 795-804.
9. Reissner E. On one-dimensional large-displacement finite-strain beam theory. *Studies in Applied Mathematics* 1973; 52(2): 87-95.

10. Simo JC. A finite strain beam formulation. The three-dimensional dynamic problem. I. *Computer Methods in Applied Mechanics and Engineering* 1985; 49(1): 55–70.
11. Simo JC, Vu-Quoc L. A three-dimensional finite-strain rod model. Part II: Computational aspects. *Computer Methods in Applied Mechanics and Engineering* 1986; 58(1): 79–116.
12. Simo JC, Vu-Quoc L. On the dynamics of flexible beams under large overall motions-the plane case: Part I. *Journal of Applied Mechanics, Transactions ASME* 1986; 53(4): 849-854. doi: 10.1115/1.3171870
13. Simo JC, Vu-Quoc L. On the dynamics of flexible beams under large overall motions-the plane case: Part II. *Journal of Applied Mechanics, Transactions ASME* 1986; 53(4): 855-863. doi: 10.1115/1.3171871
14. Borković A, Marussig B, Radenković G. Geometrically exact static isogeometric analysis of arbitrarily curved plane Bernoulli–Euler beam. *Thin-Walled Structures* 2022; 170: 108539.
15. Marino E, Kiendl J, De Lorenzis L. Isogeometric collocation for implicit dynamics of three-dimensional beams undergoing finite motions. *Computer Methods in Applied Mechanics and Engineering* 2019; 356: 548-570. doi: <https://doi.org/10.1016/j.cma.2019.07.013>
16. Ibrahimbegovic A. On the choice of finite rotation parameters. *Computer Methods in Applied Mechanics and Engineering* 1997; 149(1): 49-71. Containing papers presented at the Symposium on Advances in Computational Mechanicsdoi: [https://doi.org/10.1016/S0045-7825\(97\)00059-5](https://doi.org/10.1016/S0045-7825(97)00059-5)
17. Magisano D, Leonetti L, Madeo A, Garcea G. A large rotation finite element analysis of 3D beams by incremental rotation vector and exact strain measure with all the desirable features. *Computer Methods in Applied Mechanics and Engineering* 2020; 361: 112811. doi: <https://doi.org/10.1016/j.cma.2019.112811>
18. Bauer AM, Breitenberger M, Philipp B, Wüchner R, Bletzinger KU. Nonlinear isogeometric spatial Bernoulli beam. *Computer Methods in Applied Mechanics and Engineering* 2016; 303: 101–127. doi: 10.1016/j.cma.2015.12.027
19. Simo JC, Fox DD. On a stress resultant geometrically exact shell model. Part I: Formulation and optimal parametrization. *Computer Methods in Applied Mechanics and Engineering* 1989; 72(3): 267–304.
20. Saje M. Finite element formulation of finite planar deformation of curved elastic beams. *Computers and Structures* 1991; 39(3-4): 327–337. doi: 10.1016/0045-7949(91)90030-P
21. Patzák B, Bittnar Z. Design of object oriented finite element code. *Advances in Engineering Software* 2001; 32(10-11): 759–767.
22. Patzák B. OOFEM—an object-oriented simulation tool for advanced modeling of materials and structures. *Acta Polytechnica* 2012; 52(6).
23. Marguerre K. Zur Theorie der gekrümmten Platte grosser Formänderung. In: 1938 (pp. 93–101).
24. Bieber S, Oesterle B, Ramm E, Bischoff M. A variational method to avoid locking—independent of the discretization scheme. *International Journal for Numerical Methods in Engineering* 2018; 114(8): 801–827. doi: 10.1002/nme.5766
25. Ibrahimbegović A. On finite element implementation of geometrically nonlinear Reissner’s beam theory: three-dimensional curved beam elements. *Computer Methods in Applied Mechanics and Engineering* 1995; 122(1): 11 - 26. doi: [https://doi.org/10.1016/0045-7825\(95\)00724-F](https://doi.org/10.1016/0045-7825(95)00724-F)
26. Wood RD, Zienkiewicz O. Geometrically nonlinear finite element analysis of beams, frames, arches and axisymmetric shells. *Computers & Structures* 1977; 7(6): 725–735.
27. DaDeppo D, Schmidt R. Instability of clamped-hinged circular arches subjected to a point load. *Journal of Applied Mechanics, Transactions ASME* 1975; 42(4): 894–896.
28. DaDeppo D, Schmidt R. Large deflections and stability of hingeless circular arches under interacting loads. *Journal of Applied Mechanics, Transactions ASME* 1974; 41(4): 989-994.

29. DaDeppo D, Schmidt R. Nonlinear analysis of buckling and postbuckling behavior of circular arches. *Zeitschrift für angewandte Mathematik und Physik ZAMP* 1969; 20(6): 847-857.
30. Simo J, Wriggers P, Schweizerhof K, Taylor R. Finite deformation post-buckling analysis involving inelasticity and contact constraints. *International journal for numerical methods in engineering* 1986; 23(5): 779–800.
31. Sabir A, Lock A. Large deflexion, geometrically non-linear finite element analysis of circular arches. *International Journal of Mechanical Sciences* 1973; 15(1): 37–47.



APPENDIX

A STRUCTURE OF SECTIONAL EQUATIONS FOR CURVED BEAMS

A.1 Brief summary of the origin of sectional equations adopted in this paper

In general, sectional equations link the internal forces to variables that characterize the deformation of an infinitesimal beam segment. In our case (planar Euler-Bernoulli beam), the relevant internal forces are the normal force, N , and the bending moment, M , which have a clear physical meaning. On the other hand, the deformation variables can be selected in different ways, but they should characterize the processes of axial stretching and bending. Perhaps the most natural choice is to consider the centerline stretch λ , defined in (17), and the curvature κ , defined as the derivative of the sectional rotation φ with respect to the initial centerline length, i.e., as $\kappa = \varphi'$. Using these variables, one can conveniently describe the distribution of normal stretch λ across the section by formula (20), which also contains the initial curvature, κ_0 .

It is worth noting that formula (20) directly follows from the basic kinematic assumptions that are behind equations (1)–(2) and (13)–(14). The stretch, λ , is understood here as the ratio of the current and initial lengths of an infinitesimal fiber parallel to the centerline. Since shear deformation is neglected and individual material fibers parallel to the centerline are expected to be in a state of uniaxial stress, it is perfectly justified to assume that the density of strain energy (per unit initial volume), \mathcal{E}_{int} , is a function of the stretch. The resulting expression (24) for the strain energy variation shows that, at the sectional level, the normal force is work-conjugate with the centerline stretch, and the bending moment is work-conjugate with the curvature (understood in the present sense, i.e., as the derivative of sectional rotation with respect to the initial centerline length). The stress σ that appears in the integral definitions of internal forces as stress resultants, eqs. (25)–(26), is understood as the quantity that is work-conjugate with the stretch at the fiber level.

In the special case of a quadratic expression for strain energy density (in terms of the Biot strain $\epsilon = \lambda - 1$), the corresponding material law that links the stress to the stretch (or to the Biot strain) is linear, which then leads to a linear form of the sectional equations (34)–(35). In contrast to what would be obtained for an initially straight beam, these equations are coupled, in the sense that the normal force depends not only on the axial strain but also on the change of curvature, and the bending moment depends not only on the change of curvature but also on the axial strain.

A.2 Extension to other hyperelastic material laws

For general hyperelasticity, the strain energy density does not need to be quadratic in terms of Biot strain. The description of stretch distribution across the section by formula (20) as well as the definitions of internal forces as stress resultants given by (25)–(26) remain valid, independently of the constitutive model. One only needs to adjust the material law that links the stress to the stretch, and then derive the corresponding sectional equations. Often, the integrals in (25)–(26) would have to be evaluated numerically.

A.2.1 St. Venant-Kirchhoff model

It is instructive to look at one of the special cases that permit analytical evaluation. Let us consider the St. Venant-Kirchhoff model, which postulates a linear relationship between the Green-Lagrange strain and its work-conjugate stress, which is the

second Piola-Kirchhoff stress. This model is obtained by defining the strain energy density as a quadratic function of the Green-Lagrange strain $\varepsilon_{GL} = (\lambda^2 - 1)/2$. From

$$\mathcal{E}_{int} = \frac{1}{2} E \varepsilon_{GL}^2 = \frac{E}{8} (\lambda^2 - 1)^2 \quad (A1)$$

we get

$$\sigma = \frac{d\mathcal{E}_{int}}{d\lambda} = \frac{E}{2} (\lambda^2 - 1) \lambda = \frac{E}{2} (\lambda^3 - \lambda) \quad (A2)$$

in which σ is the first Piola-Kirchhoff stress (note that the second Piola-Kirchhoff stress would be obtained by differentiating \mathcal{E}_{int} with respect to ε_{GL} and would be given by $E\varepsilon_{GL}$). The internal forces are then evaluated as

$$\begin{aligned} N &= \int_A \sigma dA = \frac{E}{2} \int_A \left(\frac{(\lambda_s + z\kappa)^3}{(1 + z\kappa_0)^3} - \frac{\lambda_s + z\kappa}{1 + z\kappa_0} \right) dA = \\ &= \frac{EA_3}{2} (2\varepsilon_s + 3\varepsilon_s^2 + \varepsilon_s^3) + \frac{ES_3}{2} (\kappa_0 \varepsilon_s (4 + 3\varepsilon_s) + (2 + 6\varepsilon_s + 3\varepsilon_s^2) \Delta\kappa) + \\ &\quad + \frac{EI_3}{2} ((2\kappa_0^2 + 6\kappa_0 \Delta\kappa + 3\Delta\kappa^2) \varepsilon_s + 4\kappa_0 \Delta\kappa + 3\Delta\kappa^2) + \frac{EJ_3}{2} (2\kappa_0^2 \Delta\kappa + 3\kappa_0 \Delta\kappa^2 + \Delta\kappa^3) \end{aligned} \quad (A3)$$

$$\begin{aligned} M &= \int_A z\sigma dA = \frac{E}{2} \int_A \left(\frac{z(\lambda_s + z\kappa)^3}{(1 + z\kappa_0)^3} - \frac{z\lambda_s + z^2\kappa}{1 + z\kappa_0} \right) dA = \\ &= \frac{ES_3}{2} (2\varepsilon_s + 3\varepsilon_s^2 + \varepsilon_s^3) + \frac{EI_3}{2} (\kappa_0 \varepsilon_s (4 + 3\varepsilon_s) + (2 + 6\varepsilon_s + 3\varepsilon_s^2) \Delta\kappa) + \\ &\quad + \frac{EJ_3}{2} ((2\kappa_0^2 + 6\kappa_0 \Delta\kappa + 3\Delta\kappa^2) \varepsilon_s + 4\kappa_0 \Delta\kappa + 3\Delta\kappa^2) + \frac{EK_3}{2} (2\kappa_0^2 \Delta\kappa + 3\kappa_0 \Delta\kappa^2 + \Delta\kappa^3) \end{aligned} \quad (A4)$$

in which

$$A_3 = \int_A \frac{1}{(1 + z\kappa_0)^3} dA \quad (A5)$$

$$S_3 = \int_A \frac{z}{(1 + z\kappa_0)^3} dA \quad (A6)$$

$$I_3 = \int_A \frac{z^2}{(1 + z\kappa_0)^3} dA \quad (A7)$$

$$J_3 = \int_A \frac{z^3}{(1 + z\kappa_0)^3} dA \quad (A8)$$

$$K_3 = \int_A \frac{z^4}{(1 + z\kappa_0)^3} dA \quad (A9)$$

are modified sectional characteristics. These five quantities are linked by the relations $A_3 + 3\kappa_0 S_3 + 3\kappa_0^2 I_3 + \kappa_0^3 J_3 = A$ and $S_3 + 3\kappa_0 I_3 + 3\kappa_0^2 J_3 + \kappa_0^3 K_3 = 0$, and so only three of them are independent. For a straight beam, they reduce to $A_3 = A$, $S_3 = 0$, $I_3 = I$, $J_3 = \int_A z^3 dA$ and $K_3 = \int_A z^4 dA$.

The internal forces are now nonlinear functions of the (Biot) axial strain, ε_s , and the curvature change, $\Delta\kappa$. Inversion of the nonlinear sectional equations (A3)–(A4) in closed form is not possible, but the deformation variables that correspond to a given combination of internal forces N and M can, at least within a certain range, be evaluated numerically by the Newton-Raphson method.

The main reason why we present the explicit form of these more complicated sectional equations (A3)–(A4) is that they can now be compared with the linear sectional equations (34)–(35). The common feature is that, in both cases, the equations are coupled. For instance, the normal force depends not only on the axial strain but also on the change of curvature. For the linear sectional equations, it is possible to find a transformed quantity, $N + \kappa_0 M$, which is linked exclusively to the centerline strain and independent of the curvature change. However, this special property is closely related to the choice of the constitutive model and cannot be considered as general. To see that, it is sufficient to realize that

$$N + \kappa_0 M = \int_A \sigma dA + \kappa_0 \int_A z\sigma dA = \int_A (1 + z\kappa_0) \sigma dA \quad (A10)$$

If the stress-strain law (28) is used, the resulting stress distribution is given by (29), with $1 + z\kappa_0$ in the denominator, and expression (A10) yields a very simple result:

$$\int_A (1 + z\kappa_0) \sigma \, dA = \int_A (1 + z\kappa_0) E \frac{\varepsilon_s + z\Delta\kappa}{1 + z\kappa_0} \, dA = E \int_A (\varepsilon_s + z\Delta\kappa) \, dA = EA\varepsilon_s \quad (\text{A11})$$

In contrast to that, for the stress-strain law given by (A2), the integrand does not simplify that much, and the result still depends on $\Delta\kappa$:

$$\int_A (1 + z\kappa_0) \sigma \, dA = \int_A (1 + z\kappa_0) \frac{E}{2} \left(\frac{(\lambda_s + z\kappa)^3}{(1 + z\kappa_0)^3} - \frac{\lambda_s + z\kappa}{1 + z\kappa_0} \right) \, dA = \frac{E}{2} \int_A \left(\frac{(\lambda_s + z\kappa)^3}{(1 + z\kappa_0)^2} - \lambda_s - z\kappa \right) \, dA = \quad (\text{A12})$$

$$= \frac{E}{2} \int_A \frac{(\lambda_s + z(\kappa_0 + \Delta\kappa))^3}{(1 + z\kappa_0)^2} \, dA - \frac{EA}{2} \lambda_s \quad (\text{A13})$$

One can also verify that if the expression on the right-hand side of (A4) is multiplied by κ_0 and added to the expression on the right-hand side of (A3), terms with $\Delta\kappa$ do not cancel out. This fact will be used later on in the discussion of the differences between the present modeling approach and the framework used by Simo and Fox¹⁹ for shells.

It is interesting to note that if all nonlinear terms in equations (A3)–(A4) are neglected, the equations reduce to

$$N = (EA_3 + 2\kappa_0 ES_3 + \kappa_0^2 EI_3) \varepsilon_s + (ES_3 + 2\kappa_0 EI_3 + \kappa_0^2 EJ_3) \Delta\kappa \quad (\text{A14})$$

$$M = (ES_3 + 2\kappa_0 EI_3 + \kappa_0^2 EJ_3) \varepsilon_s + (EI_3 + 2\kappa_0 EJ_3 + \kappa_0^2 EK_3) \Delta\kappa \quad (\text{A15})$$

This form of sectional equations linearized around the initial state is equivalent to the linear sectional equations (34)–(35). To see that, it is sufficient to realize that $A_3 + 2\kappa_0 S_3 + \kappa_0^2 I_3 = A_{\kappa_0}$, $S_3 + 2\kappa_0 I_3 + \kappa_0^2 J_3 = S_{\kappa_0}$ and $I_3 + 2\kappa_0 J_3 + \kappa_0^2 K_3 = I_{\kappa_0}$, as follows from definitions (A5)–(A9) and (36)–(38). In the next subsection, we will show that the same linearized form is obtained for sectional equations derived from any uniaxial hyperelastic stress-strain law, i.e., not only from the presently considered St. Venant-Kirchhoff law.

A.2.2 General hyperelasticity

A certain drawback of uniaxial stress-strain laws that follow from the assumed quadratic expression for strain energy density in terms of Biot strain or Green-Lagrange strain is that they fail to describe the extreme compression limit, $\lambda \rightarrow 0^+$. The energy density remains finite and the stress as well. For the St. Venant-Kirchhoff model, the first Piola-Kirchhoff stress even tends to zero in this limit. This deficiency is not so critical for applications to slender beams, which usually buckle in compression and large compressive strains are not really attained. If needed, a more realistic behavior in extreme compression can be obtained if the strain energy density is taken as quadratic in terms of the logarithmic strain, i.e., if we set

$$\mathcal{E}_{int} = \frac{1}{2} E (\ln \lambda)^2 \quad (\text{A16})$$

The first Piola-Kirchhoff stress is then given by

$$\sigma = \frac{d\mathcal{E}_{int}}{d\lambda} = E \frac{\ln \lambda}{\lambda} \quad (\text{A17})$$

This tends to minus infinity as $\lambda \rightarrow 0^+$, i.e., in extreme compression. On the other hand, in tension the first Piola-Kirchhoff stress attains its maximum at $\lambda = e$ and afterwards decreases to zero.

Of course, one could further improve the material description by constructing a more appropriate (and presumably more complicated) expression for strain energy density, but it is also possible to postulate directly the function Σ that links the first Piola-Kirchhoff stress to the stretch. For such a general elastic material law

$$\sigma = \Sigma(\lambda) \quad (\text{A18})$$

the corresponding sectional equations read

$$N = \int_A \Sigma \left(\frac{\lambda_s + z\kappa}{1 + z\kappa_0} \right) \, dx = \int_A \Sigma \left(1 + \frac{\varepsilon_s + z\Delta\kappa}{1 + z\kappa_0} \right) \, dx \quad (\text{A19})$$

$$M = \int_A z \Sigma \left(\frac{\lambda_s + z\kappa}{1 + z\kappa_0} \right) \, dx = \int_A z \Sigma \left(1 + \frac{\varepsilon_s + z\Delta\kappa}{1 + z\kappa_0} \right) \, dx \quad (\text{A20})$$

Differentiating the internal forces with respect to the deformation variables ε_s and $\Delta\kappa$, we obtain the tangent sectional stiffnesses

$$\frac{\partial N}{\partial \varepsilon_s} = \int_A \frac{1}{1 + z\kappa_0} \Sigma_{,\lambda} \left(1 + \frac{\varepsilon_s + z \Delta\kappa}{1 + z\kappa_0} \right) dx \quad \frac{\partial N}{\partial \Delta\kappa} = \int_A \frac{z}{1 + z\kappa_0} \Sigma_{,\lambda} \left(1 + \frac{\varepsilon_s + z \Delta\kappa}{1 + z\kappa_0} \right) dx \quad (\text{A21})$$

$$\frac{\partial M}{\partial \varepsilon_s} = \int_A \frac{z}{1 + z\kappa_0} \Sigma_{,\lambda} \left(1 + \frac{\varepsilon_s + z \Delta\kappa}{1 + z\kappa_0} \right) dx \quad \frac{\partial M}{\partial \Delta\kappa} = \int_A \frac{z^2}{1 + z\kappa_0} \Sigma_{,\lambda} \left(1 + \frac{\varepsilon_s + z \Delta\kappa}{1 + z\kappa_0} \right) dx \quad (\text{A22})$$

Here, $\Sigma_{,\lambda} \equiv d\Sigma/d\lambda$ is the tangent material modulus. Its value at $\lambda = 1$ is the standard elastic modulus, E .

The main point to be made here is that no matter which specific form of the material law is used, the coupling effect is always present, already in the small-strain range. Indeed, the cross-coupling stiffness, $\partial N/\partial \Delta\kappa \equiv \partial M/\partial \varepsilon_s$, vanishes only exceptionally, e.g., when $\kappa_0 = 0$ and $\Sigma_{,\lambda}$ is constant, which corresponds to a straight beam and linear material law (28). In the initial undeformed state, we have $\varepsilon_s = 0$ and $\Delta\kappa = 0$, and the cross-coupling stiffness is

$$\frac{\partial N(0,0)}{\partial \Delta\kappa} = \frac{\partial M(0,0)}{\partial \varepsilon_s} = \int_A \frac{z}{1 + z\kappa_0} \Sigma_{,\lambda}(1) dx = \int_A \frac{Ez}{1 + z\kappa_0} dx = ES_{\kappa_0} \quad (\text{A23})$$

In a similar fashion, one gets $\partial N(0,0)/\partial \varepsilon_s = EA_{\kappa_0}$ and $\partial M(0,0)/\partial \Delta\kappa = EI_{\kappa_0}$. This means that even if the material law is nonlinear, the sectional equations linearized around the initial state always have the form (34)–(35) and thus are coupled, provided that the beam is curved.

Material nonlinearity cannot eliminate the coupling, and it can even introduce coupling for straight beams. For $\kappa_0 = 0$ (but a general deformation state), the cross-coupling sectional stiffness reduces to

$$\frac{\partial N(\varepsilon_s, \Delta\kappa)}{\partial \Delta\kappa} = \frac{\partial M(\varepsilon_s, \Delta\kappa)}{\partial \varepsilon_s} = \int_A z \Sigma_{,\lambda} (1 + \varepsilon_s + z \Delta\kappa) dx \quad (\text{A24})$$

This vanishes if the tangent modulus $\Sigma_{,\lambda} = \text{const.}$, but not in general. For instance, for the St. Venant-Kirchhoff model we have $\Sigma_{,\lambda}(\lambda) = E(3\lambda^2 - 1)/2$, and substitution into (A24) leads to

$$\int_A z \Sigma_{,\lambda} (1 + \varepsilon_s + z \Delta\kappa) dx = \frac{E}{2} \int_A z [3(1 + \varepsilon_s + z \Delta\kappa)^2 - 1] dA = \frac{E}{2} 3 \cdot 2 \cdot (1 + \varepsilon_s) \Delta\kappa \int_A z^2 dA = 3EI(1 + \varepsilon_s) \Delta\kappa \quad (\text{A25})$$

Here, the coupling effect vanishes as long as $\Delta\kappa = 0$, i.e., the beam remains straight. However, as the beam gets curved, the coupling effect gradually builds up.

A.3 Comparison with the framework used by Simo and Fox for shells

Simo and Fox¹⁹ proposed a framework for geometrically exact modeling of shells based on systematic tensorial description of basic quantities and governing equations. Among other developments, they introduced the concept of the *effective stress resultants*, which were obtained from the specific normal and shear forces by adding a certain linear combination of specific moments. The main objective was to construct internal forces that can be linked by sectional equations exclusively to the in-plane deformation variables, with the effect of bending eliminated. It is interesting to check how the Simo-Fox approach would reduce to the case of a two-dimensional Euler-Bernoulli beam studied here, and whether the effective membrane stress resultant corresponds to our $N + \kappa_0 M$, which was found to be dependent exclusively on the axial strain in the special case of linear sectional equations (34)–(35).

Simo and Fox¹⁹ worked with a general shape of the shell midsurface and described it using curvilinear coordinates and the corresponding surface convected frame, plus an additional director orthogonal frame. For comparison with the two-dimensional curved beam, it is sufficient to consider a cylindrical surface. Moreover, we assume that the section remains perpendicular to the deformed centerline, and so the director vector of the corresponding shell remains perpendicular to the deformed midsurface. The first curvilinear coordinate can be selected as our x , measured as the distance along the initial centerline, and the second one as the out-of-plane coordinate y . The surface convected frame is then orthogonal, initially even orthonormal; the first base vector stretches with the centerline and its norm is λ_s , the second remains a unit out-of-plane vector, and the third coincides with the unit director vector perpendicular to the midsurface.

Considering the curved beam (with a rectangular cross section) as a cylindrical shell strip of width b_s and using the special choice of curvilinear coordinates described above, we can reduce the expression for stress power presented in eq. (5.1) in Simo

and Fox¹⁹ to

$$\mathcal{W} = \int_0^L b_s (n^{11} \lambda_s \dot{\lambda}_s + \tilde{m}^{11} \lambda_s \dot{\kappa}) \lambda_s dx \quad (\text{A26})$$

where

$$n^{11} = \frac{N}{b_s \lambda_s^2} \quad (\text{A27})$$

$$\tilde{m}^{11} = \frac{M}{b_s \lambda_s^2} \quad (\text{A28})$$

are stress resultant components used by Simo and Fox¹⁹, evaluated from their equations (4.7), (4.11) and (4.22). Fractions N/b_s and M/b_s are identified as the specific normal force and specific bending moment, and the additional scaling by $1/\lambda_s^2$ is related to the fact that the first base vector is not normalized and its norm is λ_s . Substituting (A27)–(A28) into (A26), we can rewrite the stress power expression as

$$\mathcal{W} = \int_0^L b_s \left(\frac{N}{b_s \lambda_s^2} \lambda_s \dot{\lambda}_s + \frac{M}{b_s \lambda_s^2} \lambda_s \dot{\kappa} \right) \lambda_s dx = \int_0^L (N \dot{\lambda}_s + M \dot{\kappa}) dx \quad (\text{A29})$$

This is consistent with our previously derived equation (24), which expressed virtual work instead of stress power, and so the rates were replaced by virtual changes.

In the present paper, we have decided to define one of the deformation variables as $\kappa = \varphi'$, because this quantity is work-conjugate with the bending moment, as seen in (24). We refer to this variable as the “curvature”, even though it is equal to the reciprocal value of the radius of curvature only in the initial state, where $\kappa_0 = \varphi'_0 = 1/R_0$. In the deformed state, if the centerline segment is on a circle of radius R , has length $\lambda_s dx$ and the difference in rotation of the right and left end is $d\varphi$, elementary geometry considerations lead to the relation $R d\varphi = \lambda_s dx$, from which $R\varphi' = \lambda_s$. The true curvature is thus given by $k = 1/R = \varphi'/\lambda_s$. However, Simo and Fox¹⁹ used yet another measure of curvature, defined as

$$\kappa_{11} = \lambda_s \varphi' = \lambda_s \kappa \quad (\text{A30})$$

combined with a measure of membrane strain, defined as

$$\varepsilon_{11} = (\lambda_s^2 - 1)/2 \quad (\text{A31})$$

which is easily recognized as the Green-Lagrange strain. The rates of the deformation variables ε_{11} and κ_{11} are

$$\dot{\varepsilon}_{11} = \lambda_s \dot{\lambda}_s \quad (\text{A32})$$

$$\dot{\kappa}_{11} = \dot{\lambda}_s \kappa + \lambda_s \dot{\kappa} \quad (\text{A33})$$

and so the expression in parentheses inside the integral in (A26) can be transformed as follows:

$$n^{11} \lambda_s \dot{\lambda}_s + \tilde{m}^{11} \lambda_s \dot{\kappa} = n^{11} \dot{\varepsilon}_{11} + \tilde{m}^{11} (\dot{\kappa}_{11} - \kappa \dot{\lambda}_s) = n^{11} \dot{\varepsilon}_{11} + \tilde{m}^{11} (\dot{\kappa}_{11} - \dot{\varepsilon}_{11} \kappa / \lambda_s) = (n^{11} - \tilde{m}^{11} \kappa / \lambda_s) \dot{\varepsilon}_{11} + \tilde{m}^{11} \dot{\kappa}_{11} \quad (\text{A34})$$

Consequently, if we define the effective membrane stress resultant

$$\tilde{n}^{11} = n^{11} - \frac{\kappa}{\lambda_s} \tilde{m}^{11} \quad (\text{A35})$$

then the stress power can be expressed as

$$\mathcal{W} = \int_0^L b_s (\tilde{n}^{11} \dot{\varepsilon}_{11} + \tilde{m}^{11} \dot{\kappa}_{11}) \lambda_s dx \quad (\text{A36})$$

This means that quantities \tilde{n}^{11} and \tilde{m}^{11} are work-conjugate with deformation measures ε_{11} and κ_{11} . In fact, since the curvature does not vanish in the initial state, it is preferable to use the curvature increment $\Delta\kappa_{11} = \kappa_{11} - \kappa_{0,11}$ as the deformation variable (this quantity was denoted as ρ_{11} in Simo and Fox¹⁹, but we prefer $\Delta\kappa_{11}$, to avoid confusion with the density). Of course, by $\kappa_{0,11}$ we mean the value of κ_{11} in the initial state. Note that the factor κ/λ_s in (A35) represents the true curvature, k .

The constitutive description used by Simo and Fox¹⁹ was based on the assumption that there exists a stored energy function ψ that depends on the deformation variables, in our case only on ε_{11} and $\Delta\kappa_{11}$, and represents the strain energy per unit mass.

Since the deformation variables already characterize the strain state in the whole elementary segment, the strain energy of the shell would be evaluated by integrating over the midsurface, and for the 2D beam this reduces to integration over the centerline:

$$E_{int} = \int_0^L b_s h_s \rho_0 \psi \, dx \quad (A37)$$

The product $b_s h_s$ would in general correspond to the sectional area, but since we consider a beam model that represents a strip of a cylindrical shell, we insert right away the expression valid for a rectangular section. Symbol ρ_0 represents the initial mass density (per unit volume), and so the product $b_s h_s \rho_0$ is the mass per unit length of the centerline. Differentiation of (A37) with respect to time leads to the rate of the beam strain energy

$$\dot{E}_{int} = \int_0^L b_s h_s \rho_0 \left(\frac{\partial \psi}{\partial \epsilon_{11}} \dot{\epsilon}_{11} + \frac{\partial \psi}{\partial \Delta \kappa_{11}} \Delta \dot{\kappa}_{11} \right) dx \quad (A38)$$

and when this is compared with (A36), the constitutive equations are obtained in the form

$$\tilde{n}^{11} = \frac{h_s \rho_0}{\lambda_s} \frac{\partial \psi}{\partial \epsilon_{11}} \quad (A39)$$

$$\tilde{m}^{11} = \frac{h_s \rho_0}{\lambda_s} \frac{\partial \psi}{\partial \Delta \kappa_{11}} \quad (A40)$$

In eq. (5.18) in Simo and Fox¹⁹, these relations were written as

$$\tilde{n}^{11} = \bar{\rho} \frac{\partial \psi}{\partial \epsilon_{11}} \quad (A41)$$

$$\tilde{m}^{11} = \bar{\rho} \frac{\partial \psi}{\partial \Delta \kappa_{11}} \quad (A42)$$

where $\bar{\rho}$ is the mass density per unit surface area in the deformed state, which can be for a beam segment evaluated as

$$\bar{\rho} = \frac{\int_A \rho_0 (1 + z\kappa_0) \, dA \, dx}{b_s \lambda_s \, dx} = \frac{\rho_0 A \, dx}{b_s \lambda_s \, dx} = \frac{h_s \rho_0}{\lambda_s} \quad (A43)$$

This confirms that equations (A39)–(A40) and (A41)–(A42) are indeed equivalent.

An important difference between our approach and the framework used by Simo and Fox¹⁹ is that we start from constitutive equations at the material point level and construct the sectional equations by incorporating the kinematic assumptions that link strain to the sectional deformation variables, while Simo and Fox¹⁹ start on the sectional level and postulate the expression for stored energy density ψ directly in terms of the sectional deformation variables. The resulting sectional equations are equivalent only if the expression for ψ is consistently derived instead of arbitrarily postulated. Indeed, if we consider the strain energy density (per unit volume) as a given function \mathcal{E}_{int} of the stretch and combine this with the kinematic assumptions that lead to the distribution of stretch described by (20), substitution of (20) into (21) gives

$$E_{int} = \int_0^L \int_A (1 + z\kappa_0) \mathcal{E}_{int} \left(\frac{\lambda_s + z\kappa}{1 + z\kappa_0} \right) \, dA \, dx \quad (A44)$$

This is equivalent to (A37), provided that function ψ is defined as

$$\psi = \frac{1}{b_s h_s \rho_0} \int_A (1 + z\kappa_0) \mathcal{E}_{int} \left(\frac{\lambda_s + z\kappa}{1 + z\kappa_0} \right) \, dA = \frac{1}{b_s h_s} \int_A (1 + z\kappa_0) \psi_0 \left(\frac{\lambda_s + z\kappa}{1 + z\kappa_0} \right) \, dA \quad (A45)$$

in which $\psi_0 = \mathcal{E}_{int} / \rho_0$ is introduced only for convenience and represents the specific strain energy (i.e., energy per unit mass) of our original material model. The expression on the right-hand side of (A45) can be interpreted as averaging of the specific strain energy over the section, however, instead of uniform averaging, a certain weight function dependent on the initial curvature is used. Effectively, we average over the volume of the curved elementary segment.

In (A45), function ψ is presented as dependent on deformation variables λ_s and κ , but it is no problem to transform the expression into a function of any other two suitable chosen sectional deformation variables, such as our ϵ_s and $\Delta \kappa$, or ϵ_{11} and $\Delta \kappa_{11}$ used by Simo and Fox¹⁹. For instance, if we adopt the model based on quadratic energy density in terms of Biot strain,

function $\psi_0(\lambda)$ is given by $(E/2\rho_0)(\lambda - 1)^2$ and formula (A45) yields

$$\psi = \frac{1}{b_s h_s} \int_A (1+z\kappa_0) \frac{E}{2\rho_0} \left(\frac{\lambda_s + z\kappa}{1+z\kappa_0} - 1 \right)^2 dA = \frac{E}{2\rho_0 b_s h_s} \int_A (1+z\kappa_0) \left(\frac{\varepsilon_s + z\Delta\kappa}{1+z\kappa_0} \right)^2 dA = \frac{E}{2\rho_0 b_s h_s} (A_{\kappa_0} \varepsilon_s^2 + 2S_{\kappa_0} \varepsilon_s \Delta\kappa + I_{\kappa_0} \Delta\kappa^2) \quad (\text{A46})$$

Based on (A30)–(A31), the deformation variables used by Simo and Fox¹⁹ are

$$\varepsilon_{11} = \frac{1}{2}(\lambda_s^2 - 1) = \frac{1}{2}(\varepsilon_s^2 + 2\varepsilon_s) \quad (\text{A47})$$

$$\Delta\kappa_{11} = \lambda_s \kappa - \kappa_0 = \Delta\kappa + (\kappa_0 + \Delta\kappa)\varepsilon_s \quad (\text{A48})$$

and by inversion we obtain

$$\varepsilon_s = \sqrt{1 + 2\varepsilon_{11}} - 1 \quad (\text{A49})$$

$$\Delta\kappa = \frac{\Delta\kappa_{11} + \kappa_0 (1 - \sqrt{1 + 2\varepsilon_{11}})}{\sqrt{1 + 2\varepsilon_{11}}} \quad (\text{A50})$$

Substitution of these expressions into (A46) leads, after omission of constant terms, to

$$\begin{aligned} \psi = & \frac{E}{\rho_0 b_s h_s} \left(A_{\kappa_0} (\varepsilon_{11} - \sqrt{1 + 2\varepsilon_{11}}) + S_{\kappa_0} \left(\Delta\kappa_{11} - \frac{2\kappa_0(1 + \varepsilon_{11}) + \Delta\kappa_{11}}{\sqrt{1 + 2\varepsilon_{11}}} \right) + \right. \\ & \left. + I_{\kappa_0} \frac{(\kappa_0 + \Delta\kappa_{11})^2/2 - \kappa_0(\kappa_0 + \Delta\kappa_{11})\sqrt{1 + 2\varepsilon_{11}}}{1 + 2\varepsilon_{11}} \right) \end{aligned} \quad (\text{A51})$$

This function of ε_{11} and $\Delta\kappa_{11}$ can now be used in (A41)–(A42), where $\bar{\rho}$ needs to be replaced by

$$\bar{\rho} = \frac{h_s \rho_0}{\lambda_s} = \frac{h_s \rho_0}{\sqrt{1 + 2\varepsilon_{11}}} \quad (\text{A52})$$

The resulting expression for the effective membrane stress resultant is

$$\tilde{n}^{11} = \frac{E}{b_s} \left(A_{\kappa_0} \frac{\sqrt{1 + 2\varepsilon_{11}} - 1}{1 + 2\varepsilon_{11}} + S_{\kappa_0} \left(\frac{2\kappa_0(1 + \varepsilon_{11}) + \Delta\kappa_{11}}{(1 + 2\varepsilon_{11})^2} - \frac{2\kappa_0}{1 + 2\varepsilon_{11}} \right) + I_{\kappa_0} \left(\frac{\kappa_0(\kappa_0 + \Delta\kappa_{11})}{(1 + 2\varepsilon_{11})^2} - \frac{(\kappa_0 + \Delta\kappa_{11})^2}{(1 + 2\varepsilon_{11})^{5/2}} \right) \right) \quad (\text{A53})$$

A considerably simpler expression is obtained for the specific bending moment:

$$\tilde{m}^{11} = \frac{E}{b_s} \left(S_{\kappa_0} \frac{\sqrt{1 + 2\varepsilon_{11}} - 1}{1 + 2\varepsilon_{11}} + I_{\kappa_0} \left(\frac{\kappa_0 + \Delta\kappa_{11}}{(1 + 2\varepsilon_{11})^{3/2}} - \frac{\kappa_0}{1 + 2\varepsilon_{11}} \right) \right) \quad (\text{A54})$$

Recalling that the actual bending moment is $M = b_s \lambda_s^2 \tilde{m}^{11}$ and taking into account that deformation variables ε_{11} and $\Delta\kappa_{11}$ are linked to “our” variables ε_s and $\Delta\kappa$ by equations (A47)–(A48), we can easily check that equation (A54) exactly corresponds to the simple linear law (35) for the bending moment M in terms of ε_s and $\Delta\kappa$. For the effective membrane stress resultant \tilde{n}^{11} , the equivalence is more difficult to check because \tilde{n}^{11} corresponds to a combination of N and M , namely to $(\lambda_s N - \kappa M)/(b_s \lambda_s^3)$. The comparison becomes easier if the “original” (i.e., not effective) membrane stress resultant is expressed first:

$$n^{11} = \tilde{n}^{11} + \frac{\kappa}{\lambda_s} \tilde{m}^{11} = \tilde{n}^{11} + \frac{\kappa_0 + \Delta\kappa_{11}}{1 + 2\varepsilon_{11}} \tilde{m}^{11} = \frac{E}{b_s} \left(A_{\kappa_0} \frac{\sqrt{1 + 2\varepsilon_{11}} - 1}{1 + 2\varepsilon_{11}} + S_{\kappa_0} \left(\frac{\kappa_0 + \Delta\kappa_{11}}{(1 + 2\varepsilon_{11})^{3/2}} - \frac{\kappa_0}{1 + 2\varepsilon_{11}} \right) \right) \quad (\text{A55})$$

The resulting expression has the same structure as (A54), only with A_{κ_0} replaced by S_{κ_0} and S_{κ_0} replaced by I_{κ_0} , and so the equivalence to (34) is easy to verify.

We have shown that, for a given uniaxial hyperelastic stress-strain law, one can derive the corresponding stored energy density function ψ dependent on the sectional deformation variables such that the sectional equations (A41)–(A42) used by Simo and Fox¹⁹ become equivalent to our sectional equations (34)–(35). The opposite is not true, i.e., not all choices of ψ are consistent with a uniaxial material law. To see that, let us think of how the transformation performed in (A45) can be inverted, i.e., how the functional dependence of the strain energy density \mathcal{E}_{int} on the stretch can be identified if the dependence of ψ on the sectional deformation variables is prescribed. To be specific, let us consider that $\psi = \hat{\psi}(\lambda_s, \kappa)$, even though the proposed method would work for other choices of independent deformation variables as well. The key idea is that if λ_s and κ are selected such that $\kappa = \lambda_s \kappa_0$, then the fraction in (A45) that represents the stretch becomes independent of z , and the corresponding value of \mathcal{E}_{int}

can be taken out of the integral. The integral of $1 + z\kappa_0$ then gives the sectional area, $A = b_s h_s$, and the first equality in (A45) can be transformed into

$$\mathcal{E}_{int}(\lambda_s) = \rho_0 \hat{\psi}(\lambda_s, \lambda_s \kappa_0) \quad (\text{A56})$$

This means that function \mathcal{E}_{int} of one variable (the stretch) is uniquely determined by the values of function ψ on one single line in the plane of variables λ_s and κ . Once \mathcal{E}_{int} is extracted in this way, the values of $\hat{\psi}$ outside that special line are uniquely determined by (A45), and so they cannot be chosen arbitrarily. Of course, by far not all possible choices of $\hat{\psi}$ satisfy this constraint.

Let us now return attention to the approach used by Simo and Fox¹⁹. The reason why they introduced the effective membrane stress resultant \tilde{n}^{11} was that if ε_{11} and $\Delta\kappa_{11}$ are selected as the sectional deformation variables, then \tilde{n}^{11} is the static quantity that is work-conjugate with ε_{11} . For stored energy density ψ considered as a function of ε_{11} and $\Delta\kappa_{11}$, the sectional equations have the form (A41)–(A42). As the simplest formulation, Simo and Fox¹⁹ suggested to use linear and decoupled sectional equations, which would be in the present notation written as

$$\tilde{n}^{11} = \rho E h_s \varepsilon_{11} \quad (\text{A57})$$

$$\tilde{m}^{11} = \frac{\rho E h_s^3}{12} \Delta\kappa_{11} \quad (\text{A58})$$

This form of the equations would be obtained by transcribing the original equation (5.19) from Simo and Fox¹⁹, taking into account their equation (5.20) and setting the Poisson ratio to zero, to eliminate the difference between the beam and the cylindrical shell strip. However, equations (A57)–(A58) are not dimensionally correct, because ε_{11} is dimensionless, E is the Young modulus in Pa, h_s is the shell thickness (or beam depth) in m, \tilde{n}^{11} is a force per unit width, in N/m, and ρ is supposed to be the mass density per unit volume, in kg/m³. The derivation of these equations was not presented in detail, only briefly described as an approximation based on an asymptotic expansion, and the corresponding choice of stored energy potential ψ was not specified. One can only guess that the objective was to construct the equations in the simplest and decoupled form, which could be achieved by using the quadratic potential

$$\psi(\varepsilon_{11}, \Delta\kappa_{11}) = \frac{1}{2} C_1 \varepsilon_{11}^2 + \frac{1}{2} C_2 \Delta\kappa_{11}^2 \quad (\text{A59})$$

with the meaning of constants C_1 and C_2 yet to be identified. The corresponding sectional equations (A41)–(A42) would read

$$\tilde{n}^{11} = \bar{\rho} C_1 \varepsilon_{11} = h_s \rho_0 C_1 \frac{\varepsilon_{11}}{\sqrt{1 + 2\varepsilon_{11}}} \quad (\text{A60})$$

$$\tilde{m}^{11} = \bar{\rho} C_2 \Delta\kappa_{11} = h_s \rho_0 C_2 \frac{\Delta\kappa_{11}}{\sqrt{1 + 2\varepsilon_{11}}} \quad (\text{A61})$$

In this way, we would obtain an expression for \tilde{n}^{11} exclusively in terms of ε_{11} (and given constants), while \tilde{m}^{11} would depend not only on $\Delta\kappa_{11}$ but also slightly on ε_{11} , even though the potential ψ did not contain a mixed term with the product $\varepsilon_{11} \Delta\kappa_{11}$.

Equations (A60)–(A61) are nonlinear and (A61) contains both ε_{11} and $\Delta\kappa_{11}$. This could be fixed by considering static quantities $\hat{n} = \lambda_s \tilde{n}^{11}$ and $\hat{m} = \lambda_s \tilde{m}^{11}$ instead of \tilde{n}^{11} and \tilde{m}^{11} . The resulting sectional equations would be linear and decoupled. A more fundamental problem is related to the specific choice of quadratic potential (A59), which is not consistent with any hyperelastic uniaxial stress-strain law on the material level. To see that, let us first exploit formula (A56) and construct the strain energy density expression that *could be* (but actually is not) at the origin of the assumed quadratic potential (A59):

$$\mathcal{E}_{int}(\lambda_s) = \rho_0 \hat{\psi}(\lambda_s, \lambda_s \kappa_0) = \rho_0 \psi\left(\frac{1}{2}(\lambda_s^2 - 1), \kappa_0(\lambda_s^2 - 1)\right) = \left(\frac{\rho_0 C_1}{8} + \frac{\rho_0 C_2 \kappa_0^2}{2}\right) (\lambda_s^2 - 1)^2 \quad (\text{A62})$$

Recalling (A1), we realize that this is the strain energy density of the St. Venant-Kirchhoff material with elastic modulus

$$E = \rho_0 C_1 + 4\rho_0 C_2 \kappa_0^2 \quad (\text{A63})$$

So far we have shown that if the quadratic potential (A59) is derivable from a material-level strain energy expression, then the expression would need to have the form (A1), with E given by (A63). However, for this particular strain energy density, formula

(A45) gives

$$\begin{aligned}
 \hat{\psi}(\lambda_s, \kappa) &= \frac{1}{b_s h_s \rho_0} \int_A (1 + z\kappa_0) \mathcal{E}_{int} \left(\frac{\lambda_s + z\kappa}{1 + z\kappa_0} \right) dA = \frac{E}{8b_s h_s \rho_0} \int_A (1 + z\kappa_0) \left(\left(\frac{\lambda_s + z\kappa}{1 + z\kappa_0} \right)^2 - 1 \right) dA = \\
 &= \frac{E}{8b_s h_s \rho_0} \int_A \frac{\left((\lambda_s + z\kappa)^2 - (1 + z\kappa_0)^2 \right)^2}{(1 + z\kappa_0)^3} dA = \frac{E}{8b_s h_s \rho_0} \int_A \frac{(\lambda_s^2 - 1 + 2(\lambda_s \kappa - \kappa_0)z + (\kappa^2 - \kappa_0^2)z^2)^2}{(1 + z\kappa_0)^3} dA = \\
 &= \frac{E}{8b_s h_s \rho_0} \left(A_3 (\lambda_s^2 - 1)^2 + 4S_3 (\lambda_s^2 - 1) (\lambda_s \kappa - \kappa_0) + 2I_3 (2(\lambda_s \kappa - \kappa_0)^2 + (\lambda_s^2 - 1) (\kappa^2 - \kappa_0^2)) + \right. \\
 &\quad \left. + 4J_3 (\lambda_s \kappa - \kappa_0) (\kappa^2 - \kappa_0^2) + K_3 (\kappa^2 - \kappa_0^2)^2 \right) \quad (A64)
 \end{aligned}$$

Replacing λ_s by $\sqrt{1 + 2\varepsilon_{11}}$ and κ by $(\kappa_0 + \Delta\kappa_{11})/\sqrt{1 + 2\varepsilon_{11}}$, which are expressions that easily follow from (A49)–(A50), we obtain

$$\begin{aligned}
 \psi(\varepsilon_{11}, \Delta\kappa_{11}) &= \frac{E}{8\rho_0 b_s h_s} \left(A_3 4\varepsilon_{11}^2 + 8S_3 \varepsilon_{11} \Delta\kappa_{11} + 2I_3 \left(2\Delta\kappa_{11}^2 + 2\varepsilon_{11} \frac{\Delta\kappa_{11}^2 + 2\kappa_0 \Delta\kappa_{11} - 2\kappa_0^2 \varepsilon_{11}}{1 + 2\varepsilon_{11}} \right) + \right. \\
 &\quad \left. + 4J_3 \Delta\kappa_{11} \frac{\Delta\kappa_{11}^2 + 2\kappa_0 \Delta\kappa_{11} - 2\kappa_0^2 \varepsilon_{11}}{1 + 2\varepsilon_{11}} + K_3 \frac{(\Delta\kappa_{11}^2 + 2\kappa_0 \Delta\kappa_{11} - 2\kappa_0^2 \varepsilon_{11})^2}{(1 + 2\varepsilon_{11})^2} \right) \quad (A65)
 \end{aligned}$$

Here, A_3 to K_3 are modified sectional characteristics defined in (A5)–(A9). The resulting functional expression for ψ contains not only terms proportional to the squares of ε_{11} and $\Delta\kappa_{11}$ but also many terms with other powers, including mixed terms that depend on ε_{11} and $\Delta\kappa_{11}$ simultaneously. Therefore, the simple expression (A59) can be considered only as a convenient approximation, but it is not consistent with any hyperelastic law on the fiber level.

If the complete expression (A65) is substituted into (A39)–(A40), the resulting sectional equations are written in terms of internal forces \tilde{n}^{11} and \tilde{m}^{11} and deformation variables ε_{11} and $\Delta\kappa_{11}$, but they are equivalent with equations (A3)–(A4) written in terms of internal forces N and M and deformation variables ε_s and $\Delta\kappa$. For this consistent model, the effective membrane stress resultant \tilde{n}^{11} depends not only on ε_{11} but also on $\Delta\kappa_{11}$, in contrast to what was assumed in Simo and Fox¹⁹. Even if the consistently derived potential (A65) is approximated by a quadratic expression, the mixed terms still persist and no decoupling is achieved. The quadratic approximation obtained by neglecting terms of third and higher order in ε_{11} and $\Delta\kappa_{11}$ reads

$$\begin{aligned}
 \psi_Q(\varepsilon_{11}, \Delta\kappa_{11}) &= \frac{E}{8\rho_0 b_s h_s} (A_3 4\varepsilon_{11}^2 + 8S_3 \varepsilon_{11} \Delta\kappa_{11} + 2I_3 (2\Delta\kappa_{11}^2 + 2\varepsilon_{11} (2\kappa_0 \Delta\kappa_{11} - 2\kappa_0^2 \varepsilon_{11})) + \\
 &\quad + 4J_3 \Delta\kappa_{11} (2\kappa_0 \Delta\kappa_{11} - 2\kappa_0^2 \varepsilon_{11}) + K_3 (2\kappa_0 \Delta\kappa_{11} - 2\kappa_0^2 \varepsilon_{11})^2) = \\
 &= \frac{E}{2\rho_0 b_s h_s} ((A_3 - 2\kappa_0^2 I_3 + \kappa_0^4 K_3) \varepsilon_{11}^2 + 2(S_3 + \kappa_0 I_3 - \kappa_0^2 J_3 - \kappa_0^3 K_3) \varepsilon_{11} \Delta\kappa_{11} + (I_3 + 2\kappa_0 J_3 + \kappa_0^2 K_3) \Delta\kappa_{11}^2) = \\
 &= \frac{E}{2\rho_0 b_s h_s} ((A + 4\kappa_0^2 I_{\kappa_0}) \varepsilon_{11}^2 + 4S_{\kappa_0} \varepsilon_{11} \Delta\kappa_{11} + I_{\kappa_0} \Delta\kappa_{11}^2) \quad (A66)
 \end{aligned}$$

and the corresponding approximated sectional equations (A39)–(A40) are

$$\tilde{n}^{11} \approx \frac{h_s \rho_0}{\lambda_s} \frac{\partial \psi_Q}{\partial \varepsilon_{11}} \approx \frac{E}{b_s} ((A + 4\kappa_0^2 I_{\kappa_0}) \varepsilon_{11} + 2S_{\kappa_0} \Delta\kappa_{11}) \quad (A67)$$

$$\tilde{m}^{11} \approx \frac{h_s \rho_0}{\lambda_s} \frac{\partial \psi_Q}{\partial \Delta\kappa_{11}} \approx \frac{E}{b_s} (2S_{\kappa_0} \varepsilon_{11} + I_{\kappa_0} \Delta\kappa_{11}) \quad (A68)$$

Here we have replaced $1/\lambda_s = 1/(1 + \varepsilon_s)$ by 1, because ε_s is of the same order as ε_{11} , which is tacitly assumed to be small compared to 1 (note that $\partial \psi_Q / \partial \varepsilon_{11}$ is in fact a linear approximation of $\partial \psi / \partial \varepsilon_{11}$, which is applicable if the deformation variables are small). In the same spirit, we can use the linearized approximations

$$\varepsilon_{11} = \frac{1}{2} (\lambda_s^2 - 1) = \frac{1}{2} (2\varepsilon_s + \varepsilon_s^2) \approx \varepsilon_s \quad (A69)$$

$$\Delta\kappa_{11} = \lambda_s \kappa - \kappa_0 = (1 + \varepsilon_s)(\kappa_0 + \Delta\kappa) - \kappa_0 \approx \Delta\kappa + \kappa_0 \varepsilon_s \quad (A70)$$

and evaluate the transformation from the specific to the total internal forces:

$$M = b_s \lambda_s^2 \tilde{m}^{11} \approx b_s \tilde{m}^{11} \approx 2ES_{\kappa_0} \varepsilon_{11} + EI_{\kappa_0} \Delta\kappa_{11} \approx 2ES_{\kappa_0} \varepsilon_s + EI_{\kappa_0} (\Delta\kappa + \kappa_0 \varepsilon_s) = ES_{\kappa_0} \varepsilon_s + EI_{\kappa_0} \Delta\kappa \quad (A71)$$

$$\begin{aligned} N &= b_s \lambda_s^2 n^{11} = b_s \lambda_s^2 \left(\tilde{n}^{11} + \frac{\kappa}{\lambda_s} \tilde{m}^{11} \right) \approx b_s (\tilde{n}^{11} + \kappa_0 \tilde{m}^{11}) \approx (EA + 4\kappa_0^2 EI_{\kappa_0}) \varepsilon_{11} + 2ES_{\kappa_0} \Delta\kappa_{11} + 2\kappa_0 ES_{\kappa_0} \varepsilon_{11} + \kappa_0 EI_{\kappa_0} \Delta\kappa_{11} = \\ &= (EA + 2\kappa_0^2 EI_{\kappa_0}) \varepsilon_{11} + ES_{\kappa_0} \Delta\kappa_{11} \approx (EA + 2\kappa_0^2 EI_{\kappa_0}) \varepsilon_s + ES_{\kappa_0} (\Delta\kappa + \kappa_0 \varepsilon_s) = (EA + \kappa_0^2 EI_{\kappa_0}) \varepsilon_s + ES_{\kappa_0} \Delta\kappa \end{aligned} \quad (A72)$$

All the foregoing approximations have been based on the assumptions of small deformations ($\varepsilon_s \ll 1$, $\Delta\kappa \ll 1/h_s$) but nothing special has been assumed regarding the initial curvature, κ_0 (see Section A.5 for extended analysis). The resulting equations (A71)–(A72) are identical with equations (A14)–(A15) obtained by linearization of equations (34)–(35).

In summary, we have shown that the effective membrane stress resultant \tilde{n}^{11} in the form introduced by Simo and Fox does not really help to decouple the membrane and bending effects for an initially curved beam (considered here as a special case of a shell). The simple form of quadratic potential (A59) is not consistent with any model systematically derived from a hyperelastic uniaxial material law governing the response of each fiber, not even as an approximation valid in the small-strain range. If the quadratic approximation of the consistently derived potential is properly derived, the resulting formula (A66) contains a mixed term, which is then responsible for the coupling effect demonstrated in sectional equations (A39)–(A40). This effect is reflected by a mixed sectional stiffness $2ES_{\kappa_0}$, which is in fact the double of the mixed stiffness in sectional equations (A14)–(A15) or (34)–(35), written in terms of the standard (not effective) stress resultants.

A.4 Alternative definitions of effective force

The effective membrane stress resultant was defined by Simo and Fox such that it corresponds to the quantity work-conjugate with the membrane strain measure. However, this definition is also affected by the specific choice of the deformation variable characterizing flexural effects. For instance, if we select ε_s and $\Delta\kappa$ as the sectional deformation variables, the stress power per unit initial length of the beam segment is given by $N\dot{\varepsilon}_s + M\dot{\Delta\kappa}$, and so the force that provides work on increments of ε_s at constant $\Delta\kappa$ is simply the normal force, N . The shell model of Simo and Fox is based on deformation variables which, for a beam, reduce to ε_{11} and κ_{11} , defined in (A31) and (A30), and the stress power is then given by (A36). The force that provides work on increments of ε_{11} at constant κ_{11} is in fact not directly \tilde{n}^{11} defined in (A35) but the product $\tilde{n}^{11} \lambda_s$ (the additional multiplication by b_s is simple scaling by a constant, which only transforms the specific internal force, i.e., force per unit width, into the internal force at the level of the whole section of a given width). Clearly, other choices of sectional deformation variables are possible and they may lead to other work-conjugate internal forces.

One natural choice would be to select the flexural deformation measure such that it remains equal to zero if all fibers are stretched uniformly. A uniformly stretched straight beam would of course remain straight. For a curved beam segment whose centerline is initially a circular arc of radius R_0 that subtends an angle $d\varphi_0 = dx/R_0$, uniform stretching of all fibers leads to a centerline still located on a circle of radius R_0 but subtending an angle $d\varphi = \lambda_s d\varphi_0$. We have defined the curvature as $\kappa = \varphi' = d\varphi/dx$, which means that the initial curvature $\kappa_0 = d\varphi_0/dx$ is equal to $1/R_0$ but the curvature in a deformed state is in general not equal to the reciprocal value of the current radius of curvature. This is fine as long as the meaning of κ is properly interpreted. In the case of uniform stretching of all fibers, we get $\kappa = d\varphi/dx = \lambda_s d\varphi_0/dx = \lambda_s \kappa_0$. This is why we need to consider the combination of λ_s and $\kappa = \lambda_s \kappa_0$ when constructing the state of uniform strain energy density, which is exploited, e.g., in (A56). It is more natural to define the “true” curvature as $k = 1/R$ where R is the current radius of inertia. In general, $R d\varphi = \lambda_s dx$, and so $k = 1/R = \varphi'/\lambda_s = \kappa/\lambda_s$, from which $\kappa = k\lambda_s$ and $\dot{\kappa} = \dot{k}\lambda_s + k\dot{\lambda}_s$. The stress power per unit initial length is then

$$N\dot{\varepsilon}_s + M\dot{\kappa} = (N + kM)\dot{\varepsilon}_s + \lambda_s M\dot{k} \quad (A73)$$

The initial value of k is $k_0 = \kappa_0 = 1/R_0$. If we define potential

$$\psi(\lambda_s, \Delta k) = \frac{1}{b_s h_s \rho_0} \int_A (1 + z\kappa_0) \mathcal{E}_{int} \left(\frac{\lambda_s + z(\kappa_0 + \Delta k)\lambda_s}{1 + z\kappa_0} \right) dA = \frac{1}{b_s h_s \rho_0} \int_A (1 + z\kappa_0) \mathcal{E}_{int} \left(\lambda_s \left(1 + \frac{z\Delta k}{1 + z\kappa_0} \right) \right) dA \quad (A74)$$

as function of λ_s and $\Delta k = k - \kappa_0$, the sectional equations resulting from this choice of deformation measures read

$$N + kM = b_s h_s \rho_0 \frac{\partial \psi}{\partial \lambda_s} \quad (A75)$$

$$\lambda_s M = b_s h_s \rho_0 \frac{\partial \psi}{\partial \Delta k} \quad (A76)$$

The advantage of this formulation is that, for given $\psi(\epsilon_s, \Delta k)$, the strain energy density is easily identified as

$$\mathcal{E}_{int}(\lambda_s) = \rho_0 \psi(\lambda_s, 0) \quad (\text{A77})$$

For instance, for the material model with strain energy density given by (27), we obtain

$$\psi(\lambda_s, \Delta k) = \frac{E}{2\rho_0}(\lambda_s - 1)^2 + \frac{EI_{\kappa_0}}{2\rho_0 b_s h_s} \lambda_s^2 \Delta k^2 \quad (\text{A78})$$

and the corresponding sectional equations read

$$N + kM = EA(\lambda_s - 1) + EI_{\kappa_0} \lambda_s \Delta k^2 \quad (\text{A79})$$

$$\lambda_s M = EI_{\kappa_0} \lambda_s^2 \Delta k \quad (\text{A80})$$

The effective normal force, $N + kM$, depends not only on λ_s but also on Δk , and a full decoupling effect is not achieved. However, using the small-strain assumptions, we can construct the quadratic approximation

$$\psi_Q(\epsilon_s, \Delta k) = \frac{E}{2\rho_0} \epsilon_s^2 + \frac{EI_{\kappa_0}}{2\rho_0 b_s h_s} \Delta k^2 \quad (\text{A81})$$

and the corresponding linearized sectional equations

$$N + kM = EA\epsilon_s \quad (\text{A82})$$

$$M = EI_{\kappa_0} \Delta k \quad (\text{A83})$$

are indeed decoupled. The main point here is that the quadratic approximation (A81) does not contain the mixed term with the product $\epsilon_s \Delta k$. For other uniaxial hyperelastic models combined with the present choice of deformation variables, the exact potential is different from (A78) and introduces slight coupling, but the quadratic approximation of that potential always has the form (A81) and leads to decoupled linearized sectional equations. In this sense, $N + kM$ is a meaningful choice of the effective normal force, but it is not the only one.

To complete the picture, let us consider yet another choice of deformation variables, namely λ_s combined with

$$\tilde{\kappa} = \kappa - \kappa_0 \epsilon_s \quad (\text{A84})$$

or, equivalently, ϵ_s combined with

$$\Delta \tilde{\kappa} = \tilde{\kappa} - \kappa_0 = \kappa - \kappa_0 \lambda_s = \Delta \kappa - \kappa_0 \epsilon_s = \Delta k \lambda_s \quad (\text{A85})$$

The stress power per unit initial length can be expressed as

$$N \dot{\epsilon}_s + M \Delta \dot{\kappa} = N \dot{\epsilon}_s + M (\Delta \dot{\tilde{\kappa}} + \kappa_0 \dot{\epsilon}_s) = (N + \kappa_0 M) \dot{\epsilon}_s + M \Delta \dot{\tilde{\kappa}} \quad (\text{A86})$$

and so the forces work-conjugate with ϵ_s and $\Delta \tilde{\kappa}$ are $N + \kappa_0 M$ and M . This time, for the material model with strain energy density given by (27), the exact potential

$$\psi(\lambda_s, \Delta k) = \frac{E}{2\rho_0}(\lambda_s - 1)^2 + \frac{EI_{\kappa_0}}{2\rho_0 b_s h_s} \Delta \tilde{\kappa}^2 \quad (\text{A87})$$

is already quadratic in terms of $\epsilon_s = \lambda_s - 1$ and $\Delta \tilde{\kappa}$, and moreover does not contain the mixed term. The corresponding sectional equations

$$N + \kappa_0 M = EA\epsilon_s \quad (\text{A88})$$

$$M = EI_{\kappa_0} \Delta \tilde{\kappa} \quad (\text{A89})$$

are then linear and decoupled, provided that $N + \kappa_0 M$ is considered as the effective normal force. Linearity and decoupling for arbitrarily large deformation are special properties that are achieved only for one particular uniaxial hyperelastic material law. For other laws, the exact sectional equations would still be nonlinear and coupled, but their linearized form, applicable under the small-strain assumption, would be decoupled. Note that if the strains are considered as small, the difference between effective normal forces defined as $N + kM$ or as $N + \kappa_0 M$ is negligible.

formulation	deformation variables	stress power density	conjugate forces
1a – present	λ_s κ	$N\dot{\lambda}_s + M\dot{\kappa}$	N M
1b – present	ε_s $\Delta\kappa$	$N\dot{\varepsilon}_s + M\Delta\dot{\kappa}$	N M
2 – Simo and Fox	ε_{11} κ_{11}	$b_s\lambda_s(\tilde{n}^{11}\dot{\varepsilon}_{11} + \tilde{m}^{11}\dot{\kappa}_{11})$	$b_s\lambda_s\tilde{n}^{11} \equiv N/\lambda_s - \kappa M/\lambda_s^2$ $b_s\lambda_s\tilde{m}^{11} \equiv M/\lambda_s$
3a – alternative	λ_s k	$(N + kM)\dot{\lambda}_s + \lambda_s M\dot{k}$	$N + kM$ $\lambda_s M$
4b – alternative	ε_s $\Delta\tilde{\kappa}$	$(N + \kappa_0 M)\dot{\varepsilon}_s + M\Delta\dot{\tilde{\kappa}}$	$N + \kappa_0 M$ M

TABLE A1 Various formulations that differ by the choice of sectional deformation variables and the corresponding conjugate forces

A.5 Overview of formulations and discussion

The formulations discussed above are summarized in Table A1. Each of them is characterized by a specific choice of two variables that characterize the deformation of an infinitesimal segment. The stress power density (per unit length of the undeformed centerline) can be expressed in terms of rates of these variables and the corresponding conjugate variables (generalized internal forces) can be identified.

Formulations 1a and 1b are equivalent versions of the approach used in the present paper. The difference is only formal – 1a uses variables λ_s and κ , which do not vanish in the initial state, while formulation 1b uses $\varepsilon_1 = \lambda_s - 1$ and $\Delta\kappa = \kappa - \kappa_0$, which are true deformation variables that are initially equal to zero. The rates are the same for both formulations, and therefore the conjugate forces are also the same and they correspond to the standard normal force, N , and bending moment, M .

Formulation 2 is a reduced version of the approach used by Simo and Fox, adapted to the case of a planar curved beam. The original model for shells uses certain tensorial components which, for the beam, reduce to the Green-Lagrange strain at the centerline, $\varepsilon_{11} = (\lambda_s^2 - 1)/2$, and a curvature measure defined as $\kappa_{11} = \lambda_s \kappa$. The conjugate forces at the beam section level turn out to be $N/\lambda_s - \kappa M/\lambda_s^2$ and M/λ_s .

In Section A.4, we have also outlined two alternative formulations, which are presented in Table A1 under labels 3a and 4b. Formulation 3a combines the centerline stretch, λ_s , with the “true curvature”, k , which is equal to the reciprocal value of the current radius of curvature. These variables could be easily replaced by deformation variables ε_s and $\Delta k = k - \kappa_0$, which would lead to formulation 3b, with the same conjugate forces as for formulation 3a. Finally, formulation 4b is written directly in terms of deformation variables that vanish in the initial state, ε_s and $\Delta\tilde{\kappa}$, but it could also be presented as formulation 4a using λ_s and $\tilde{\kappa}$. The special definition of the “quasi-curvature” $\tilde{\kappa}$ given in (A84) leads to conjugate forces $N + \kappa_0 M$ and M , which have a certain potential advantage.

Each formulation provides a specific expression for the distribution of stretch across the section and, when combined with a suitable uniaxial hyperelastic stress-strain law, leads to a potential written in terms of the selected deformation variables. The sectional equations are then obtained by setting the conjugate forces equal to the partial derivatives of that potential with respect to the deformation variables. If the uniaxial law is given, all formulations obtained in this way are equivalent, just written in terms of different variables. Their mathematical form is in some particular cases simpler. For instance, for the law based on a linear relation between the Biot strain and its work-conjugate stress, formulation 1 gives linear sectional equations (for arbitrarily large deformations), and formulation 4 gives sectional equations that are not only linear, but also fully decoupled, still for arbitrarily large deformations. However, this would not be the case if formulation 4 is combined with another material law, e.g., the St. Venant-Kirchhoff law.

If the deformation is assumed to be small, the sectional equations can be linearized around the initial state. Since the distribution of Biot strain across the section is given by $\varepsilon = \lambda - 1 = (\varepsilon_s + z\Delta\kappa)/(1 + z\kappa_0)$ where z ranges from $-h_s/2$ to $h_s/2$, the small-strain assumption is in terms of the deformation variables written as $\varepsilon_s \ll 1$ and $\Delta\kappa \ll 1/h_s$. For other types of deformation variables this means that $\varepsilon_{11} \ll 1$, $\Delta\kappa_{11} \ll 1/h_s$, $\Delta k \ll 1/h_s$ and $\Delta\tilde{\kappa} \ll 1/h_s$. The resulting form of sectional equations becomes independent of the specific choice of the uniaxial law (provided that the elastic modulus is fixed), but it still depends on the choice of deformation variables. Consistent linearization leads to coupled linear equations for formulations 1 and 2, and

to two independent equations for formulations 3 and 4 (in fact, in the small-strain limit, formulations 3 and 4 become equivalent). For formulation 2, the consistently derived quadratic approximation of the potential ψ based on the assumptions of small deformation variables ($\epsilon_{11} \ll 1$ and $\Delta\kappa_{11} \ll 1/h_s$) with no other simplifying assumptions is given by (A66) and a mixed term with the product $\epsilon_{11}\Delta\kappa_{11}$ is present. The resulting linear sectional equations (A67)–(A68) contain a coupling sectional stiffness $2ES_{\kappa_0}$, which is in fact “twice as strong” as the coupling stiffness in equations (34)–(35) for our formulation 1. This means that transformation from formulation 1 to formulation 2 does not eliminate the coupling (makes it even stronger) and the interpretation of the effective membrane stress resultant \tilde{n}^{11} as a quantity related exclusively to the membrane strain and independent of the curvature is in general not justified.

All previous considerations have been done without any restrictions on the initial curvature, except for the mild assumption that $1 \pm h_s\kappa_0/2$ remains positive and not “too small” (in geometric terms, the initial center of curvature of the centerline is outside the beam). It is instructive to rewrite the quadratic potential (A66) as

$$\psi_Q(\epsilon_{11}, \Delta\kappa_{11}) = \frac{EA}{2\rho_0 b_s h_s} \left(\left(1 + 4\kappa_0^2 i_{\kappa_0}^2\right) \epsilon_{11}^2 - 4 \frac{\kappa_0 i_{\kappa_0}^2}{h_s} \epsilon_{11} (h_s \Delta\kappa_{11}) + \frac{i_{\kappa_0}^2}{h_s^2} (h_s \Delta\kappa_{11})^2 \right) \quad (\text{A90})$$

where $i_{\kappa_0} = \sqrt{I_{\kappa_0}/A}$ is the modified radius of inertia of the section, which is comparable to the sectional depth, h_s . We have exploited here the general relation $S_{\kappa_0} = -\kappa_0 I_{\kappa_0}$ and transformed the curvature change, $\Delta\kappa_{11}$, to a small dimensionless variable $h_s \Delta\kappa_{11}$. One could now make an additional assumption that the initial radius of curvature is much larger than the beam depth, i.e., $\kappa_0 \ll 1/h_s$. This leads to $\kappa_0 i_{\kappa_0} \ll 1$ and the factor that multiplies the mixed term in (A90) becomes much smaller than the factors that multiply the other two terms. The quadratic potential can then be legitimately approximated by

$$\psi_Q(\epsilon_{11}, \Delta\kappa_{11}) = \frac{EA}{2\rho_0 b_s h_s} \left(\epsilon_{11}^2 + \frac{i_{\kappa_0}^2}{h_s^2} (h_s \Delta\kappa_{11})^2 \right) \quad (\text{A91})$$

So, if the initial curvature is small, one can indeed postulate the potential in the form (A59) and obtain decoupled sectional equations. However, under the same assumptions, one could use analogous arguments to simplify the quadratic potential (A46) that is written in terms of ϵ_s and $\Delta\kappa$ and corresponds to formulation 1, and the resulting equations would be directly the traditional simplified sectional equations (41)–(42). This means that, if the initial curvature is small, there is no need to transform the standard normal force into an effective one. And if the initial curvature is not small, the proper definition of the effective normal force should be based on formulation 3 or 4.

B LOGARITHMIC SPIRAL: DESCRIPTION OF THE INITIAL SHAPE

The logarithmic spiral is easily defined in polar coordinates by equation (156) but the algorithm developed in Section 3 works with local Cartesian coordinates aligned with the curved element. The initial deviation from a straight shape needs to be described by functions that depend on the coordinate measured as the arc length along the undeformed centerline. The purpose of this appendix is to show the derivation of these functions.

In the first step, we can easily express Cartesian coordinates with respect to an auxiliary coordinate system with the origin placed at the pole of the polar coordinates and with axis \hat{z} considered as the axis from which the polar angle is measured counterclockwise; see Fig. B1. Since the radial coordinate is a given exponential function of the polar angle, the Cartesian coordinates can be expressed as unique functions of the polar angle:

$$\hat{x} = r \sin \theta = a e^{b\theta} \sin \theta \quad (\text{B92})$$

$$\hat{z} = r \cos \theta = a e^{b\theta} \cos \theta \quad (\text{B93})$$

The final objective is to use the arc-length coordinate s as the independent variable, and so we need to find the link between θ and s . The differential of the arc length is expressed as

$$\begin{aligned} ds &= \sqrt{(d\hat{x})^2 + (d\hat{z})^2} = \\ &= \sqrt{(a b e^{b\theta} \sin \theta + a e^{b\theta} \cos \theta)^2 + (a b e^{b\theta} \cos \theta - a e^{b\theta} \sin \theta)^2} d\theta = \\ &= a \sqrt{1 + b^2} e^{b\theta} d\theta \end{aligned} \quad (\text{B94})$$

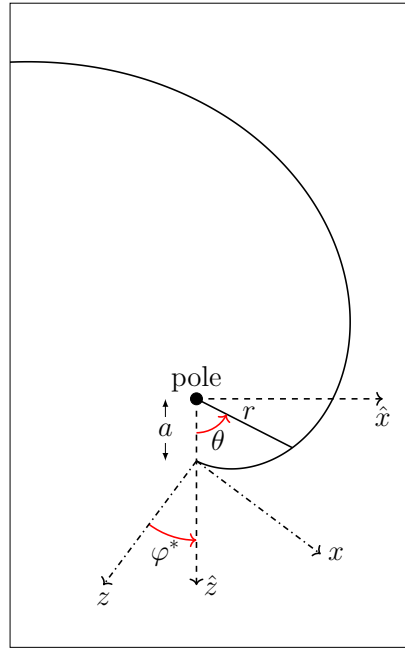


FIGURE B1 Geometry of the logarithmic spiral and position of the auxiliary Cartesian axes \hat{x} and \hat{z} and of the local Cartesian axes x and z aligned with the left end of the element (illustrative plot with $b = 0.5$, leading to a faster increase of the radial coordinate than for $b = 0.15$ considered in the example).

and integration with initial condition $s = 0$ at $\theta = 0$ leads to

$$s = \frac{a\sqrt{1+b^2}}{b} (e^{b\theta} - 1) = \frac{1}{c} (e^{b\theta} - 1) \quad (\text{B95})$$

where $c = b/(a\sqrt{1+b^2})$ is an auxiliary parameter introduced for convenience; see also (160). By inversion of (B95) one easily gets

$$\theta(s) = \frac{\ln(1+cs)}{b} \quad (\text{B96})$$

and substitution back into (B92)–(B93) yields

$$\hat{x}(s) = a(1+cs) \sin \theta(s) \quad (\text{B97})$$

$$\hat{z}(s) = a(1+cs) \cos \theta(s) \quad (\text{B98})$$

It is also useful to express the angle $\hat{\varphi}$ by which the tangent to the spiral deviates (counterclockwise) from the \hat{x} axis, because this at the same time determines the deviation of the cross section from the \hat{z} axis. From

$$\begin{aligned} \cos \hat{\varphi}(s) &= \frac{d\hat{x}(s)}{ds} = ac \sin \theta(s) + a(1+cs) \cos \theta(s) \frac{c}{b(1+cs)} = \\ &= \frac{b}{\sqrt{1+b^2}} \sin \theta(s) + \frac{1}{\sqrt{1+b^2}} \cos \theta(s) \end{aligned} \quad (\text{B99})$$

one can infer that

$$\hat{\varphi}(s) = \theta(s) - \varphi^* \quad (\text{B100})$$

where $\varphi^* = \arctan b$, as defined in (161). Interestingly, each section deviates from the radial direction by the same angle, φ^* .

The final step consists in transformation of the derived expressions from the auxiliary Cartesian coordinate system aligned with the pole and starting point of the spiral to the local Cartesian coordinate system used by the algorithm, which as its origin at the starting point of the spiral, i.e., at $\hat{x} = 0$ and $\hat{z} = a$, and the x axis is tangent to the spiral at that point. This implies that x and z are rotated clockwise by φ^* with respect to \hat{x} and \hat{z} , and the transformation equations can be written as

$$x = \hat{x} \cos \varphi^* + (\hat{z} - a) \sin \varphi^* \quad (\text{B101})$$

$$z = -\hat{x} \sin \varphi^* + (\hat{z} - a) \cos \varphi^* \quad (\text{B102})$$

Substitution from (B97)–(B98) then gives

$$x(s) = a((1 + cs) \sin(\theta(s) + \varphi^*) - \sin \varphi^*) \quad (\text{B103})$$

$$z(s) = a((1 + cs) \cos(\theta(s) + \varphi^*) - \cos \varphi^*) \quad (\text{B104})$$

Having derived the description of the initial spiral shape, we can proceed to the interpretation of the results in the notation used in the main body of this paper. In the present derivation, s denotes the arc-length coordinate and $x(s)$ and $z(s)$ specify the local Cartesian coordinates of the point on the centerline at arc-length distance s from the left end. However, the theoretical considerations in Section 2 as well as the numerical techniques described in Section 3 use x instead of s and interpret this symbol as the x coordinate of the point in the fictitious straight configuration, which would arise if the centerline were unfolded without changing its length (see Section 2.1). The position of each centerline point in the initial curved configuration is then described by the differences u_{s0} and w_{s0} with respect to the straight configuration. This means that on the left-hand sides of (B103)–(B104) we need to replace $x(s)$ by $x + u_{s0}(x)$ and $z(s)$ by $w_{s0}(x)$, and on the right-hand sides s by x . Furthermore, the initial deviation of a generic section from the direction aligned with the left-end section, denoted in Sections 2–3 as φ_0 , is given by $\hat{\varphi} + \varphi^*$ (because the present xz coordinate system is rotated with respect to the $\hat{x}\hat{z}$ coordinate system by φ^* clockwise), and therefore, in view of (B100), φ_0 turns out to be equal to the polar angle θ , which is expressed by (B96). This leads to equation (157), and we can also replace the symbol $\theta(s)$ on the right-hand sides of (B103)–(B104) by $\varphi_0(x)$, which finally yields equations (158)–(159).